Study of Kesterite Cu2ZnSnS4 Thin Films prepared from Cu2ZnSnS4 Nanoparticle Inks

LATIFAH MUHAREB ALSHAMMARI

Study of Kesterite Cu_2ZnSnS_4 Thin Films prepared from Cu_2ZnSnS_4 Nanoparticle Inks

Latifah M. Alshammari

A thesis presented for the degree of
Doctor of Philosophy

Department of Physics
The University of Durham
Supervised by
Professor Douglas Halliday
Professor Marek Szablewski
United Kingdom
February 2023

Study of Kesterite Cu_2ZnSnS_4 Thin Films prepared from Cu_2ZnSnS_4 Nanoparticle Inks

Abstract

Due to the recent rapid industrial and population growth, there has been an increase in the demand for energy which has led to a strong reliance on non-renewable energy sources which has negative environmental effects. Due to its unlimited sources and absence of environmentally harmful green house gas emissions, solar energy has emerged as an effective candidate for renewable energy. Cu_2ZnSnS_4 (CZTS) has been widely investigated as an absorber for thin film solar cells. It can replace $Cu(In, Ga)Se_2$ (CIGS), and CdTe since it consists of non-toxic, abundant, and cheap elements. Its high absorption coefficient, optimal band gap, and naturally abundant non-toxic elemental constituents give it several advantages over most thin film absorber materials. However, the present performance of CZTS solar cells is still below their theoretical limit. Recently, there has been a rise in interest in improving the performance and lowering the production cost of solar cells based on CZTS.

In this study, CZTS nanocrystals were synthesized by one of the non-vacuum techniques: the CZTS absorber is synthesized by using the hot injection technique, and it is responsible for synthesizing the crystalline layer that performs as the solar cell device absorber. CZTS nanoparticles were synthesized using a chemical synthesis process, with sulphur being injected into a solution of hot metallic precursor ions. It was revealed that the reaction temperature and time greatly influenced their composition, structure, and optical properties. In this research, a method was proposed to fabricate nonstoichiometric CZTS thin films. Using soda lime glass and molybdenum substrates, the CZTS thin films were deposited on the different substrates by drop casting and spin coating methods, followed by preheating in air and post-deposition annealing treatments, in two different atmospheres, H_2S and N_2. The CZTS thin films were annealed at different annealing temperatures. The morphology, composition,

structure, and optical properties of the CZTS thin films were characterized using scanning electron microscopy, energy dispersive X-ray spectroscopy, X-ray diffraction, Raman spectroscopy, and UV-vis spectroscopy. The influence of the annealing on the morphology, composition, and structure of the films has been studied. From the XRD patterns of the CZTS thin films, the peaks of all CZTS thin films are indexed to tetragonal CZTS (PDF 026-0575) and can be attributed to the (112), (220), and (312) planes of kesterite CZTS, respectively. The Raman spectra of the samples give evidence that in all spectra the dominant peaks are located at 330–338 cm^{-1}, indicating that these samples contain peaks associated with the Cu_2ZnSnS_4 phase. A significant influence on the energy bandgap of CZTS thin films was observed during the annealing of thin films. In addition, the fabrication of CZTS/CdS heterojunctions was explored to gain a better understanding of the properties of the interface reactions that take place between the Mo/CZTS and CZTS/CdS layers. the effect of high annealing temperature on a Mo/CZTS/CdS heterojunction was carried out at temperatures ranging from 450°C to 550°C at an annealing time of one hour in H_2S and N_2 atmosphere . Annealing promotes cadmium diffusion from the n-type semiconductor to the absorber. According to various studies, Cd diffusion improved the performance of thin-film solar cells. However, at annealing temperatures of 500 and 550 °C, the presence of a Cu-related secondary phase was observed, which is detrimental because it introduces shunting routes that lower the devices' FF due to its metallic nature and low resistivity profile. In addition, Mo combines with S at the CZTS/Mo interface to form MoS_2, which leads to losses of Voc, Jsc, and FF in CZTS devices. The findings presented here indicate that there is significant interdiffusion of the elements from the different layers in a Mo/CZTS/CdS heterojunction, which occurs at the temperatures commonly used to fabricate CZTS devices. Further improvements in CZTS devices will require strategies to control this interdiffusion.

Supervisors: Professor Douglas Halliday and Professor Marek Szablewski.

Acknowledgements

I'd like to thank my supervisor, Prof. Douglas Halliday, for his continuous encouragement and direction throughout the study. He provided me with valuable feedback on the research. He has always been so kind and encouraging of all of my efforts and struggles. It has been a great experience working under his supervision, and I feel like I've learned and developed a lot. Thanks from the bottom of my heart to Prof. Marek Szablewski for his help with this project, for his hard work guiding me to the completion of this project, and especially for his assistance in the chemistry laboratory. I would like to use this opportunity to offer my most sincere gratitude to each of them. Douglas and Marek are particularly deserving of my gratitude for the continuous guidance, direction, and support they have given me during my research. I would want to express my gratitude to them for providing me with the opportunity to carry out the research under their supervision. It would have been difficult to complete this project on time without their encouraging supervision and constructive advice. I consider myself the most lucky PhD student because I had the opportunity to work closely with them.

I'd like to give special thanks to the following individuals who assisted me in the physics department: Thanks to Dr. Fernando Dias and his group for assistance in his laboratory and Dr. Aidan Hindmarch for assistance in sputtering laboratory and being around for queries. Thanks to Mr. Leon Bowen for organizing the SEM training, and to Dr. Diana Talia Alvarez Ruiz for performing FIB microscope cross-sectional imaging on samples. I'd like to thank the technical and support staff in the physics department at the University of Durham for all their assistance. Thanks to Mr. David Pattinson for assistance in annealing using the furnace; Mr. Duncan McCallum, Mr. Michael Armstrong and Mr. Wayne Dobby for their assistance, and all the other technicians in the department who offered help if needed.

I would like to extend my gratitude to members of the chemistry department for

providing facilities to carry out my research. I also would like to thank Prof. Andy Beeby for providing Raman spectroscopy equipment and for teaching me how to use his Raman microscope and the instructions thereon. I also want to thank Mr. Gary Oswald for his X-ray diffraction training. Thanks to Ph.D. student David A. Palacios-Gomez in the Engineering Department who tried to help in using the solar simulator but, unfortunately, it was not completed as a result of lockdown because of the COVID-19 coronavirus pandemic.

Also, I'd like to thank the following people for their help in completing the project: PhD candidates Yasir Altowairqi and his assistance in the first year in the synthesis of CZTS nanocrystals; Oliver Rigby and his assistance in annealing using a furnace; and thanks to Taghreed Alsulami whos ready to help any time. Also to fellow master's student Gerardo Pérez Marin. Also special thanks to Karen Stroh, for her assistance in the synthesis and deposition of CZTS nanocrystals. Finally, I would like to thank my family and especially my daughter Alreem for their love and supports.

Contents

Declaration **xi**

List of Figures **xii**

List of Tables **xviii**

1 Introduction **1**

1.1 Research motivations 1

1.2 Aims of the study 7

1.3 Thesis outline 7

2 Thin-film solar cells **9**

2.1 Development of solar cells 9

2.1.1 The first generation solar cell 9

2.1.2 The second generation solar cell 10

2.1.3 The third generation solar cell 10

2.2 The photovoltaic effect 10

2.3 Characteristics of photovoltaic materials 12

2.3.1 Absorption coefficient 12

2.3.2 Band gap 12

2.4 Theory of $p - n$ junction 15

2.5 Device characterisation 18
2.5.1 Current-voltage measurement 18
2.5.2 External quantum efficiency 20
2.6 Losses in a solar cell 21
2.6.1 Optical losses 21
2.6.2 Recombination losses 21
2.6.3 Metal/semiconductor interface 22
2.6.4 Resistance losses 22

3 Copper zinc tin sulphide (Cu_2ZnSnS_4)-based thin-film solar cells 23
3.1 Introduction 23
3.2 Crystal structure of CZTS 24
3.2.1 Structure of kesterite and stannite Cu_2ZnSnS_4 24
3.3 Optical and electronic properties 26
3.3.1 The band structure 26
3.4 Thin-film growth methods 28
3.4.1 Vacuum-based deposition techniques 29
3.4.1.1 Vacuum evaporation 29
3.4.1.2 Magnetron sputtering 30
3.4.1.3 Electron beam evaporation 30
3.4.1.4 Spray pyrolysis 30
3.4.1.5 Pulsed laser deposition 31
3.4.2 Non-vacuum-based deposition techniques 31
3.4.2.1 Sol–gel deposition 31
3.4.2.2 Successive ionic layer adsorption and reaction 32
3.4.2.3 Solvothermal 32
3.4.2.4 Electro-deposition method 33
3.4.2.5 Nanoparticle inks 33
3.5 Construction of the CZTS solar cell 34
3.5.1 Thickness of the layers in the solar cell 34

3.5.2 Rear contact . . . 35
3.5.3 Absorber layer . . . 35
3.5.4 Buffer layer . . . 36
3.5.4.1 CdS buffer layer . . . 36
3.5.4.2 Alternative buffer layer . . . 37
3.5.5 Window and TCO layers . . . 38
3.6 Annealing / sulphurisation . . . 38
3.7 Grain growth . . . 39
3.8 Challenge toward highly efficient CZTS solar cells . . . 40
3.8.1 Secondary phases . . . 41
3.8.2 Sodium impurities . . . 42
3.8.3 Defects in CZTS . . . 43
3.8.3.1 Vacancy . . . 44
3.8.3.2 Interstitial . . . 44
3.8.3.3 Antistite defects . . . 44
3.9 Fluctuations in band gap . . . 46
3.9.1 Interface losses . . . 46
3.9.1.1 Mo/CZTS interface . . . 46
3.9.1.2 CZTS/CdS interface . . . 49
3.10 Summary . . . 51

4 Cu_2ZnSnS_4 thin film fabrication and characterisation techniques 53

4.1 Thin films fabrication . . . 53
4.1.1 CZTS nanocrystal-based approaches . . . 53
4.1.2 Synthesis of Cu_2ZnSnS_4 CZTS nanoparticles . . . 54
4.1.3 CZTS ink fabrication . . . 55
4.1.4 Fabrication of Cu_2ZnSnS_4 thin films . . . 56
4.1.4.1 Substrate preparation . . . 56
4.1.4.2 Deposition of rear contact (Mo) . . . 57
4.1.4.3 Deposition of Cu_2ZnSnS_4 thin films . . . 57

4.1.4.4 Deposition of CdS buffer layer 59
4.1.5 Annealing of the CZTS thin film 60
4.2 Characterisation techniques 62
4.2.1 Scanning electron microscopy 63
4.2.1.1 Sample coating 63
4.2.1.2 SEM imaging 64
4.2.1.3 Atomic composition 66
4.2.2 Focused ion beam milling 67
4.2.3 X-ray diffraction 68
4.2.3.1 Estimation of lattice parameters and grain size . . . 68
4.2.3.2 Identification of secondary phases 70
4.2.4 Raman spectroscopy 71
4.2.5 Optical spectroscopy measurements 73
4.3 Summary 74

5 Spin coated kesterite Cu_2ZnSnS_4: optical, structural, and morphological investigations for photovoltaic applications 75

5.1 Introduction 75
5.2 characterisation of the absorber layer 76
5.2.1 CZTS thin film as deposited characterisation 76
5.2.1.1 Composition analysis 76
5.2.1.2 Morphological characterisation 76
5.2.1.3 Structural characterisation 77
5.2.1.4 Optical characterisation 78
5.3 The influence of reaction time 79
5.3.1 Chemical composition 80
5.3.2 Crystal structure 80
5.3.2.1 X-ray diffraction 80
5.3.3 Optical characterisation 81
5.4 Influence of reaction temperature 82

5.4.1 Chemical composition 83
5.4.2 Film morphology 83
5.4.3 Crystal structure 85
5.4.3.1 X-ray diffraction 85
5.4.3.2 Raman spectroscopy 86
5.4.4 Optical characterisation 87
5.5 Summary 89

6 Effects of heat treatments on Cu_2ZnSnS_4 thin films deposited by the spin coating technique 90

6.1 Introduction 90
6.2 The influence of preheat treatment on Cu_2ZnSnS_4 thin films 92
6.2.1 Influence of preheat treatment time on CZTS thin films . . . 92
6.2.1.1 Structure characterisation 92
6.2.1.2 Optical characterisation 94
6.2.2 Influence of preheating temperatures on CZTS thin films . . 95
6.2.2.1 Structure analysis 95
6.2.2.2 Morphology analysis 97
6.2.2.3 Optical analysis 98
6.3 Effect of annealing on Cu_2ZnSnS_4 thin films 100
6.3.1 Heterojunction fabrication 101
6.3.1.1 Structure analysis 102
6.3.1.2 Optical properties 105
6.3.1.3 Electron microscopy morphology analysis 105
6.3.1.4 Cross section element mapping 107
6.4 Summary 115

7 Structural, morphological and optical properties of Cu_2ZnSnS_4 thin films deposited by the drop-casting technique 116

7.1 Effect of annealing temperature 118

7.1.1 Composition analysis . . . 118
7.1.2 Morphology characterisation . . . 119
7.1.3 Crystal structure . . . 119
7.1.3.1 X-ray diffraction . . . 119
7.1.3.2 Raman spectroscopy . . . 121
7.1.4 Optical characterisation . . . 123
7.2 Influence of annealing time . . . 124
7.2.1 Composition analysis . . . 124
7.2.2 Morphology characterisation . . . 124
7.2.3 Crystal Structure . . . 126
7.2.3.1 X-ray diffraction . . . 126
7.2.3.2 Raman spectroscopy . . . 127
7.2.4 Optical characterisation . . . 128
7.3 Summary . . . 129

8 Conclusions **131**
8.1 Thesis summary . . . 131
8.2 Suggestions for further work . . . 133

Bibliography **135**

Declaration

I declare that the work presented in this thesis has not been submitted for any other degree and that the candidate is responsible for all the work included in this thesis that they have presented, excluding the work detailed below.

- Some of the XRD measurements during the Corona virus pandemic have been carried out by Gary Oswald (Department of Chemistry, Durham University).
- The cross-sectional images presented in Section 6.3 have been done by Mr. Leon Bowen (Department of Physics, Durham University) and Dr. Diana Talia Alvarez Ruiz (School of Chemical Engineering and Analytical Science, University of Manchester).

The work in this thesis is based on research carried out at the Centre for Materials Physics, Department of Physics, University of Durham, England. No part of this thesis has been submitted elsewhere for any other degree or qualification, and it is the sole work of the author unless referenced to the contrary in the text.

List of Figures

1.1 (AM0) spectra at the top of the earth's atmosphere and (AM1.5) at sea level. 2
1.2 Efficiencies of different semiconductors shown against the Shockley–Queisser limit 4

2.1 E vs. k curve of a direct (a) and indirect (b) band gap semiconductor [40]. 13
2.2 Absorption spectra of various semiconductors. 14
2.3 A p-type semiconductor comes in contact with an n-type semiconductor to form a $p-n$ junction. 16
2.4 Band diagram of a $p-n$ junction before and after contact. 16
2.5 Forward and reverse bias energy band diagrams of a $p-n$ junction. . . 18
2.6 Current-Voltage characteristic of a solar cell in the dark and under illumination and showing solar cell parameter. 19
2.7 Equivalent circuit for a real solar cell. 20
2.8 The loss mechanism in a typical $p-n$ junction solar cell. 22

3.1 NREL *Best Research-Cell Efficiency Chart* showing photovoltaic efficiency records for several solar cell technologies from the NREL PV website [63]. 25

3.2 3D perspective view of (a) kesterite-type and (b) stannite-type CZTS structures. 26
3.3 Energy-band structure of kesterite-type CZTS. 28
3.4 Schematic diagram of CZTS thin film based solar cell device. 34
3.5 The defect ionisation levels in the band gaps of Cu_2ZnSnS_4 (A). The red bars show the levels of acceptors, whereas the blue bars represent the levels of donors. 46
3.6 simplified diagram showing the two possible conduction band offset at the pn-junction, (a) cliff type, (b) spike type barriers. 51

4.1 Schematic diagram of the setup for the synthesis, fabrication, and annealing of CZTS thin films. 56
4.2 Schematic diagram of chemical bath deposition (CBD). 59
4.3 The furnace and gas supply sulphurisation annealing system to perform the annealing measurements required for this thesis a) front view; b) side view; and nitrogen valve (1), flush valve (2), the gas mix valve (3), vacuum valve (4), and the furnace valve (5). 62
4.4 A schematic annealing temperature cycle of CZTS thin films in the furnace, not to scale. 63
4.5 Schematic diagram of scanning electron microscope (SEM). 64
4.6 Signals emitted by incident electron beam-sample interactions. 66
4.7 Schematic diagram of the characteristic X-ray generation. 67
4.8 Schematic diagrams of the FEI Helios Nano Lab 600 Dual Beam system available in the laboratory where some of the work for this thesis was performed. 68
4.9 The interaction of two x-rays with repeating atomic lattice planes. . . . 69
4.10 Energy-level diagram involved in the Raman Effect. Displays anti-Stokes and Rayleigh scattering by a molecule excited by a photon with energy $E = h\upsilon$. 72

5.1 Top view(a) and cross section (b) SEM images of the as-deposited CZTS film on SLG coated by Mo substrate at reaction temperature 225 °C at 30 min at a magnification of 5k and 20k respectively 77
5.2 XRD patterns (a) and Raman spectra (b) of CZTS thin films deposited on glass substrate using ink synthesised for 0.5 hour at 225 °C. 78
5.3 Absorption versus wavelength of CZTS film grown for 0.5 hour at 225 °C. The inset shows the Tauc Plot of $(\alpha h\nu)^2$ vs. $h\nu$. 79
5.4 The XRD spectra of CZTS thin films deposited on glass and synthesised at different reaction times at 225 °C. The reference values PDF026-0575 are shown in the red stick plot. 81
5.5 Absorbance versus photon energy for CZTS thin films synthesised at reaction time (30, 60 min). The inset shows a plot of $(\alpha h\nu)^2$ vs. $(h\nu)$ used to determine the optical band gap. 82
5.6 SEM plan view images of the thin film synthesised at different reaction temperatures 175-250 °C at reaction times of 0.5 h. 84
5.7 The XRD patterns of CZTS thin films synthesised at different reaction temperatures in the range (175-250 °C). The reference PDF026-0575 is shown in the red stick plot. 86
5.8 Raman spectra of CZTS thin films synthesised at different reaction temperatures. 87
5.9 Tauc Plot of $(\alpha h\nu)^2$ versus photon energy $(h\nu)$ for CZTS for samples at different reaction temperatures, used to determin the energy band gap. 88

6.1 XRD patterns of as deposited and preheated films at 310 °C on a hotplate at different times.A reference pattern from the ICDD database for kesterite Cu_2ZnSnS_4 (PDF 00-026-0575) is shown as a stick plot. . . . 93
6.2 Absorption spectra of CZTS thin films heated on a hotplate at a temperature of 310 °C at different times. 94

6.3 Tauc plot of $(\alpha\ h\nu)^2$ versus photon energy $(h\nu)$ for CZTS thin films heated at various times at a constant temperature of 310 °C. The intercept of the straight line fit gives the values of the energy bandgap. 95
6.4 Raman spectra of CZTS thin films heated at 150–230 °C for 3 min. . . . 96
6.5 Top view and cross-sectional SEM image view of preheated CZTS films,at a magnification of × 40k in the left-hand column and of × 100k in the right-hand column respectively. (a, b) 170 °C, (c, d) 190 °C, and (e, f) 230 °C 97
6.6 UV-Vis absorption spectra of the as-synthesized CZTS thin film and preheated thin films at different hot-plate temperatures 150-230 °C for 3 min. 98
6.7 Plot of $(\alpha\ h\nu)^2$ vs photon energy at different preheating temperatures. The estimated energy gaps are shown in the inset. 99
6.8 UV-vis absorption spectra of the as-synthesized CZTS thin film at reaction time of 60 min and preheated films at different hot plate temperatures. 99
6.9 Plot of $(\alpha\ h\nu)^2$ vs photon energy at different preheating temperatures treated for 60 minuutes. The estimated energy gaps are shown in the inset. 100
6.10 XRD patterns of the CZTS thin films annealed at different temperatures.102
6.11 Raman spectra of annealed CZTS thin films at different annealing temperatures. 103
6.12 Raman spectra of CZTS as-deposited and annealed at different temperatures in a sulphur atmosphere; the spectra were fitted using Gaussian–Lorentzian shape components. 104
6.13 A Tauc plot based on the UV-Vis absorption spectra of the as-synthesized and annealed CZTS thin films at different temperatures, showing $(\alpha\ h\nu)^2$ vs. photon energy $(h\nu)$ to determine the energy band gap. 105

6.14 Top view images of as-deposited CZTS thin film deposited on glass substrate synthesised for 30 minutes at 225°C reaction temperature (a, b) and top view and cross section images of annealed film at 450°C for 1 hour under H_2S and N_2 pressure (20:80) (c-f), (e) and (f) at a magnification of 20k and 80k respectively. 106

6.15 Elemental mapping of elements in CZTS/glass thin film cross section after annealing at 500 °C in a H_2S+N_2 (20:80) atmosphere (at a magnification of × 6.5k). Each element concentration profile is indicated as a different colour and overlayed on the original microscopy image. The greater intensity of colour indicates a higher element concentration. . . 108

6.16 Elemental mapping of elements in the cross section of Mo/CZTS/CdS heterojunction films at annealing temperatures of 500 °C in a H_2S+N_2 (20:80) atmosphere, at a magnification of 8k. Each element concentration profile is indicated as a different colour and overlayed on the original microscopy image. The greater intensity of colour indicates a higher element concentration. 109

6.17 Elemental mapping of elements in a cross section of Mo/CZTS/CdS film at annealing temperature of 550 °C in H_2S and N_2 at a magnification of × 1.23k (Site 1). 111

6.18 SEM surface image and EDX spectrum of deposited CZTS thin film annealed at 500 °C for one hour in H_2S and N_2 (20:80). 112

6.19 Elemental mapping of elements in a cross section of Mo/CZTS/CdS films at annealing temperature of 550 °C for one hour in a H_2S and N_2 at a magnification of × 3.19k (Site 2). 114

7.1 SEM top views (a, b) and cross-sectional images (c, d) of CZTS thin films deposited by drop-casting before annealing at different magnifications (10k, 40k, 100k, and 200k, respectively). 117

7.2 SEM images of a CZTS drop cast thin film deposited on a glass substrate and annealed for 1 hour under $H_2S + N_2$ 20:80 pressure at temperatures of (a) 375, (b) 400, (c) 500, and (d) 550 °C 120
7.3 XRD patterns of annealed CZTS thin films at various temperatures for 1 hour. A reference pattern from the ICDD database for kesterite Cu_2ZnSnS_4 (PDF 00-026-0575) is shown in the red stickplot. 121
7.4 The fitting with Lorentzian functions curves of the Raman spectrum with different annealing temperatures for one hour. 122
7.5 Tauc Plot of $(\alpha h\nu)^2$ versus photon energy $(h\nu)$ for CZTS for annealed samples at different temperatures for 1 h. The inset shows the variation of energy band gap with annealing temperature. 123
7.6 Top view SEM images of a CZTS thin film deposited on a glass substrate and annealed at 550 °C for (a) 30, (b) 45, and (c) 75 minutes. 125
7.7 SEM image of the film annealed at 550 °C for 75 min. The floor layer with red stars and large grains is indicated by blue stars (magnification of ×1k). 126
7.8 XRD pattern of CZTS thin films annealed at 550 °C for various annealing times. The ICDD-260575 reference spectra is shown in the red stick plot. 127
7.9 The fitting with Lorentzian function curves of the Raman spectra for CZTS samples annealed at 550 °C at different annealing times. 128
7.10 Tauc Plot of $(\alpha h\nu)^2$ versus photon energy $(h\nu)$ for as-deposited and annealed CZTS thin films at 550 °C for different annealing times. The inset shows the energy band gap as a function of annealing time. 129

List of Tables

5.1 The chemical composition of CZTS thin films at various reaction times. 80

5.2 Lattice parameters, FWHM, and crystal scattering domain size for CZTS thin films at different reaction times. 80

5.3 Chemical composition for CZTS thin films at different reaction temperatures (RT) at a reaction time of 30 min. 83

5.4 Lattice parameter, FWHM, and scattering domain size for deposited CZTS thin films synthesised at different reaction temperatures. 85

5.5 Variation of optical band gap with the variation of reaction temperatures 89

6.1 The peak intensity, lattice parameters a and c, FWHM, and scattering domain size of CZTS thin films at different preheating times. 93

6.2 The peaks identified in the Raman spectra of annealed samples at various temperatures. 104

7.1 The composition of the CZTS thin films annealed for one hour at different annealing temperatures. 118

7.2 XRD lattice parameter, FWHM of (112) diffraction peak, and scattering domain of as-deposited CZTS thin films and after annealing at different temperatures for one hour. 121

7.3 CZTS thin film compositions at annealing temperatures of 550 °C and different annealing times. 124

7.4 Lattice parameters, FWHM, and scattering domain size of CZTS thin films as-deposited and annealed at 550 °C for various annealing times. . 127
7.5 Phase analysis of the measured spectra at different annealing times. . . 128

Chapter 1

Introduction

1.1 Research motivations

Solar energy technologies are considered to be one of the most promising alternatives to fossil fuels to meet the rising demand for clean and renewable energy [1]. Humanity needs to meet the electrical power generation of 30 TW by 2050 without carbon emissions associated with the expected increase in global warming demand [2]. Photovoltaics have great potential to meet future electricity supply [2], it uses sunlight to generate electricity. With the increase of problems of global warming attributed to CO_2 in the Earth's atmosphere, from emissions due to the use of fossil fuels, development of renewable energy, and particularly solar energy now has great urgency [3]. The Earth intercepts 174,000 Terawatts of incident solar radiation in the upper atmosphere. Since about 30% of solar radiation is reflected back to space, the rest of solar radiation is absorbed by the Earth's atmosphere, land masses, and oceans approximately 3,850,000 EJ per year. The solar energy received on the Earth's surface in 1 hour is more than that currently used by the world in 1 year [4]. The solar spectrum involves electromagnetic radiation that is emitted by the sun. Figure 1.1 shows the solar radiation spectra at both the top of the earth's atmosphere and sea level. The energy flow within the sun results in a surface temperature of 5800 K, so the spectrum of the radiation from the sun is similar to that of a 5800 K blackbody. The effect of the atmosphere on energy dens-

ity of solar radiation can be measured by the air mass factor AM, which is defined as optical path length through the earth's atmosphere. The spectra are labeled AM0, which corresponds to the spectrum of the sun outside the atmosphere. AM1 indicates the sun is directly overhead. AM1.5G which corresponds to the solar spectra at the earth's surface is used as the standard radiation density for measuring the efficiency of solar cells. The AM0 and AM1.5 spectra are shown in Figure 1.1 [4, 5]. The Air Mass is related to the angle of incidence θ by $AM = 1/\cos\theta$. AM1.5G corresponds to an energy density of 1 kW m^{-2}. Solar cells must absorb a range of energy that corresponds to the solar spectrum in order to be efficient. The solar spectrum has a wavelength range of 100 nm to 1mm, but most irradiance occurs between 250 nm and 2500 nm as shown in Figure 1.1, with the maximum in the visible region of light (400-700 nm) for air mass AM0, indicating that solar cells should strive to absorb as much as possible in the visible region of the solar spectrum [6].

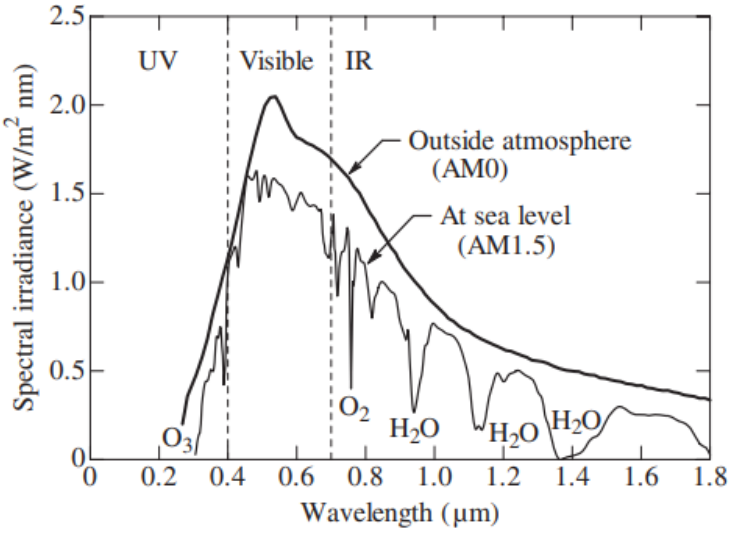

Figure 1.1: (AM0) spectra at the top of the earth's atmosphere and (AM1.5) at sea level [5].

The conversion efficiency of a solar cell is the percentage of power converted from sunlight to electrical energy. The efficiency of a single absorber layer is theoretically calculated using the Shockley-Queisser efficiency (SQ) limit as a function of the semiconductor band gap [7]. it can be determine By calculating the amount of

electrical energy extracted per photon of incoming sunlight. Figure 1.2 shows the dependence of the single-layer efficiency of various semiconductors on band gaps. It is clear from Figure 1.2 that in order to achieve high photon absorption, absorber materials must have band gaps in the range of 1.1 to 1.5 eV. This results in a theoretical maximum efficiency of 32% under typical AM1.5G conditions. However, When solar radiation with different wavelengths reaches the earth, the photon with energy less than the solar cell absorber layer band-gap energy (E_g) will not be absorbed in the semiconductor. The photon having energy higher than the energy gap of the semiconductor will be absorbed in the semiconductor and then excite an electron from the valance band to the conduction band. The photon having excessively high energy can excite an electron at the higher conduction band state, however, the excited electron will relax quickly via thermalisation toward the conduction band edge states via the electron-phonon interaction. These factors can reduce the SQ limit for solar cells. Figure 1.2 plots the SQ efficiency limit versus E_g, the theoretical SQ efficiency limit shows a maximum near E_g=1.3 eV at 32% [5]. Experimentally, the highest efficiency achieved for monocrystalline Si in 2014 [4] was 25% still well below the SQ limit. According to the Shockley-Queisser model, the efficiency under standard AM1.5 conditions with a band gap in the range 1.3-1.5 eV, the maximum theoretical efficiency can be determined as 32% for a single-layered cell [8]. Hence suitable material with an energy gap in this range includes CdTe and CIGS which are achieving two-thirds of this limit. CZTS is quite closely related to CIGS where the expensive and scarce elements indium and gallium are replaced by 50:50 of zinc and tin [9].

The range of solar cells continues to expand making progress in laboratory efficiencies. Thin film technologies are achieving around two-thirds of SQ limits such as CdTe and CIGS [11]. There is a need to expand the range of materials that are available for thin film solar cells, by the emphasis on cheap, sustainable, and non-toxic materials such as copper zinc tin sulfide.

Crystalline Si-based solar cells are the dominant photovoltaic technology and con-

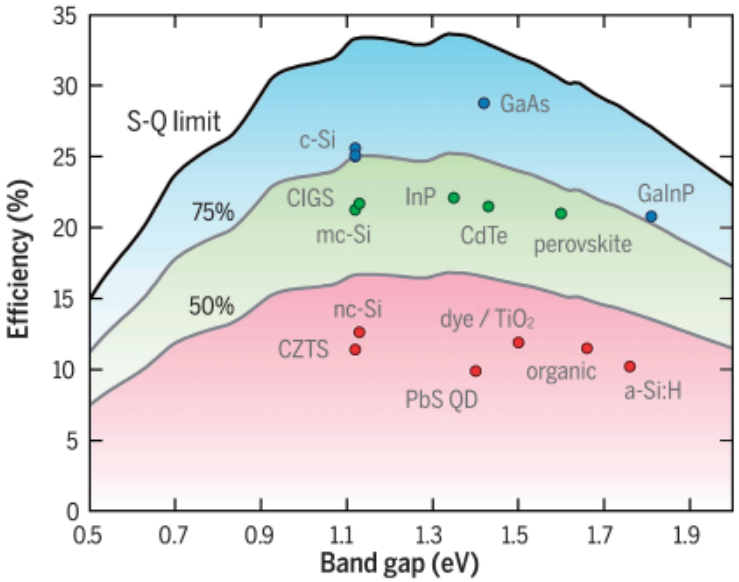

Figure 1.2: Efficiencies of different semiconductors shown against the Shockley–Queisser limit [10].

stitute around 85% of the world's photovoltaics. However the high cost of solar cell fabrication based on Si, and the degradation of their performance over time mean that lower cost alternatives are required [12]. Silicon also has the disadvantage of being an indirect bandgap semiconductor, requiring much thicker layers to absorb the sunlight, typically 200-300 μm [13]. In contrast most thin film devices are fabricated from direct bandgap devices. Therefore, next-generation solar cells based on chalcogenide-based thin film photovoltaics such as CdTe and CIGS have the potential to reduce the cost of photovoltaic technologies. This technology is an alternative method to overcome these disadvantages as they reduce the thickness of the absorber layer by a factor of over 100. CdTe and CIGS technologies exhibit conversion efficiencies beyond 17.7-21.7% [7, 12, 14, 15, 16, 10], and many other common thin film materials have efficiencies in the 10 to 13% range [10]. Thin-film solar cell is a second generation technology, The thickness of the film can vary from several nanometers to tens of micrometers, which is thinner than first generation c-Si solar cell with a 200 μm thick wafer [17]. However, these chalcogenide based materials are unable to meet world electricity demand because of the usage

of rare-earth elements for CIGS [15], and the toxicity of Cd in CdTe. Also the relative abundance of some of the constituent elements is low and won't meet the demand for growing solar PV. Therefore, cost and environmental considerations are important for the economical production of electricity. To solve these problems, it is necessary to develop new materials that are based on earth-abundant and non-toxic elements. Recently, more attention has been paid to the I2-II-IV-VI4 family, such as Cu_2ZnSnS_4 (CZTS) [18]. This material has many advantages, such as being earth-abundant and eco-friendly material, and has similar properties to CIGS [15, 11]. However, gallium (Ga) and indium (In) are expensive and relatively rare elements. The abundance of indium in the upper continental crust is estimated to be 0.16 ppm. In contrast, copper zinc tin sulphide (CZTS) is composed of abundant elements in the Earth's crust (crust abundance of 68 ppm, 79 ppm, 2.2 ppm, and 420 ppm for copper, zinc, tin, and tin and sulphur respectively)[18]. CZTS semiconductors are potential candidate materials for terawatt (TW) scale photovoltaic conversion [7]. CZTS semiconductors have emerged as one of the most promising materials for thin film photovoltaic which meet the electricity consumption with a cost reduction. CZTS compounds combine with suitable optical and electronic properties for solar energy conversion. CZTS can be obtained from the chalcopyrite CIGS structure by replacing the In/Ga with Zn and Sn found in the kesterite structure [19]. CZTS has a Kesterite crystal structure and with a direct band gap of 1.0-1.5 eV, is nearer to the optimum band gap of a photovoltaic device. In addition, it has a very high absorption coefficient greater than 10^4 cm^{-1} in the visible light region [1] [20]. Because of the large absorption coefficient of CZTS thin film, a layer of micron thickness can absorb sunlight sufficiently. Moreover, all elements Cu, Zn, Sn, and S are low-cost, earth-abundant, and non-toxic. However, cost-effective solar cell production not only requires the use of earth-abundant materials, such as CZTS, but also needs economical fabrication methods. Fabrication methods of CZTS absorber layers can be classified into vacuum-based and non-vacuum-based techniques. Vacuum-based techniques, such as evaporation and

sputtering, generally require a large capital investment and a high amount of energy to deposit thin films from the target sources. Non-vacuum-based techniques, on the other hand, are less expensive, use less energy, and produce uniform thin films. The efficiency of CZTS solar cells has achieved a record efficiency of 7.2% for devices grown by hot-injection synthesis of nanocrystal absorber Cu_2ZnSnS_4 [21] and 9.66% for $Cu_2ZnSn(S, Se)_4$ thin-film solar cell using the hydrazine-based solution [22]. The highest power conversion efficiency was reported at 12.6% in 2014 using solution deposition of chalcogenides dissolved in hydrazine followed by annealing, but hydrazine is a highly toxic and unstable compound [2, 11, 20, 21]. Non-vacuum methods such as solution-based deposition have shown the potential of this technique for the cheap manufacturing of efficient solar cells that consist of earth-abundant elements [19]. A non-vacuum deposition approach has recently achieved a 9.0% efficiency via the selenisation of CZTS nanocrystals [23]. The highest power conversion efficiencies by solution-processed techniques have been recorded for CZTS with record efficiencies reaching 12.6% compared to 9.7% for vacuum-based methods [24, 2, 25, 26]. The non-vacuum-based techniques follow the general solution-processing route, where ink is deposited as a thin film, followed by a thermal treatment to get large grains. The nanoparticle ink approaches have the potential to control phase formation, surface properties, and particle size of the nanoparticles. It is possible to use simple deposition processes such as spin-coating and dip-coating as well as screen printing and ink-jet printing with an ink-based technique [27]. In the present work, Cu_2ZnSnS_4 (CZTS) nanocrystals was synthesized by using metal chloride precursors [16, 25, 26]. The hot injection technique is considered an effective method of forming CZTS thin films uniformly for the economic production of CZTS thin film solar cells. The structural, morphological and optoelectrical properties of CZTS nanocrystals can be controlled by optimizing synthesis parameters such as reaction temperature, reaction time, precursor concentrations, etc. Despite the advantage of CZTS as an absorber material for solar cells, solar cells based on CZTS exhibit relatively low efficiencies. CZTS cells suffer

from low optoelectronic properties mainly due to the high carrier recombination in bulk and at the interface between the absorber and buffer layers. In addition, the presence of various secondary phases and defects are the main hindrances in achieving the target device performance. Secondary phases such as ZnS, SnS, and Cu_2SnS_3 that appear on the surface of the CZTS and at the back contact interface. The SnS phase has a lower bandgap than the CZTS phase and could modify the interface properties. While the ZnS phase can block the current flow, the high concentration of zinc in the solar cell might act as a resistive barrier for carriers, which affects the performance of the solar cell.

1.2 Aims of the study

The aims of this study is to optimise the experimental process for the fabrication of CZTS nanoparticle inks by using the hot injection method and spin coating deposition techniques to produce high-quality CZTS absorber layers and to study the effect of different synthesis parameters such as temperature and time on the structural and optical properties of CZTS thin films. Also, to investigate the impact of the annealing parameters such as temperature, and time on the structure, morphological and optical properties of CZTS thin films structural and optical properties of CZTS thin films.

1.3 Thesis outline

This thesis is divided into eight chapters. Following the introduction, Chapter 2 presents a general background of the theory of solar cells. Chapter 3 is an overview of CZTS-based thin film solar cells. It deals with thin film solar cells having an optical absorber layer composed of CZTS-based quaternary semiconductors. It describes the thin film solar cell fabrication from CZTS nanocrystals and reviews CZTS properties and technologies to produce CZTS nanocrystal nanoparticle ink-

based deposition techniques, such as drop casting and spin coating techniques and fabrication of full devices. The chapter ends by describing the characterisation techniques for CZTS thin films in this work. Chapter 4 provides an overview of the CZTS nanocrystal synthesis process using the hot injection method and the deposition of the resultant CZTS ink to fabricate thin films. A description of the techniques used for the characterisation of CZTS thin films follows. Chapter 5 describes the synthesis of CZTS thin films from nanocrystal inks and studies the effect of synthesis reaction conditions such as temperatures and time of the growth on CZTS nanocrystals and their impacts on phase purity, defect formation, and homogeneity in growing crystals. The Chapter describes how thin film deposition methods determine the structure, phase purity, morphology, and optical properties of the CZTS thin films. XRD diffraction is used to determine the crystal structure and determine lattice parameters, Raman spectroscopy for phase purity of CZTS nanocrystals, SEM, FIB for structural characterisation, and compositional analysis of nanocrystals. Lastly optical characterisation of CZTS thin films using ultraviolet-visible spectroscopy (UV-vis) is described to estimate the energy gap of CZTS thin films. Chapter 6 investigates preheat treatment and sulphurisation effect on spin-coated CZTS thin films, and Mo/CZTS/CdS heterojunctions Electron microscopy and EDX imaging is used to quantify element interdiffusion throughout the heterojunction. Chapter 7 describes the annealing of CZTS thin films, deposited by drop casting techniques, in the H_2S+N_2 atmosphere and the effect of annealing parameters such as temperatures and times on structural, morphological and optical properties of thin films. Chapter 8 reports the conclusions from the work and provides suggestions for further work.

Chapter 2

Thin-film solar cells

2.1 Development of solar cells

Over the past century, there has been a significant rise in the world's energy demand, and due to the recent rapid industrial and population growth. In this environment, solar energy is rapidly expanding among renewable energies, which is important for the sustainability of human society. Various technological approaches for solar PV have been developed over the years. There are three different generations of solar cells, as presented below.

2.1.1 The first generation solar cell

Single-crystalline silicon (sc-Si) and multi-crystalline silicon (mc-Si) cells, as well as conventional panels with crystalline silicon (c-Si) bases, are included in the first generation [28]. Silicon wafers dominate the solar cell markets, accounting for 80% of the market due to their relative high power efficiency and established manufacturing [6][29] . Despite this generation's high efficiency, elemental abundance, durability, and non-toxicity, it still needs high-temperature processing, and has significant manufacturing costs. c-Si technology is suitable to reduce PV module cost but is less efficient than sc-Si cells and too expensive for large-scale operation, and c-Si modules only interact weakly with light because Si is an indirect bandgap

semiconductor, that requires over 200 μm of material to absorb the solar spectrum.

2.1.2 The second generation solar cell

The second-generation solar cells are based on thin-film solar cells that use amorphous silicon (a-Si), cadmium telluride (CdTe), gallium arsenide (GaAs), copper indium selenide (CIS), copper indium gallium selenide (CIGS), and cadmium sulphide. On the other hand, due to the scarcity and toxicity of certain elements such as (In,Ga) or toxic element such as cadmium [30] make new materials with kesterite structure such as CZTS more attractive in thin film photovoltaic. Theoretical studies showed that the CZTS-based solar cell has a conversion efficiency of more than 30%, BUT the highest efficiency that has been reached so far is 12.6% [31][32][33].

2.1.3 The third generation solar cell

A new generation of solar cells emerged due to the high costs of the first generation and the toxicity and limited availability of materials for the second generation solar cells. The third generation of solar cells differs from the first two because they do not rely on the p-n junction structure [6] . This generation uses materials and compounds that potentially reduce production costs when compared to Si-Wafer solar cell technology [29]. It can be represented by four types: dye-synthesized solar cells, organic/polymer solar cells, nanostructured quantum dot solar cells, and perovskite solar cells[29].

2.2 The photovoltaic effect

A solar photovoltaic (PV) cell is an electronic device that uses semiconductor materials to convert solar energy to electrical energy. Electrons flow in this cell when photons (energy packets) from sunlight are absorbed and electrons from the valence band of the semiconductor material are excited to the conduction band, forming

a hole that is then inhabited by another electron. This whole process is known as the photovoltaic (PV) effect [34]. The active section of each solar cell consists of two layers that form a $p-n$ type junction of semiconductor materials, which is the underlying basis of electron hole pair creation and separation. The photovoltaic cell is the fundamental component of a solar power generation system and is responsible for the direct transformation of light into usable electricity. A $p-n$ junction shown in Figure 2.3, p-type layer of a $p-n$ junction has holes as the majority charge carriers and electrons as the minority charge carriers. In the n-type layer, electrons are the majority charge carriers, whereas holes are the minority charge carriers.

Several independent works of literature have been written about the development of solar cells in relation to amorphous silicon (a-Si), copper indium gallium selenide (CIGS), and cadmium telluride (CdTe). Due to their low production costs, minimal material requirements, and promising efficiency growth, thin-film solar cells are quickly becoming the preferred technology. The process of fabricating a thin-film solar cell requires depositing one or more thin layers of material onto a material like glass, plastic, or metal. The film thickness can range from several nanometers to tens of micrometers [35, 36], making it thinner than standard first-generation c-Si solar cells (200 μm thick wafers). Because of this, thin-film photovoltaic cells are flexible and light; cadmium telluride and copper indium gallium diselenide are the two most common types of thin-film PV semiconductors currently available. Due to its excellent absorption spectrum and ideal 1.5 eV band gap, CdTe has emerged as one of the best materials for creating solar cell devices. CdTe and CIGS technologies exhibit conversion efficiencies beyond 20% efficiency [10] [16] [15] [37]. In recent years CZTS-based thin-film solar cells have come to the attention of a significant number of researchers for a variety of reasons, including their high absorption coefficient, appropriate band gap (1.4–1.5 eV), and low cost.

2.3 Characteristics of photovoltaic materials

2.3.1 Absorption coefficient

A thin absorption layer with a high absorption coefficient is required for thin-film solar cells. The material's absorption coefficient should be high, around 10^4-10^6 cm^{-1}. Higher absorption coefficient materials can easily absorb photons and thus excite electrons into the conduction band . Indirect band gap semiconductors have lower optical absorption than direct band gap semiconductors. Si indirect band semiconductors have a lower absorption coefficient, therefore the thickness of the absorption layer should be greater than 200 μm [38]. The absorption coefficient α is a frequency-dependent and material-specific parameter, The absorption coefficient can be calculated experimentally from the reflectance R and transmittance T using the relation:

$$\alpha(\lambda) = \frac{1}{x} ln \frac{1 - R(\lambda)}{T(\lambda)} \tag{2.1}$$

Where, x is thickness of the film.

2.3.2 Band gap

The band gap is the minimal amount of energy needed to excite an electron in a semiconductor valence band to a higher energy state. Only photons with energies larger than or equal to the band gap of a material can be absorbed. Material should have a band gap that is suitable for the solar spectrum. If the band gap is too narrow, a great deal of the extra energy will be released as heat via thermalisation. However, if the band gap is too wide, many photons with insufficient energy will pass through the material without producing an electron-hole pair. The energy bandgap should be between 1-2 eV for effective solar energy collection [34, 38]. In a semiconductor, there are two types of band gaps: a direct band gap and an indirect

band gap. In a semiconductor with a direct band gap, the maximum in the valance band and the minimum in the conduction band occur at the same wavevector k; thus, valence band electrons can be excited directly to the conduction band with a high probability by only a photon. Hence, the absorption coefficient is high, and as a result, the absorption depth for solar radiation is small, typically 1 μm [39]. In an indirect band semiconductor, the valence band maximum and conduction band minimum are displaced along different k-axes. Therefore, optical absorption at the band gap also involves the participation of a phonon to provide momentum conservation. Thus, this three-body process results in a lower transition probability and hence a longer absorption depth for solar radiation, typically >100μm. The processes of direct and indirect band gaps are described in Figure 2.1. The band-gap is the most significant feature of a photovoltaic materials, The band gap should be near-optimal band-gap value of 1.5 eV.

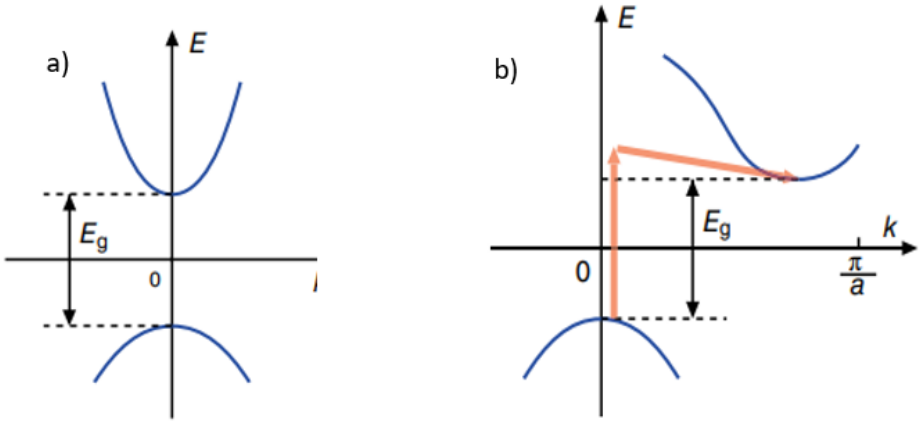

Figure 2.1: E vs. k curve of a direct (a) and indirect (b) band gap semiconductor [40].

The absorption coefficient of a direct-gap semiconductor can be expressed by

$$\alpha(\hbar\omega) = K(\hbar\omega - E_g)^{\frac{1}{2}} \tag{2.2}$$

The Beer-Lambert Law gives the absorption depth x for a thin film:

$$I = I_0 \exp(-\alpha x) \tag{2.3}$$

where I_0 is the incident radiation intensity, I is the intensity after traversing a depth x, and α is the wavelength-dependent absorption coefficient [40]. The absorption coefficient is related to the energy density of states in the conduction and valence bands. Thin-film solar cells made from direct band gap semiconductors absorb light in a much thinner region, allowing them to be made with a very thin layer as thin as 1 μm. In contrast to indirect-band semiconductors, where the value of the absorption coefficient α is small, Therefore, a thicker absorber layer is needed, typically hundreds of microns thick. Figure 2.2 shows the absorption coefficients of different semiconductors as a function of photon energy.

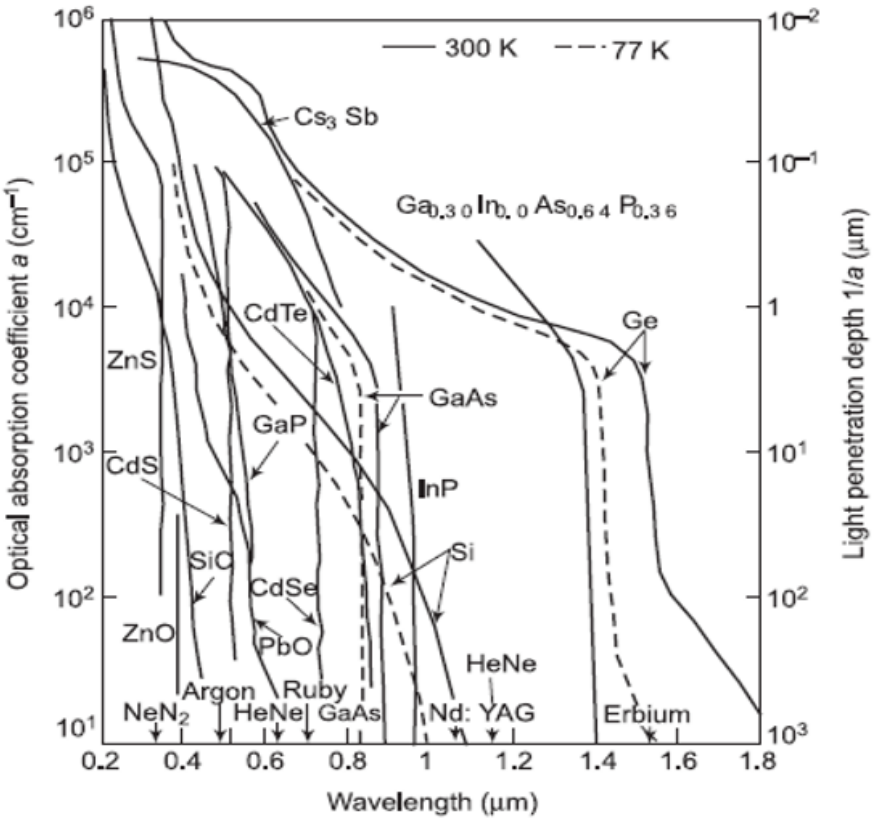

Figure 2.2: Absorption spectra of various semiconductors [39]

Thin films of high absorption coefficient semiconductors can be utilized to produce

power that is equivalent to, or greater than that produced by thick films or wafers of low absorption coefficient semiconductors as is the case in crystalline silicon, c-Si , the absorption coefficient for Si with an indirect band gap is around 10^2 cm^{-1}, the light penetration depth is greater than 100 μm. In contrast, with a thin film such as CZTS with a high absorption coefficient of around 10^4 cm^{-1}, the penetration depth is around 1 μm. Therefore, a direct-gap semiconductor with a direct band gap, can enhance the energy conversion efficiency of a thin-film solar cell [40].

2.4 Theory of $p-n$ junction

The semiconductor used in a $p-n$ junction for the p-type and n-type parts can be the same material that has been doped with p and n dopants; this is a $p-n$ homojunction. This means that the band gap is uniform throughout the material, with the only difference being the type of carriers present. Thin film solar cells are usually $p-n$ heterojunctions, where the absorber and window layers are different semiconductor materials, rather than homojunctions. A heterojunction is formed by combining non-identical p-type and n-type semiconductors. This means that the band gap is no longer homogeneous. A solar cell consists of a semiconductor $p-n$ junction with a band gap E_g to provide the built-in electric field that separates the charge carriers. A $p-n$ junction is formed when a p-type semiconductor comes into contact with an n-type semiconductor. Excess holes and electrons will diffuse to the opposite side of the junction along the concentration gradient, which means excess holes on the p-side diffuse to the n-side and excess electrons on the n-side diffuse to the p-side. At the same time, the negatively charged fixed acceptor ions on the p-side and the positively charged fixed donor ions on the n-side near the junction are left in the semiconductor, resulting in an electron field at the junction, and as a result, the depletion region is created as shown in figure 2.3. In this region, the direction of the electric field is from the n-side to the p-side, which opposes the majority carrier diffusion process. At the same time, the minority

carriers that reach the junction can drift across the depletion region and become majority carriers in the other type. When the diffusion and drift currents are equal, the current across the junction will reach zero.

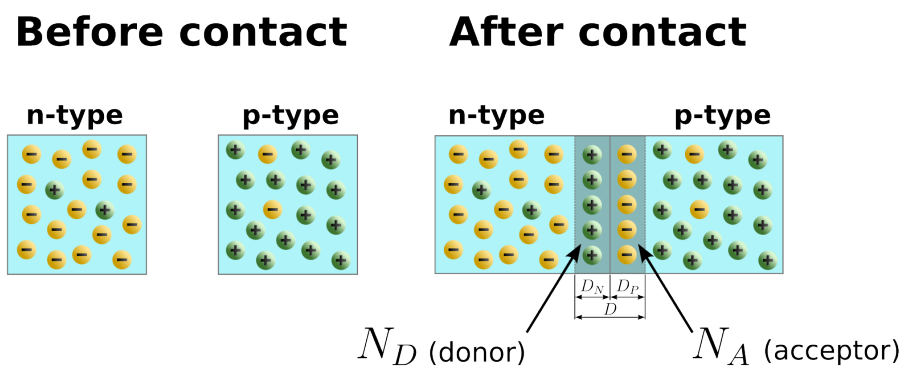

Figure 2.3: A p-type semiconductor comes in contact with an n-type semiconductor to form a $p-n$ junction.

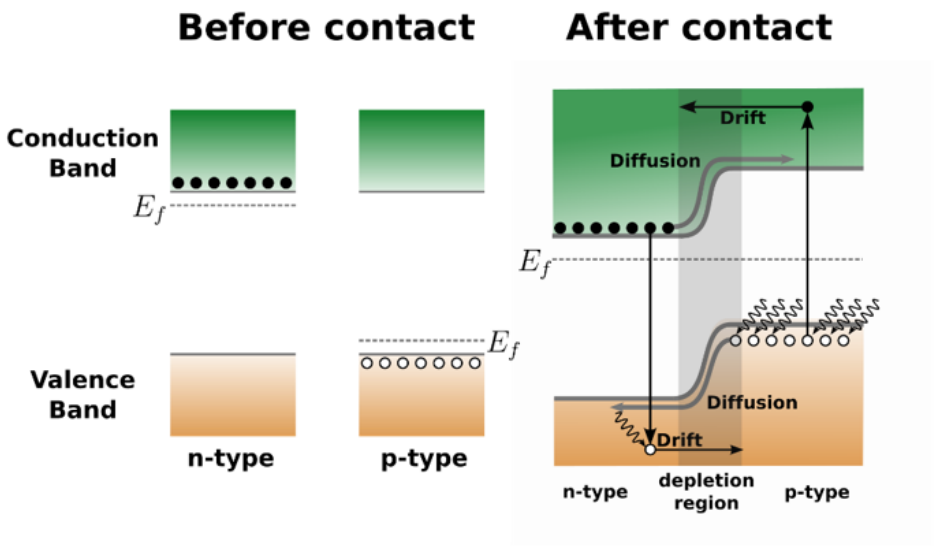

Figure 2.4: Band diagram of a $p-n$ junction before and after contact.

Figure 2.4 shows band diagram of a $p-n$ junction before and after contact. A built-in potential difference exists between the two regions because of the electric

field and the realignment of Fermi level and can be defined as

$$V_{bi} = \frac{kT}{q} \ln\left(\frac{N_A N_D}{n_i^2}\right) \tag{2.4}$$

where N_A, N_D are acceptor and donor concentrations, respectively, n_i is the intrinsic carrier concentration. The depletion width is given by

$$W = \sqrt{\frac{2\varepsilon_s V_{bi}}{qN_B}} \tag{2.5}$$

where ε_s is semiconductor permittivity, V_{bi} is the built-in voltage, N_B is the doping concentration, and V is the built-in bias across the junction. The width of the depletion region also depends on the external bias across the junction and can be given by:

$$W = \sqrt{\frac{2\varepsilon_s(V_{bi} - V)}{qN_B}}. \tag{2.6}$$

V is positive for forward bias and negative for reverse bias. Forward bias decreases the depletion region width, and reverse bias increases the depletion region width, as shown in figure 2.5.

In the dark, a solar cell has the same voltage-current characteristic as a diode. The diode current can be expressed by the Shockley diode equation; the current density diverted through the diode is:

$$J = J_s\left[\exp\frac{qV}{AkT} - 1\right] \tag{2.7}$$

where J_s is the diode saturation current density, A is the diode ideality factor, k is the Boltzmann constant, and T is the absolute temperature. Under illumination, the current density-voltage curve of the solar cell is shifted downward because of the light-generated current opposing the diode dark current, and the total current density is

$$J = J_s\left[\exp\frac{qV}{AkT} - 1\right] - J_L \tag{2.8}$$

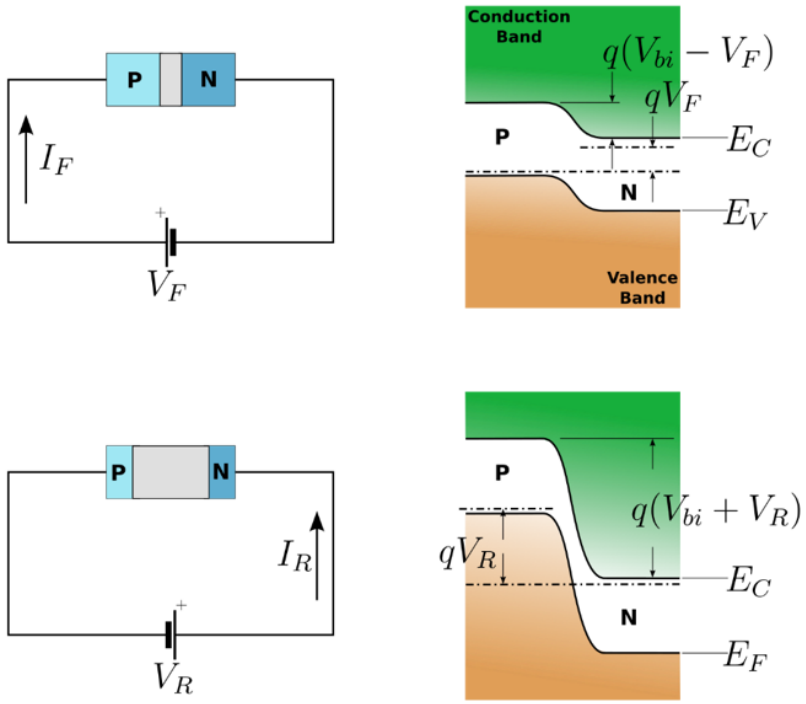

Figure 2.5: Forward and reverse bias energy band diagrams of a $p - n$ junction.

where J_L is photo current [41]. The current density-voltage characteristics for a solar cell operating in the dark and under illumination are shown in Figure 2.6.

2.5 Device characterisation

2.5.1 Current-voltage measurement

The I-V curve can be used to determine the parameters of a solar cell and determine the efficiency of the solar cell. From the J-V curve, the solar cell parameters are determined, such as short circuit current J_{sc}, open circuit voltage V_{oc}, and fill factor FF, as shown in figure 2.6. V_{oc} is the maximum voltage at which no net current (zero current) is flowing across the device and can be expressed by:

$$V_{oc} = \frac{AkT}{q} \ln\left(\frac{J_L}{J_0} + 1\right). \tag{2.9}$$

Whereas current density (J_{sc}) is the maximum current that a solar cell can produce at zero voltage. The voltage and current along this curve where the solar cell produces the most power is known as the "maximum power point". The fill factor is a measure of the curve's squareness. The fill factor is the ratio between the maximum possible power generated by a solar cell and the actual power of the solar cell with no series resistance and infinite shunt resistance, as follows:

$$FF = \frac{J_{MP}V_{MP}}{J_{SC}V_{OC}} \tag{2.10}$$

The conversion efficiency of the solar cell is the ratio between the maximum generated powers and the incident power [19, 23], as given by the following formula:

$$PCE = \frac{P_{out}}{P_{in}} = \frac{J_{SC}V_{OC}FF}{P_{in}} \tag{2.11}$$

where P_{out} and P_{in} are the output power and input power of the cell, respectively, J_{sc} and V_{oc} are the short-circuit current density and open-circuit voltage, respectively. V_{MP} and J_{MP} are the voltage and current density of the solar cell at maximum power, respectively. The low performance of solar cell is due to low fill factor (FF) and open-circuit voltage (V_{oc}).

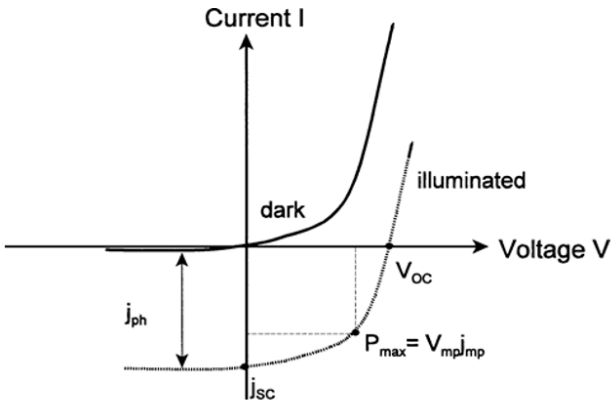

Figure 2.6: Current-Voltage characteristic of a solar cell In the dark and under illumination and showing solar cell parameter [42].

The series resistance is minimized to avoid a decrease in device efficiency due to increased charge carrier resistive losses. The shunt resistance should be as high as possible by reducing current leakage through recombination losses. The equivalent circuit of a real solar cell is presented in Figure 2.7 [39, 43]. The current density of the equivalent circuit is given by

$$J = J_s \left[\exp \frac{q(V - JR_s)}{AkT} - 1 \right] + \left(\frac{V - JR_s}{R_{sh}} \right) - J_L. \tag{2.12}$$

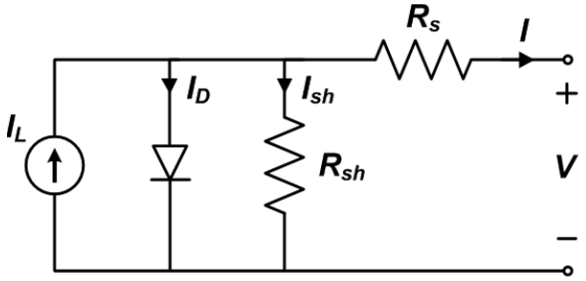

Figure 2.7: Equivalent circuit for a real solar cell [44].

2.5.2 External quantum efficiency

External quantum efficiency (EQE) which is calculated as electrons generated divided by photons incident on the device, and is a measurement of how well a solar cell converts an incident photon into an electron. The measurement is carried out by keeping records of a solar cell's current response to light that is monochromatic across a wide spectrum of wavelengths. It's described by

$$\mathrm{EQE}(\lambda) = \frac{I_L(\lambda)}{qN(\lambda)} \tag{2.13}$$

Here, N is the quantity of photons that were incident on the cell, q is the charge of an electron, and I_L is the current produced by the light as a function of wavelength. Various portions of the EQE curve indicate information about different loss mechanisms in the device.

2.6 Losses in a solar cell

The performance of solar cells is limited by a variety of losses. Below are descriptions of the many losses that can occur in a solar cell and lower its efficiency.

2.6.1 Optical losses

It is possible for a device to suffer energy losses, which lowers its efficiency. In a typical $p-n$ junction solar cell, figure 2.8 shows five different loss mechanisms in $p-n$ junction [45, 46, 47, 48]. (1) Some of this light might be absorbed by the contacts, or it might be reflected by the surface of the cell. When a photon hits the junction, the bandgap of the absorber layer serves as a filter for the photons that are coming in. Solar radiation: photons whose energy is equal to or higher than the bandgap are absorbed, and photons with energies less than the bandgap are transmitted through the absorber material. (2) The thermalisation of electron-hole pairs caused by short wavelength photon absorption via electron (hole) relaxation near the conduction (valence) band edge. Other losses include junction loss (3) and contact loss (4), both of which in an ideal device can be arbitrarily small. Recombination loss (5), which can occur because of states formed within the bandgap that allow charge carriers to recombine via this extra state, these states can occur because of material defects and grain boundaries [38, 41, 49].

2.6.2 Recombination losses

These losses result from recombination in the depletion region as well as surface and bulk recombination at the metal or semiconductor interface. Impurities and defects act as traps for photoexcited carriers [50, 51, 52]. Therefore, recombination on these traps causes a decrease in photocurrent and has an impact on the open-circuit voltage [53].

2.6.3 Metal/semiconductor interface

The front and back surfaces of a solar cell's metal/semiconductor interactions result in losses. One of the key methods to reduce the power losses in cells is to reduce the resistance of the metal/semiconductor interface.

2.6.4 Resistance losses

Due to the negative impact of a large value of series resistance on short-circuit current, solar cells with a low value of series resistance tend to be more efficient. To maximise the open circuit voltage, the shunt resistance should be high. The efficiency and fill factor of a solar cell are both diminished by the presence of resistance losses, both in series and in shunt [54].

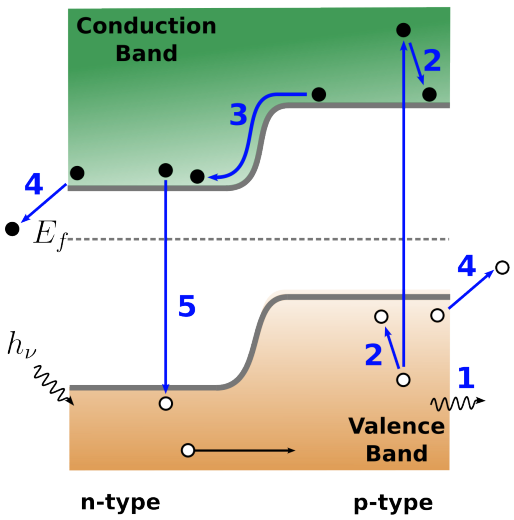

Figure 2.8: The loss mechanism in a typical $p-n$ junction solar cell.

Chapter 3

Copper zinc tin sulphide (Cu_2ZnSnS_4)-based thin-film solar cells

3.1 Introduction

Thin-film solar cells are attractive due to their low material cost, low synthesis cost, and a promising trend in efficiency increase. Figure 3.1 shows NREL's photovoltaic efficiency records for several solar cell technologies. Thin film solar cell technology has developed rapidly, including Si, CdTe, GaAs, Cu(In,Ga)Se_2, and others. Chalcopyrite-based Cu(In,Ga)Se_2 is one of the most promising materials for thin-film solar cells [55]. c-Si and pc-Si wafers make up about 80% of the current solar market [56]. In today's market, copper indium gallium diselenide (CIGS), copper indium diselenide (CIS), cadmium telluride (CdTe), gallium arsenide (GaAs), and copper-zinc sulphur (CZTS) are the most used thin-film materials. However, with rare indium in CIGS, and toxic arsenic and cadmium in gallium arsenide and cadmium telluride respectively, CZTS is one of the most promising candidates in renewable energy harvesting and makes it competitive with CIGS thin-film solar cells in the longer term. The material cost of a solar cell can be reduced

by using earth-abundant elements, making the CZTS-based thin-film solar cell a photovoltaic device that has the potential to provide a considerable amount of low-cost electricity. A CZTS thin film has an optimum direct band gap of 1.4-1.5 eV and a high absorption coefficient of 10^4 cm^{-1} which will be suitable with multiple layer-based structures when employed as the absorption layer of thin film-based photovoltaics [57]. The high absorption coefficient of CZTS suggests that the solar cell can be produced in thin-film form with less material used in the fabrication of the cell. The energy conversion efficiency of an ideal solar cell consisting of CZTS, which is theoretically calculated by Shockley–Queisser (SQ) relation, is equal to 32.2%, see section 3.4 [57, 58]. However, the best reported experimental efficiency achieved by a solution method is only 12.6% [59, 60, 61]. This huge gap between the theoretical and experimental power conversion efficiencies can be attributed to several factors, such as the lack of stoichiometric control, the difficulty of producing single-phase CZTS without a secondary phase, and the complicated nature of the bulk and surface defects [62]. The next technological target for the CZTS-based thin film solar cell could be set for the achievement of half the theoretical limit, which is high enough to cut the balance of system cost per peak watt.

3.2 Crystal structure of CZTS

3.2.1 Structure of kesterite and stannite Cu_2ZnSnS_4

At room temperature and normal pressure, most I2-II-IV-VI4 semiconductors crystallize into tetragonal or orthorhombic structures. The tetragonal semiconductors crystallize either in the kesterite or stannite structure. The physical, chemical, and optical properties of CZTS are controlled by the synthesis process and resulting crystal stoichiometry. The structure desired for photovoltaic applications is kesterite, as it is the most thermodynamically stable structure. These structures are closely related but assigned to different space groups due to different distributions of the cation atoms Cu and Zn. However, it's difficult to distinguish whether a

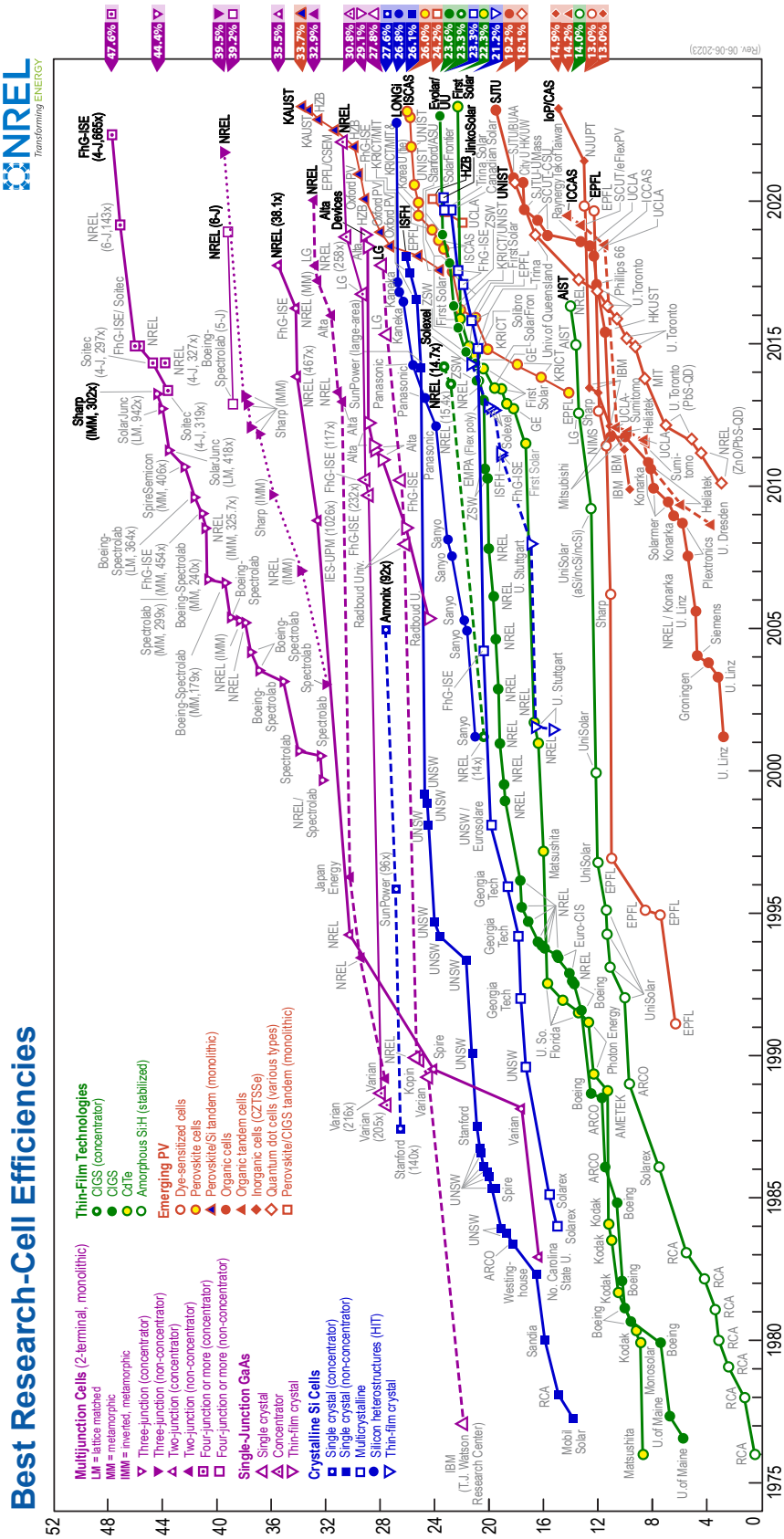

Figure 3.1: NREL *Best Research-Cell Efficiency Chart* showing photovoltaic efficiency records for several solar cell technologies from the NREL PV website [63].

structure is a kesterite or a stannite without using the rietveld refinement process with X-rays as the Cu and Zn are isoelectronic. Many studies indicate that, for CZTS, the kesterite structure is energetically more stable than the stannite structure [64, 65]. The kesterite phase is more stable than the stannite phase and it has 2.86 meV per atom less energy than the stannite structure [66]. The change from kesterite CZTS to disordered kesterite is expected to happen around 260 °C, but neutron diffraction has shown that there is a lot of disorder in all kesterite CZTS samples at room temperature. At elevated temperatures of 866–1002 °C, tetragonal CZTS transforms into sphalerite, a fully disordered cubic structure. In some cases, the sphalerite phase has been found to coexist with the tetragonal phases even at room temperature [67]. Figure 3.2 shows a few examples of the many different crystal structures that CZTS can take. The lattice in the tetragonal crystals can be defined by the two lattice parameters, a and c, where $a = 5.430$ Å and $c = 10.845$ Å at 300K [68].

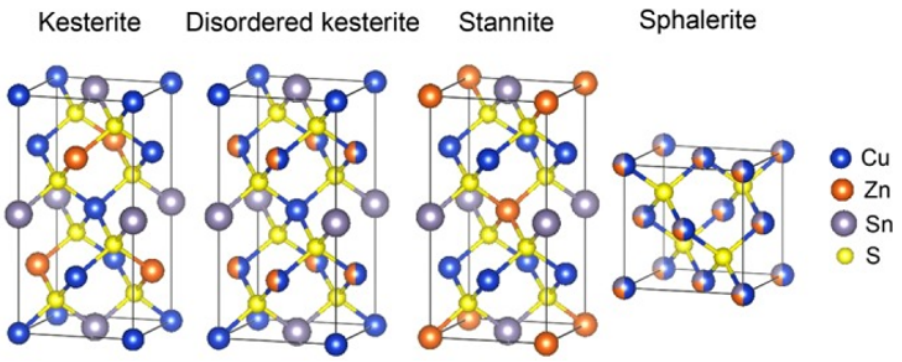

Figure 3.2: 3D perspective view of (a) kesterite-type and (b) stannite-type CZTS structures [64, 67, 69].

3.3 Optical and electronic properties

3.3.1 The band structure

Tetrahedral geometry is identical to group IV, III-V, and II-VI semiconductors in the group I2-II-IV-VI4 molecule. Each anion in this combination has eight electrons

surrounding it, and a closed valence shell creates the four bonds. Figure 3.3 shows clearly the electronic band structure of the quaternary compounds CZTS. In a semiconductor with a direct band gap, the valence band maximum and conduction band minimum both occur at the same crystal momentum value (k-vector) in the Brillouin zone. The band structure plot in 3.3 shows that CZTS has a directly band gap in the range of 1.4-1.5 eV, making it ideal for use in photovoltaics. Because phonons are not involved in the absorption process, this material can be used in thin film devices as a powerful absorber. CZTS with high absorption coefficients of 10^4 cm^{-1} [70] which means that a 1-2 μm thick CZTS film may absorb more than 90% of the incident light in the absence of reflection losses [71, 72]. However, the variation of the energy gap is related to different parameters, such as sample composition and heat treatment parameters like annealing temperature, time, and atmosphere [73]. The band gaps of the thin films were influenced little by the composition [74, 75, 76]. In different investigations researchers found the absorption coefficient increases slightly as the Cu/(Zn+Sn) ratio rises, whereas the band gap reduces from 1.83 to 1.49 eV [76]. In another study, as the [Sn]/[Cu] ratio grows, the band-gap energy shifts from 1.48 to 1.63 [68]. In another study on how annealing affects the energy gap of CZTS, the energy gap of annealed CZTS decreases from 2.2 eV to 1.5 eV, which shows that heat treatment improved the optical properties of annealed samples [77, 78].

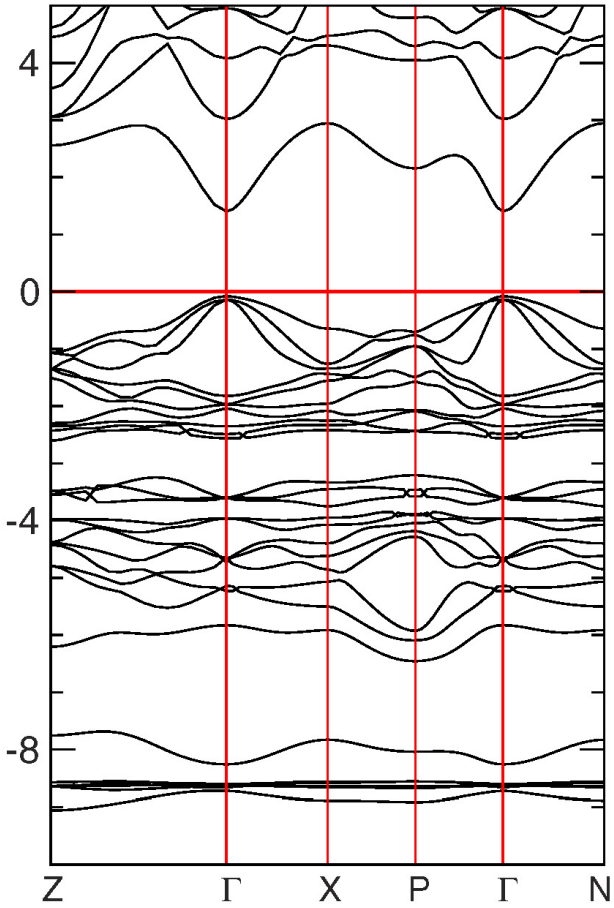

Figure 3.3: Energy-band structure of kesterite-type CZTS [64].

3.4 Thin-film growth methods

Deposition is the process of coating a substrate with a thin layer of material. Recently, different vacuum-based and non-vacuum-based deposition processes have been mainly used to fabricate CZTS films. The strategies focused on the fabrication of straightforward, inexpensive synthesis techniques. The material quality of a CZTS thin film, as well as the overall conversion efficiency of a CZTS solar cell, can be affected by a variety of thin-film deposition techniques. CZTS thin films can be deposited using vacuum or non-vacuum-based techniques. Vacuum-based techniques have been widely used for the deposition of kesterite thin films, such

as solvothermal [79, 80], sputtering [81, 82], thermal evaporation, electron beam evaporation, co-evaporation, and pulsed laser deposition (PLD) [83, 84]. However, these techniques require considerable energy to deposit a thin film at the target sources. In addition, the CZTS is decomposed at higher annealing temperatures because sulphur and tin are both volatile elements [85]. Therefore, solution-based techniques have been used as approaches to grow CZTS without undesirable secondary phases. This technique provides low energy consumption and low cost, such as with electrodeposition ($\eta = 7.3$), co-electrodeposition [86], co-electrodeposition ($\eta = 8.7$) [87], spray pyrolysis ($\eta = 1.15$), nanoparticles ($\eta = 11\%$), spin-coating of precursor solutions, successive ionic layer adsorption and reaction (SILAR) [88], and sol-gel ($\eta = 2.23\%$) [84].

3.4.1 Vacuum-based deposition techniques

Vacuum deposition is used to deposit CZTS compound on a substrate under vacuum, such as by sputtering, evaporation/co-evaporation, and pulse laser deposition methods. The benefits of these methods include direct control over the chemical composition of the sample, high levels of reproducibility, the ability to make high-quality thin-film devices, and simple, direct manipulation of the chemical composition of the sample.

3.4.1.1 Vacuum evaporation

Vacuum evaporation is a simple process that produces better-quality CZTS films. The raw film material is placed in a vacuum chamber and heated to a high temperature to cause the atoms or molecules to escape from the surface before forming a vapour stream that enters the surface of the plated substrate, where it condenses to form a solid film due to the substrate's low temperature. However, the vacuum deposition preparation process wastes film materials and is relatively expensive.

A device efficiency of 9.15% [89] and 11.6% [90] was achieved using vacuum co-evaporation and thermal co-evaporation techniques, respectively.

3.4.1.2 Magnetron sputtering

In magnetron sputtering, electrons collide with Ar atoms in an electric field, ionizing numerous argon ions and electrons which are then ejected to the substrate. The Ar ions are accelerated in an electric field, bombarding the target with many target atoms, and the neutral target atoms (or molecules) are deposited on the substrate to form a film. There are many advantages of magnetron sputtering, such as the possibility of making high-density thin films with precisely controlled element stoichiometry and thickness, low production cost, fast deposition, better adhesion of the film, and reduced contamination of the substrate [91]. A conversion efficiency of 9.26% has been achieved by a CZTS thin-film solar cell fabricated using this method [91]. However, the balanced magnetron sputtering process has a few disadvantages. Because of the effect of the electric field, the effective coating area is smaller. The deposition rates of some materials are low, making it hard to coat the substrate with a uniform film. In reactive sputtering, the gas composition must be carefully controlled.

3.4.1.3 Electron beam evaporation

In electron beam evaporation, an electric field is used to accelerate electrons so that they can bombard the evaporation material at the anode, causing the material to vaporize and produce an evaporation coating.

3.4.1.4 Spray pyrolysis

The spray pyrolysis process involves heating the substrate surface to around 600 °C and then spraying one or more metal salt solutions onto the substrate surface. The

high temperature causes pyrolysis of the spray coating, which forms a coat on the substrate surface.

3.4.1.5 Pulsed laser deposition

This method is straightforward, and it deposits films with the desired stoichiometric composition and high quality. The pulsed laser deposition technique is a physical vacuum deposition process that involves focusing a high-power pulsed laser on the surface of interest, followed by the generation of high-pressure, high-temperature plasma, which then spreads out to deposit a thin film on a substrate. Highest research device efficiency of CZTS using this technique ($\eta = 5.2\%$). However, this technique requires high laser energy, so some macroscopic and microscopic target elements are lost during the process. Moreover, single-step production of uniform film composition is difficult.

3.4.2 Non-vacuum-based deposition techniques

Non-vacuum techniques don't require a vacuum at any stage. It is less expensive and easier for thin-film deposition. Non-vacuum methods require the production of a precursor, which is then applied to a substrate by a variety of methods. These techniques include spin-coating of precursor solutions, nanoparticle inks, spray pyrolysis, solgel [92], the SILAR method, and electrodeposition. Deposition of thin films using non-vacuum approaches is discussed more below.

3.4.2.1 Sol–gel deposition

A spin coating process based on sol-gel is very straightforward and inexpensive for the fabrication of different semiconductor thin films. The preparation of thin films involves two steps: First, prepare a sol-gel precursor solution, and then spin coat the solution onto a substrate. It is easy to obtain homogeneous and multicomponent chalcogenide films and quantitative doping. By using this technique,

a conversion efficiency of 10.1% was achieved [61]. But there are some issues as well: certain organic raw materials are harmful and expensive, and it's difficult to manage how porous the material is.

3.4.2.2 Successive ionic layer adsorption and reaction

Films are deposited by cycles of adsorption and reaction in this process, and this can occur throughout the contact area between the substrate and the liquids (precursor solutions). It requires immersing the substrate alternately in cationic and anionic precursor solutions and washing it in highly purified deionized water after each immersion. The process is continued until the desired thickness of film is obtained. It is not influenced by external influences such as an electric or magnetic field, and vapor phase transfer from the source to the target is unaffected. Furthermore, the SILAR process is exceptionally eco-friendly because it utilizes only non-toxic chemicals and solvents and does not require expensive equipment or vacuum during the deposition [93].

3.4.2.3 Solvothermal

Solvothermal is a low-cost, eco-friendly alternative process that uses a solvent-based precursor solution to produce the desired material. Solvothermal synthesis prepares metals, semiconductors, ceramics, and polymers. This approach is suitable for the large-scale production of high-quality crystals while preserving good composition and morphological control. The main benefits of solvothermal synthesis include simplicity, high purity, low cost, and environmental friendliness, but also high crystallinity and energy savings. The procedure uses a solvent under moderate to high pressure (1 atm to 10,000 atm) and temperature (100 °C to 1000 °C) to enable precursor contact. Using solvothermal fabrication of CZTS thin film-based nanoparticles, photovoltaic devices demonstrated 3.56% efficiency [94].

3.4.2.4 Electro-deposition method

Electro-deposition is one of the low-cost, eco-friendly methods for coating a thin film over a large area. There are two types of deposition: electro-deposition, in which different layers of metal salts are deposited and annealed to get the final film, or constituent metal precursors are sequentially electro-deposited and then annealed in sulphur atmosphere, and single-step electro-deposition, in which all the constituents come from the same electrolyte. There are so many advantages of the electro-deposition method, such as the low temperature required for the deposition process, strong interface bonding in between the coating and substrate layers, no residual thermal stress, structure and porosity, chemical composition, and coating thickness that can be precisely controlled.

3.4.2.5 Nanoparticle inks

Guo et al. [95] initially reported the hot-injection method used to synthesize the nanocrystals necessary for making the inks. The nanoparticle inks can be deposited by several techniques, such as being dip-coated, doctor bladed, dropcasted, or spin-coated into thin films. It is found that efficiency is influenced by several parameters, such as composition, reaction temperature, and post-annealing conditions of CZTS nanocrystals [69, 96]. The nanocrystals-based approach was used to create a $Cu_2ZnSn(S,Se)_4$ thin-film solar cell with a 7.2% efficiency [95]. 10 % efficiency has been reported for CZTS nanocrystal thin film solar cells achieved by hydrazine-based solution processing. In another study, by selenizing nanocrystals with Ge/(Sn+Ge) = 0.25, device efficiencies of 8.3% were obtained. Ford et al. achieved 6.8% efficiency by selenizing nanocrystals, compared to a previously reported device with 7.2% efficiency fabricated without any germanium [97]. Exciting results demonstrate the potential of CZTS for high-efficiency thin-film solar cells through techniques such as drop casting, dip coating, and, spin coating [57].

3.5 Construction of the CZTS solar cell

CZTS-based materials are $p-$type semiconductors with a hole density of around 10^{16} cm^{-3}, which is characteristic of CIGS in high efficiency CIGS solar cells. These similarities allow the device architecture that is optimized for CIGS to work just as well for CZTS-based materials. A solar cell consists of a front contact, transparent conducting oxide (TCO), a window layer, a buffer layer, an absorber, and the most common device configuration is SLG/Mo/CZTS/CdS/Al: ZnO/Al/Ni for a CZTS thin film based solar cell as shown in Figure 3.4.

3.5.1 Thickness of the layers in the solar cell

In the second generation of solar cells, the thickness of the layer is another important characteristic that greatly impacts both cost and open circuit voltage. Absorber layers with a thickness of 100 nm are said to achieve a good compromise between series resistance R_s and the absorption coefficient. Interfacial layers are ideally between 5 and 20 nm thick, and the optimal window layer thickness to be 60 nm.

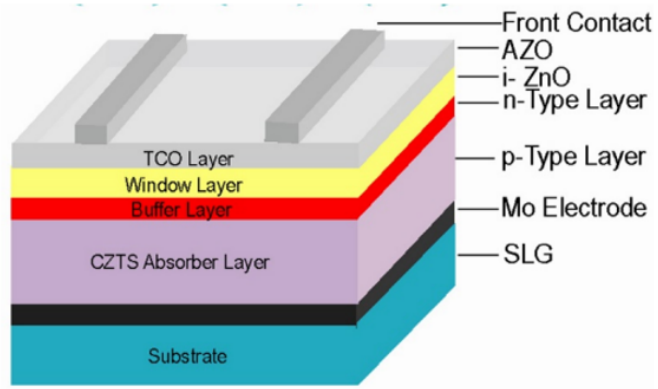

Figure 3.4: Schematic diagram of CZTS thin film based solar cell device [98].

3.5.2 Rear contact

The construction of CZTS solar cells has made use of soda lima glass (SLG) as the substrate covered by a metallic layer with a thickness of approximately 1 μm to provide electrical back contact. The spontaneous diffusion of sodium (Na) into the absorber layer is the main reason for using SLG-based substrates. Grain growth is enhanced due to the diffusion of sodium (Na) impurities into the CZTS nanocrystals. Na can passivate grain boundaries, which reduces non-radiative recombination processes. SLG coated with metals such as W, Mo, ITO, FTO, Cr, V, Ti, Mn, Au, Ni, Ag, Pt, Nb, and others are employed as electrodes to capture charge carriers [99]. Mo has high conductivity and stability in harsh conditions. Due to its many desirable properties, such as its excellent adhesion, ohmic contact, formation of the diffusion barrier layer $Mo(S,Se)_2$, and durability during the high temperature annealing process, the Mo layer is the back contact of choice for CIGS solar cells.Furthermore, the Mo layer allows sodium to migrate from the glass substrate to the absorber[13]. It is also used for the back contact in CZTS solar cells. The optimum surface substrate for a back contact in CZTS in photovoltaic applications was discovered to be molybdenum-coated glass. Many studies show that the substrate type has a significant impact on the CZTS characteristics [100]. Moreover, crystallinity, excellent morphology, and an energy bandgap of roughly 1.6 eV make CZTS films produced on a Mo substrate preferable for CZTS-based solar cells.

3.5.3 Absorber layer

For photovoltaic applications, there are different factors that should be taken into consideration when growing the absorber layer, such as the presence of secondary phases, contamination, impurities, and other imperfections, like grain boundaries, defects, and inhomogeneities, that are frequently reported to be present in a film. The absorber's band gap should be in the photon energy range so that it can absorb most of the incident sunlight. As an absorber layer, CZTS, a $p-$type semiconductor

is used. A layer of CZTS as a light absorber layer with a thickness of 1-2 μm is in contact with $n-$type CdS with a thickness in the range of 50–100 nm to form a p–n junction.

3.5.4 Buffer layer

3.5.4.1 CdS buffer layer

Despite Cd's toxicity, it has been discovered that the use of Cd-containing chalcogenides lowers Cd emissions to the environment because they are stable and water-insoluble unless exposed to acidic environments [101]. Typically, CdS is positioned between the window and the absorber layer. The buffer layer is frequently deposited on top of the absorber layer using chemical bath deposition [102]. The chemical bath deposition (CBD) technique has given the best solar cell performance to date. CdS is a wide-bandgap $n-$type semiconductor. This allows the most sunlight to reach the absorber layer. This is usually deposited as an $n-$type cadmium sulphide (CdS) layer by chemical bath deposition in a thickness range of 50–100 nm to form the p–n junction and is called the buffer layer. Buffer layer thickness plays an important role in the efficiency of solar cells. An increase in the thickness of the buffer layer can lead to the recombination of the generated electron hole pairs and, as a result, a decrease in the efficiency of the solar cells. CdS has good optical transmittance, a wide bandgap, a high absorption coefficient, low resistivity, easy ohmic contact, and good electrical properties. CdS is a II-VI semiconductor with an energy band gap of 2.45 eV. Due to its optoelectronic properties, CdS thin film has long attracted the attention of researchers, and it is commonly used as a buffer layer in solar cells. Moreover, this material gives the absorber layer thermal and chemical stability and leads to an improvement in the solar cell's bulk recombination [103]. However, the "cliff"-like conduction band offset at the CZTS/CdS interface is a limiting factor for the V_{OC} of CZTS solar cells [104]. At the CZTS/CdS interface, undesirable cliff-like band alignment is frequently raised,

causing an energy barrier to form, and causing recombination. Therefore, several initiatives have been made to reduce the cliff-like alignment or modify it into a more favourable spike-like alignment. Band alignment can be improved with the use of an interlayer applied to the interfaces between an absorber and a buffer. Specific materials such as SnO_x, In_2S_3, Al_2O_3, and ZnS as interlayers at the absorber/buffer interface. The absorber/buffer interface qualities will be enhanced by the addition of this interlayer. In a previous study, the V_{OC} of the CZTS/CdS solar cell increased because of the deposition of a SnO_x inter-layer. The tin oxide layer had no impact on the FF and J_{SC} values; hence, the increase in V_{OC} directly increased the PCE of the CZTS/CdS solar cell [105]. In other studies, the V_{OC} is improved by a TiO_2 interlayer, which achieves this by decreasing the interface recombination centre [106]. However, FF, J_{sc}, and efficiency were reduced.

3.5.4.2 Alternative buffer layer

Even though high-performance kesterite devices have been made with CdS as the buffer layer, researchers are looking into the use of Cd-free buffer layers to improve device performance and deal with concerns about toxicity. Thin film Zn(O,S) is a promising candidate to replace CdS thin film as a buffer layer for CZTS thin film absorber material. The material's features low interface recombination, high resistivity, transparency to incident light, good conduction band alignment with the absorber material, and reliable device stability make it a promising alternative for CdS as a buffer layer [107]. Martin et al. (2022) studied $Zn_{1-x}Sn_xO_y$ (zinc tin oxide, ZTO) deposition by atomic layer deposition, which produced improved open circuit voltage values and a high-quality interface in terms of band alignment and interface creation [108]. Bahfir et al. (2011) found that a CZTS-based solar cell was optimized by replacing the CdS buffer and ZnO window layers with a single layer of ZnMgO; the resulting cell had a conversion efficiency of 11.5 %, $V_{oc} = 0.78$ V, $J_{sc} = 22.3$ mA cm^{-2}, and FF = 66.1% [109].

3.5.5 Window and TCO layers

An intrinsic ZnO layer with a thickness of about 50–90 nm is usually sputtered on top of the CdS as a window layer. This is followed by a layer of Al-doped ZnO or indium tin oxide, which is a transparent conducting oxide. The transparent conducting oxide layer allows electrons to flow in the horizontal plane towards the front contact and prevents surface recombination. And finally, an Al/Ni layer is deposited as a front electrical contact to reduce series resistance and increase the current collection [110, 111, 112].

3.6 Annealing / sulphurisation

For photovoltaic applications, it's best for the absorber film to have large grains that facilitate the transport of photo-generated carriers while reducing the amount of recombination at the grain boundaries. Thus, the CZTS nanoparticle thin films are subjected to thermal annealing in the presence of sulphur (sulphurisation) [113], to promote grain growth. Annealing is the process of heating a substance to a specific temperature, usually in a controlled atmosphere, and then gradually cooling it down to room temperature, in order to enhance the structural qualities and elemental composition. Several studies suggest that the efficiency of a solar cell is enhanced by the sulphurisation of CZTS thin films, which increases the absorption coefficient of CZTS. The band gap of a CZTS absorber is increased via sulphurisation, leading to a higher open-circuit voltage. Studies showed that annealing the films in a sulphur environment prevented Zn-loss in the samples even at the higher annealing temperatures of 550 and 575 °C and also reduced the production of secondary phases such as $Cu_{2-x}S$ and Cu_2SnS_3. Different investigations explored the effect of annealing thin films under different atmospheres, such as vacuum, air, N_2 [79, 114, 115], and N_2+ H_2S environments [77, 92, 116]. The formation of different binary and ternary secondary phases during the sulphurisation process, such as Cu_2SnS_3, $Cu_{2-x}S$, SnS_2, and ZnS, with increasing temperature throughout the

annealing process, grain boundaries gradually merge, and grain size increases. As a result, the annealing process was critical to grain growth. Annealing films in an H_2S atmosphere at high temperatures between 450 and 550 °C results in very little binary or ternary sulphide and an enhancement in device performance. However, Zhang et al. (2019) found when the annealing temperature was raised above 600 °C, the CZTS crystal began to decompose at the grain boundary, causing the growth of secondary phases and excessively large grains, which caused surface nonuniformity. When the annealing temperature reached 625 °C, secondary phases such as ZnS and SnS_x were formed and pinholes that stretched through the film began to appear [60]. Shi. et al. (2020) found that air-annealing a Cu_2ZnSnS_4 precursor thin film effected crystal growth of a $Cu_2ZnSn(S,Se)_4$ absorber layer [117]. It is reported that in order to prepare a Cu_2ZnSnS_4precursor thin film for selenisation, a simple air-annealing pre-treatment is performed on the film first. This pre-treatment can result in sodium diffusion into the CZTS precursor thin film as well as surface oxidation of the CZTS thin film. The Na diffusion and surface oxidation of the CZTS precursor thin film can significantly enhance the crystal growth of the CZTSSe thin film, causing the small-particle bottom layer to be fully removed and a large-grain CZTSSe thin film to form. As a result, conversion efficiency of CZTS solar cell improved.

3.7 Grain growth

Grain growth means that the nanocrystals become larger in size and ideally form micron-sized grains . Chernomordik et al.[118] investigated the impact of varying temperature, time, and sulphur pressure during the annealing of CZTS nanocrystal films on their microstructure. the material incorporated into the abnormal grains appears to diffuse along the grain boundaries and nanocrystal surfaces from the nanocrystal floor layer on top of which they grow. Vapour transport was mentioned by Chernomordik et al. as another possible explanation for the migration of some

of the elemental species.

3.8 Challenge toward highly efficient CZTS solar cells

Despite all the advantages of CZTS absorbers, improving the efficiency of CZTS-based thin film solar cells remains a major challenge. CZTS solar cells have the advantage of having cheap manufacturing costs, being non-toxic, and having a high constituent element abundance. However, the present highest efficiency achieved by CZTS is 12.6%, which is still significantly less than the SQ limit because of various limiting factors, such as the formation of secondary phases and defects due to large grain boundaries at the CZTS absorber interface with either the back-contact or buffer layer. According to the literature, one of the key causes of low device efficiency is a higher deficit in open circuit voltage (V_{oc}). The reduction in V_{oc} overall reduces device performance by lowering short circuit density (J_{sc}) and fill factor (FF) [119, 120, 121]. The presence of an interface, stable secondary phases, bulk recombination between the absorber and conducting surface, non-uniform morphology of the absorber surface, and the presence of defects such as antistites, interstitials, and vacancies in the absorber layer all contribute to a decrease in V_{oc} [120, 122, 123]. High efficiencies are characterized by an off-stoichiometric Cu-poor and Zn-rich composition [122], and careful synthesis conditions are essential to avoid secondary phases and defects [120]. Because the chemical potential region for CZTS is narrow, the synthesis of pure-phase CZTS is sensitive to synthesis conditions. The narrow stable region is mainly restricted by the formation of secondary phases such as ZnS and Cu_2SnS_3, which form spontaneously during the synthesis when Zn is either rich or insufficient. Whereas SnS, CuS, and Cu_2S, with their short bandgaps and metallic properties, may cause shunting through the cell or unfavourable offsets, leading to recombination centres or electron blocking layers. ZnS, SnS_2, and Sn_2S_3 all have $n-$type conductivity, which means they might form a second diode in the cell and reduce the rectifying effects of the first

$p-n$ junction.

3.8.1 Secondary phases

Phase homogeneity and the presence of secondary phases limit the power conversion efficiency of CZTS solar cells. The formation of secondary phases during the growth of CZTS is one of the significant challenges as it affects the solar cell performance. Any nonstoichiometric regions in a kesterite absorber allows undesirable binary and ternary impurity phases to appear. When compared to CZTS, there are two types of secondary phases: those with a higher and lower bandgap energy, respectively. Secondary phases with a greater bandgap than the absorber can narrow the charge carrier transport conduction pathway and increase R_s, but reduce FF [60] [124]. ZnS and SnS_2 with their large bandgaps and insulating properties would prevent carrier extraction. Meanwhile, secondary phases with a lower bandgap than the absorber operate as trap states and recombination centres that reduce V_{oc} [82, 83] [124], whereas SnS, CuS, and Cu_2S, with their short bandgaps and metallic properties, may cause shunting through the cell or unfavourable offsets, leading to recombination centres or electron blocking layers and reducing the open circuit voltage for the solar cells. The Cu-poor and Zn-rich composition reduces the formation energy of the Cu vacancy V_{Cu} and helps enrich the $p-$type features. However, the Zn-rich results in the ZnS impurity, which leads to the shunt channel present in CZTS [120]. ZnS has a higher band gap than CZTS in the range 3.54–3.68 eV. ZnS can generate electron-hole pairs and current collection by reducing the active area [100], especially under Zn-rich growth conditions, which have been used in the most of experimental studies. Secondary zinc sulphide (ZnS) phases typically form in Sn-deficient but Zn-rich areas. ZnS would prevent current conduction in the absorber layer [113, 125]. SnS_2 can form secondary diodes inside the CZTS absorber and cause high photocarrier recombination. Secondary phase copper sulphide ($Cu_{2-x}S$) can occur in Cu-rich locations, which is a severe concern since it increases recombination and the shunt current cannot be used to

drive an external load [125]. Since the energy gap of the ($Cu_{2-x}S$) phase is lower than that of the CZTS phase (1-1.2 eV). The energy bandgap of the CZTS absorption layer might be filled with the electronic states which act as carrier trapping and non-radiative recombination centres, reducing the open-circuit voltage of the solar cell [91, 100]. CZTS solar cells suffer from a severe loss of fill factor, which is very likely attributed to the shunting behaviour. It is reported that the shunting behaviour in CZTS solar cells is primarily related to the Cu_xS phase, which might show metallic properties, and Cu_2SnS_3, whose bandgap is much lower than that of CZTS [56]. The presence of secondary phases affects the bandgaps of these films. A previous study discovered that secondary phases such as SnS_2, ZnS, and CuS cause bandgap shifts ranging from 1.41 to 1.68 eV. These phases cause changes in the optical absorption edge, which affects cell efficiency [113]. Different techniques were used to remove these secondary phases. As an example the secondary phases associated with copper and tin such as CuS, Cu_2S, SnS, SnS_2, and Cu_2SnS_3, can be eliminated using potassium cyanide (KCN) [72, 91, 125] and H_2O_2 etching, or HCl etching [72] to remove the oxide phases and ZnS phase from the absorber surface [126]. However, etching CZTS thin films would lead to the creation of voids on the thin-film surface, which would lower the quality of the CZTS film by affecting the stoichiometric homogeneity of the composition for the CZTS thin-film phase [91].

3.8.2 Sodium impurities

Na can passivate the dangling bonds in CZTS grain boundaries, improving photovoltaic performance. As a result, Na incorporation may be an effective method for passivating defects in CZTS films and yielding better single-phase CZTS [127]. Researchers found that soda lime glass (SLG) was the optimal substrate for depositing CIGS solar cells [128]. This was related to Na diffusing from the glass, through the Mo back contact, and into the absorber. Greatest efficiency Na incorporation is achieved in CIGS and CZTS solar cells through deposition on the SLG or the deposition of a thin Na-containing layer, often between the back contact and the

absorber. In fact, CIGS solar cells with relatively small grains can achieve very high efficiencies. When Na amounts are increased in the CZTS layer, the CZTS grain size increases significantly, and Zn segregation increases both in the heterojunction and in the back contact. Ehira.et al. (2017) studied the impact of Na-addition on CZTS solar cells. CZTS precursor and sodium fluoride (NaF) were sequentially deposited on Mo, then the film was sulfphurised with hydrogen sulphide. The sodium diffused from both sides of the CZTS surface and the substrate. As a result, an improvement in PV characteristics was due to the increase in carrier density due to the Na-addition effect on CZTS [129]. Other investigations into CZTS films grown on SLG using the ultrasonic spray pyrolysis process. SLG substrates were used to grow films. It was discovered that sodium diffuses into them. Sodium improved the grain size and texture of the CZTS films. The influence of sodium diffusion was also found to significantly increase the number of holes. The presence of sodium has a significant effect on the electrical properties of the films. The presence of sodium does help to improve the characteristics of CZTS films. These films are ideal for the fabrication of thin-film solar cells [130].

3.8.3 Defects in CZTS

Intrinsic defects play a significant role in influencing the electrical characteristics of the kesterite absorber Cu, Zn, Sn, or S vacancies (V_{Cu}, V_{Zn}, V_{Sn}, V_S); antistites AB with element A replacing element B (Cu_{Zn} , Zn_{Cu}, Zn_{Sn}, Sn_{Zn} etc.), and interstitials (Cu_i, Zn_i, Sn_i) are examples of likely intrinsic defects. The $p-$type conductivity is attributed to a large population of shallow acceptor-like defects such as CuZn antistites and Cu vacancies (V_{Cu}), the density of which depends on the Cu/(Zn+Sn) and Zn/Sn composition ratios.

3.8.3.1 Vacancy

The electronic characteristics of the kesterite absorber are heavily influenced by vacancy defects. Several investigations have claimed that the kesterite absorber is $p-$type due to Cu vacancy. It was reported that the formation energy of the copper vacancy V_{Cu} is 0.57 eV, and the acceptor state energy level is 0.02 eV above the valance band, as shown in Figure 3.5. As a result, copper vacancy can occur with the kesterite absorber. Many investigations show that Cu-poor and Zn-rich conditions are used to improve the efficiency of solar cells which has the consequence of increasing the copper vacancy formation maximum. However, some vacancy defects, such as sulphur vacancies, behave as traps, trapping charges and thereby reducing the highest possible efficiency of CZTS solar cells. Other acceptor level defects such as Zn vacancy V_{Zn} and Sn vacancy V_{Sn}, can be detected in CZTS with high energy formation. In these cases, due to their different formation energies close to the mid-gap level, as well as low formation energy, multi-acceptor states for each elementary vacancy behave as recombination centres in CZTS, having a negative influence on solar performance.

3.8.3.2 Interstitial

The energy levels due to interstitial defects are either within the band gap or in an unfavourable position. As an example, copper interstitial Cu_i could produce a shallow state near the conduction level, whereas zinc interstitial Zn_i produces two mid gap states. Interstitial defects have no beneficial effects on the performance of the kesterite solar cell because they do not help to improve the carrier concentration.

3.8.3.3 Antistite defects

In the kesterite absorber, acceptor levels might result from antisite defects. Due to the comparable chemical structures of Zn and Cu disorders, antisite defects are quite common. Being isoelectronic, these two atoms are easily able to switch

places, resulting in the Cu_{Zn} acceptor and Zn_{Cu} donor antisite defects. The $p-$type kesterite absorber is the result of these defects. However, a high concentration of these antisites may have a negative impact on device performance because it promotes trap-assisted recombination. As a result, it was discovered that non-stoichiometric samples with low Cu content and high Zn content are proposed to be suitable for high-performance devices. However, nonstoichiometric conditions allow the existence of secondary phases. Defects cause the local variation of the valence band maxima (VBM) and conduction band minima (CBM). The formation of mid-gap states, deep-level states, and donor levels causes the recombination of photogenerated carriers. Shallow donor or acceptor defects reduce the optical bandgap and reduce the light absorption of the CZTS absorber layer. Defects such as vacancies, antistites, and interstitials exist in CZTS. They cause the shallow acceptor, shallow donor level formation, and deep level states within the bandgap of the CZTS absorber layer. Figure 3.5 summarizes the calculated values of the intrinsic defect ionisation levels within the band gap of Cu_2ZnSnS_4. CZTS device performance is enhanced by copper vacancies, as these vacancies form a shallow acceptor level above the valence band maxima (VBM), which enhances the $p-$type material properties of CZTS. However, zinc and tin vacancies form both mid-gap and deep-level states within the bandgap of CZTS, while sulphur vacancies form only mid-gap states. Under copper-rich conditions copper and zinc interstitials are commonly detected in CZTS. They cause shallow donor levels and mid-gap states. Therefore, copper-poor, zinc-rich conditions provide better CZTS solar cell device performance. The high level of Cu_{Zn} may reduce open-circuit voltage, lowering solar performance as a result. Cu-poor and Zn-rich growth conditions should be used to enhance the formation of V_{Cu}, which has a shallow acceptor level of 0.02 eV higher than the VBM.

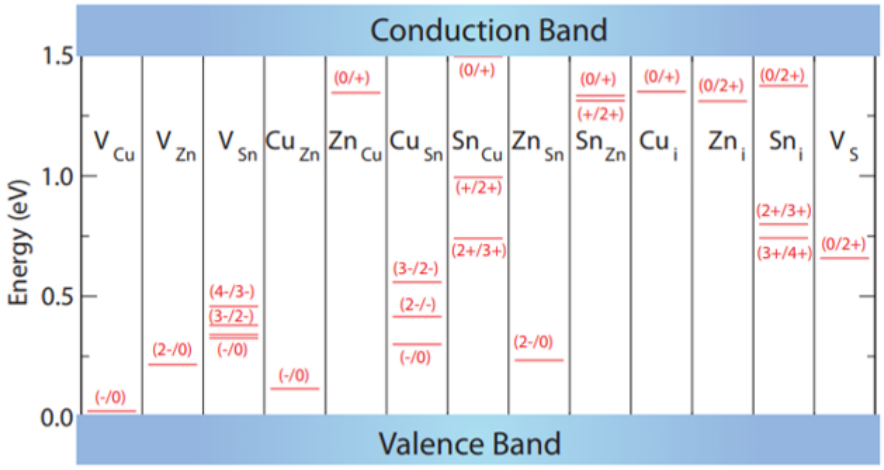

Figure 3.5: The defect ionisation levels in the band gaps of Cu_2ZnSnS_4 [65].

3.9 Fluctuations in band gap

The existence of various point defects, which disturb the local structure, causes band-gap fluctuation. It reduces open-circuit voltage and has a negative impact on photovoltaic device performance. According to a previous study [131] , disorder among the Cu and Zn atoms in the kesterite structure contributes significantly to the band gap variations that have been blamed for the large voltage deficit in CZTS solar cells. The disorder results in a high density of (CuZn+ZnCu) defect pairs. This would lead to losses in open circuit voltage and efficiency losses in a solar cell [132]. As a result, eliminating Cu-Zn disorder may be critical for future increases in the efficiency of CZTS-based solar cells.

3.9.1 Interface losses

3.9.1.1 Mo/CZTS interface

The back contact for the solar cell Mo/CZTS/CdS/ZnO/ITO construction is frequently reported to have issues with voids, low crystallinity, carbon contamination,

and the formation of a highly resistive MoS_2 interlayer, which tends to reduce the generated open-circuit voltage V_{oc}. Many investigations show that molybdenum (Mo) is the preferred back-contact material for CZTS solar cells due to its good adhesion and suitable ohmic contact. Mo films primarily meet the criteria of a back contact which has been widely used in solar cells due to their high processing temperature [59, 133]. However, the issues with the Mo/CZTS interface are that during annealing treatments, molybdenum sulphide (MoS_2), secondary phases, and voids form at the Mo/CZTS interface due to thermodynamic instability during the heat treatment process. Due to the high partial S pressure present throughout the heat treatment process, sulphur vapour diffuses toward the Mo back-contact, where it combines to generate MoS_2 and a secondary phase at the Mo/CZTS interface. MoS_2 is an indirect semiconductor with a low-bandgap [134, 135]. The performance of CZTS solar cells is impacted by thin and thick MoS_2 [133]. A thin layer of MoS_2 provides an excellent ohmic contact at the Mo/CZTS interface, improving solar cell performance. MoS_2 layers with a thickness of 350 nm are harmful to solar cell efficiency because they act as poor ohmic contacts, preventing the photogenerated hole from being transported to the Mo back-contact. Increases in heat treatment duration or temperature are typically required to enhance crystallinity, but they also lead to a thicker MoS_2 layer being formed [133]. As a result, the performance of solar cells was affected because electrical loss increased as a result of decreased hole carrier collection at the Mo back-contact, due to the presence of the potential barrier. According to other investigations, the MoS_2 layer contributes to significant R_s and electrical loss at the Mo/CZTS interface by acting as a Schottky barrier. This leads to inefficient collection of hole carriers at the Mo back-contact, decreasing the J_{sc}. Another issue associated with the instability of the Mo/CZTS interface during the heat treatment process is voids. This is undesirable because voids cause high R_s by disrupting the ohmic contact between Mo and CZTS, resulting in low FF, J_{sc}, and R_s values. The open-circuit voltage of the device can be reduced due to the formation of MoS_2. The formation of thick MoS_2 may result in electrical losses

due to poor ohmic contact between Mo and CZTS which prevents hole carriers from transporting to the Mo back-contact and increases the recombination centre. Due to less hole carrier collection at the Mo back-contact caused by this potential barrier, solar cell performance was ultimately decreased [134, 136]. Xiao et al. (2016) found that a larger MoS_2 layer lowers J_{sc} by acting as a built-in potential barrier to stop the photogenerated hole from moving from CZTS to Mo [136]. As a result, the performance of solar cells was affected because electrical loss increased because of decreased hole carrier collection at the Mo back-contact due to the presence of the potential barrier. According to other investigations [137], the MoS_2 layer contributes to significant R_s and electrical loss at the Mo/CZTS interface by acting as a Schottky barrier. This leads to inefficient collection of hole carriers at the Mo back-contact, decreasing the J_{sc}. Another issue associated with the instability of the Mo/CZTS interface during the heat treatment process is voids. This is undesirable because voids cause high R_s by disrupting the ohmic contact between Mo and CZTS, resulting in low FF, J_{sc}, and R_s values [136]. As indicated by Xia et al. (2015), the volatile Sn-related secondary phase diffused towards the CZTS surface during the heat treatment process, leaving behind voids that contributed to poor ohmic contact and a shunting pathway [134]. It has also been reported that the existence of a Zn-related secondary phase at the Mo/CZTS interface reduces FF and increases R_s because the Zn secondary phase accumulates at the Mo/CZTS interface and narrows the path of hole carriers back to the Mo back-contact. In addition, the Cu-related secondary phase introduces shunting routes that decrease the FF of the device due to its metallic nature and low resistivity. To address these concerns, various studies have been conducted to investigate the use of alternate back contacts or interlayers at the Mo/CZTS interface, such as metal and metal oxide, nitride, or metal sulphide interlayers. Mo and CZTS interfacial reactions were avoided by using the interlayer. As an interlayer at the Mo/CZTS interface, metals are advantageous due to their high conductivity and work function. Some intermediate layers improve the CZTS solar cell's back contact. TiN, Ag, Bi, C,

ZnO, Al_2O_3, and TiB_2 are intermediary layers between CZTS and Mo. It has been discovered that using metal interlayers such as Bi, Ti, and Al slows the growth of the MoS_2 layer, resulting in a reduction in R_s. The Bi layer improves the crystallinity of the synthesized Cu_2ZnSnS_4 film, as demonstrated by larger grain diameters and fewer grain boundaries [138]. To improve the device's performance, a Ti film is placed between Mo and CZTS as a layer and dopant. The Ti layer prevents the diffusion of sulphur into the Mo films, and thereby prevents the formation of MoS_2 [139]. The Al intermediate layer helped to reduce MoS_2, ZnS, and SnS_{2-x}, which improved FF and carrier transfer [140]. Voids and phase segregation at the rear contact region can be effectively minimized by adding an intermediate layer of metal oxide, such as an aluminium oxide (Al_2O_3) interlayer layer between Mo and CZTS, and limiting the interface reaction between CZTS and Mo [141]. It has been discovered that the presence of MoO_3 improves the sodium transport into CZTS and encourages the growth of bigger CZTS grains during the sulphurisation process [142]. Carbon, ceramics, and silicon have also been reported as interlayers at the Mo/CZTS interface. Both materials have significant and interesting advantages, particularly in reducing the formation of MoS_2 by preventing sulphur diffusion and enhancing the grain size of the CZTS absorber.

3.9.1.2 CZTS/CdS interface

The $p-n$ junction of the CdS and CZTS interfaces is an interesting topic of investigation because of charge carrier recombination and band offset. Figure 3.6 shows a spike and cliff recombination/band offset. The V_{oc} is raised because electron transport from CZTS to CdS is hindered by the spike barrier. In addition, the cliff barrier facilitates electron transport from CZTS to CdS, which raises the fill factor (FF), as well as the J_{sc} and V_{oc} [143]. Unwanted cliff-like band alignment is frequently raised at the CZTS/CdS interface, resulting in recombination due to the formation of an energy barrier, which has been shown to reduce surface contamination. The issues associated with the CZTS/CdS interface are mostly

caused by suboptimal band alignment which results in photogenerated carrier interface recombination. When the conduction band maximum (CBM) of CZTS is greater than that of CdS, trap state recombination occurs, but high barrier recombination occurs when the CBM of CZTS is lower than that of CdS. CZTS has a greater CBM than CdS, indicating a negative Conduction Band Offset (CBO) of the cliff-like alignment. It was found that a slightly positive CBO is preferable for band alignment because it creates a pathway for photogenerated electrons to travel through when the bias is forward. As the CBO increased from 0.0 to 0.2 eV, Sun et al. (2018) reported a longer carrier lifetime correlated with an increase in V_{oc} from 638 to 657 mV [144]. However, Hong et al. (2017) found that a reduction in CBO from -0.14 to -0.4 eV causes a decrease in V_{oc} from 623 to 561 mV, indicating an increase in trap state recombination that causes a significant electrical loss [145]. The efficient performance of a solar cell always requires low interfacial recombination. Several strategies have already been taken regarding the interfacial engineering, such as the addition of an alternate buffer layer [102], additional passivation layer, and thermal treatment of the junction. Previous research has shown that heat treatment at the interface of CZTS solar cells improves V_{oc} and FF significantly.

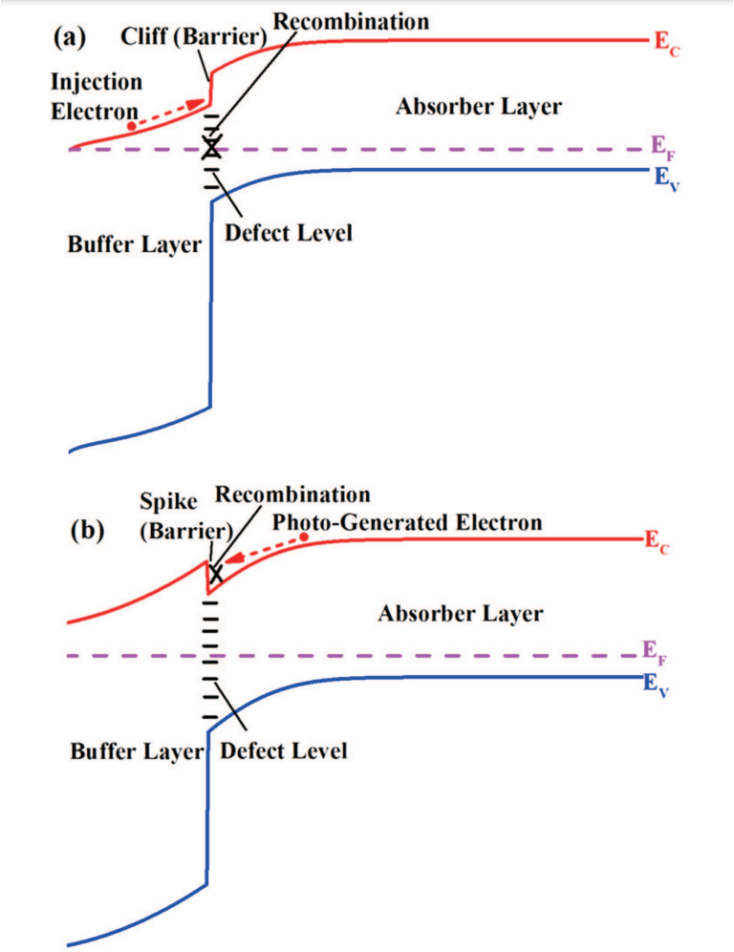

Figure 3.6: Simplified energy band diagram showing the two possible conduction band offsets at the $p-n$ junction, with (a) cliff type, and (b) spike type barriers [146].

3.10 Summary

With its kesterite structure and favourable direct band gap between 1.4 and 1.5 eV and high absorption coefficient, over 10^4 cm^{-1}, Cu_2ZnSnS_4 (CZTS) is a promising candidate for synthesis of low cost, high efficiency thin film solar cells. It is also composed of elements that are both abundant on Earth and nontoxic. The efficiency of the kesterite solar cell CZTS is discussed in detail in this chapter. If compositional difficulties like secondary phases, defects, interfacial recombination, and annealing temperatures are resolved, the CZTS may eventually replace the

CIGS as the standard for advanced solar technology.

Chapter 4

Cu_2ZnSnS_4 thin film fabrication and characterisation techniques

This chapter provides an overview of the CZTS nanocrystal synthesis process using the hot injection method and the deposition of the resultant CZTS ink to fabricate thin films. A description of the techniques used for the characterisation of CZTS thin films follows.

4.1 Thin films fabrication

4.1.1 CZTS nanocrystal-based approaches

CZTS nanocrystal ink-based approaches start with the controlled synthesis of nanocrystals and end with the deposition and post-treatment of films using the resulting inks.Solid particles are dispersed in a solvent to create an ink that can be deposited on a substrate. CIGS thin films have a comparable structure and characteristics to CZTS thin films, so the use of similar technologies for CZTS thin films has been extensively researched. Various studies on the hot injection method of synthesis of nanocrystals have been reported [147, 96]. It is an attractive method of synthesising $Cu_2ZnSn(S, Se)_4$ thin film absorber layers for photovoltaic applications. Hot injection is a simple method for producing various types of nanoparticles. This

method leads to the immediate nucleation and growth of nanocrystals. It provides control over composition and morphology. Guo et al. [148, 95] have revealed for the first time a simple synthesis for quaternary CZTS nanocrystals. They used the hot injection process, which involves injecting a cold precursor solution into a hot surfactant solution (oleylamine) while shielded by inert gas, to synthesize CZTS nanocrystals. Guo et al. (2010) found by using CZTS nanocrystal fabrication methods, the efficiency of CZTSSe solar cells reached 7.2% [95]. Qu et al. (2016) used the hot injection method and found that doping level, secondary phases, and crystal structure are affected by different parameters such as the reaction time, temperature, and cooling rate of the nanoparticle fabrication process, respectively which leads to a higher open circuit voltage and lower parasitic resistance, increasing device efficiency [96]. In this study, the CZTS nanoparticles have been synthesised using the hot injection method. After the synthesis of nanocrystals and fabrication of CZTS thin films, the films are annealed at high temperatures in a sulphur atmosphere to enhance grain growth and decrease surface defects and grain boundaries which leads to improvements in device parameters such as open circuit voltage, short circuit current, and fill factor.

4.1.2 Synthesis of Cu_2ZnSnS_4 CZTS nanoparticles

CZTS solar cells with the highest efficiencies can only be obtained using Cu-poor and Zn-rich composition regions. Shallow acceptors in CZTS are a result of Cu vacancies being formed under Cu-poor conditions. In contrast, Zn-rich conditions suppress the substitution of Cu at Zn sites, resulting in deep acceptors [40, 149, 150]. The CZTS thin film with the highest photocurrent response had a Cu/(Zn+Sn) ratio of 0.79 to 0.85 and a Zn/Sn ratio of 1.05 to 1.25 [149, 150, 151]. The nanocrystals are synthesised using a hot-injection method, which was described by Guo et al. [148, 95]. Slight changes have been made in the precursor ratios and the centrifuging procedure. The synthesis of nanoparticles began with the combination of metal salts dissolved in oleylamine: copper (II) acetylacetonate (Sigma Aldrich

99.99%), 1.332 mmol; zinc acetylacetonate (Sigma Alrich 99.995%), 0.915 mmol; and tin (IV) bis (acetylacetonate) dichloride (Sigma Aldrich 98%). These three precursor powders are mixed with 10 ml of oleylamine in a three-neck flask used as the reaction vessel. Because of its high boiling point and excellent coordinating nature (managing the growth), the synthesis procedure was carried out in oleylamine [149].

At the beginning of the procedure, the solutions of metal salts were mixed at room temperature. A magnetic stirrer bar was placed inside the flask for uniform mixing. The three-neck flask was attached to a Schlenk line which has two tubes. One tube is connected to a source of argon; to remove residual water and oxygen dissolved in the solvents. The other Schlenk tube is connected to a vacuum pump to eliminate air from the solution. A thermometer is inserted in the third neck to monitor the reaction temperature, as shown in Figure 4.1. The experiment started with the evacuation of the three-neck flask. The resulting solution was heated up to 140 °C and maintained at that temperature for 30 minutes with constant stirring. The vessel was then purged with argon gas three times for five minutes each, using a small disposable needle inserted into the bung to compensate for the pressure. All reaction conditions were kept inert to prevent formation of undesired oxides [149].. After that, the precursor solution was heated to 225 °C, followed by the injection of a solution of elemental sulphur after reaching this temperature. This 4 mmol of sulphur powder was mixed with 12 ml of oleylamine and stirred in an ultrasonic bath at 90 °C to ensure uniform dispersion. After the injection, the temperature was held at 225 °C for a reaction time for 30 minutes to allow the growth of the CZTS nanoparticles. Then, the mixture was left to cool down [148, 95, 152, 69, 153, 154].

4.1.3 CZTS ink fabrication

After the mixture cooled to room temperature, 5 ml of toluene and 40 ml of isopropanol (IPA) were added to the reaction mixture, and the nanoparticles were

collected using two tubes in a centrifuge, as shown in Figure 4.1. After centrifuging at 10,000 rpm for 10 minutes, the supernatant containing unreacted precursors and by-products was discarded [95]. The CZTS nanoparticles were then washed twice with toluene and IPA and centrifuged at 8000 rpm for 10 minutes to remove excess dissolved capping agents[149]. After that, the synthesized nanoparticles are dried overnight in a vacuum desiccator. To create a fine powder of nanocrystals, the accumulated particles are gently ground in a mortar and pestle. Then, CZTS nanoparticles were dispersed in 1-hexanethiol [$CH_3(CH_2)_5SH$; from ACROS Organics, 96 %] and placed in an ultrasonic bath for 45 min at 90 °C at a concentration of 200 mg/mL to create the CZTS ink which was then used to deposit nanoparticles on the substrate [155].

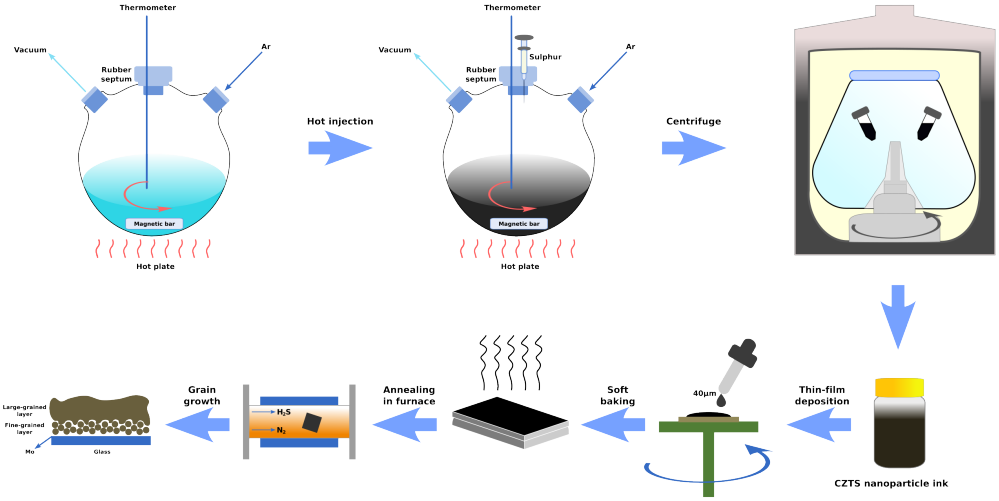

Figure 4.1: Schematic diagram of the setup for the synthesis, fabrication, and annealing of CZTS thin films.

4.1.4 Fabrication of Cu_2ZnSnS_4 thin films

4.1.4.1 Substrate preparation

The thin films were prepared from CZTS nanoparticle inks that were fabricated using the hot injection method described above. A 2.4 x 2.4 cm^2 soda lime glass

(SLG) substrate was cleaned sequentially in acetone, methanol, and deionized water in an ultrasonic bath (10 min each) and then dried with a nitrogen gas gun.

4.1.4.2 Deposition of rear contact (Mo)

In this work, a molybdenum (Mo) layer has been used as the back contacts for CZTS solar cells because of the advantages of Mo, such as good adhesion between CZTS and the glass substrate, stability, and low resistivity at high processing temperatures. RF and DC magnetron sputtering can be used to deposit the rear contact layer on the SLG substrate. Mo films with a thickness of around 800 nm were used as a back contact. The Mo films were deposited by RF magnetron sputtering with a target of 2-inch diameter on cleaned glass substrates held at room temperature. RF magnetron sputtering of molybdenum begins with the chamber being evacuated to a high vacuum of between 10^{-5}-10^{-6} torr to reduce contaminants and produce better quality films. Then a plasma is created in the chamber by applying a high voltage between the cathode connected to the target and the anode connected to the chamber. The Mo film was RF sputtered onto the glass substrate when a suitable pressure of 2.5×10^{-3} torr was reached. In this sputter system, a turbopump backed by a rotary pump was used to evacuate the chamber to an initial pressure in the range of 10^{-5}-10^{-6} torr. Deposition was carried out at various powers ranging from 40 to 50 W at an Ar pressure of 2.5×10^{-3} torr.

4.1.4.3 Deposition of Cu_2ZnSnS_4 thin films

The deposition of CZTS thin films on substrates is investigated using two methods: drop casting and spin coating. Drop casting was used to deposit films studied in Chapter 7 and spin coating for films studied in Chapters 5 and 6. Drop casting is a straightforward film forming method that is popular among research groups since it doesn't demand special tools. The solution containing the required substance is

dropped over a substrate, followed by the evaporation of the solvent. Less material waste is one of drop casting's benefits. However, producing a homogeneous coating and controlling its thickness is challenging. The thickness and characteristics of the films are affected by the volume and concentration of the dispersion. There are several factors, such as the drying process and rate of evaporation, that influence the film's structure. In the spin coating process, a solution is applied to a substrate, which is then spun at a specified rotational speed. The solution is sheared by the centrifugal force, which leads to an equal distribution of the thin film as it covers the surface. It enables the production of homogenous films with great uniformity in morphology. However, it is a wasteful technique because most of the solution is expelled during the spinning process. Furthermore, this might make coating with a low-concentration solution challenging. The deposition of CZTS nanocrystal ink using the spin-coating method involves the dropping of nanoparticle inks onto a substrate during its acceleration to a certain angular velocity. In this study, for the drop casting method, a pipette was used to apply one drop of 40 μl of concentrated ink to a square (2.4 cm $\times$ 2.4 cm) SLG substrate. For spin-coated films, the spin coater (WS-400 Lite Series Spin Processor from Laurell Technologies) was used for the deposition of the ink on the substrate, where the glass substrate is held on a rotating plate by vacuum. the spinning speed used was 2500 rpm for 15 sec. 40 μl of the concentrated ink was applied to a square (2.4 cm $\times$ 2.4 cm) SLG and molybdenum-coated SLG substrate during each spin cycle. Because of the hexanethiol boiling point at 150–154 °C, residual hexanethiol in the CZTS thin film could be easily removed after deposition by soft baking, which has been adopted from a previous study [156] using hot plates at temperatures of 150 and 300 °C for 30 sec . This entire coating process was repeated several times to achieve the desired CZTS film thickness of about 1 μm.

4.1.4.4 Deposition of CdS buffer layer

To test the film properties and optimize the buffer layer, a thin n-type CdS layer was deposited on the cleaned glass using the chemical bath deposition (CBD) technique. After the optimisation of the buffer layer, CdS was deposited onto CZTS for devices. Glass slides were first used as substrates to deposit CdS test layers. To deposit the cadmium sulphide CdS thin films, the glass slide was then placed in the prepared bath solution for CBD. A set of samples of CdS were deposited on cleaned glass substrates using the bath temperature of 75 °C at different deposition times (20, 30, 45, and 60 min). As shown in Figure 4.2, the reaction took place in a double-walled beaker with a water jacket to keep the reaction temperature constant at 75 °C.

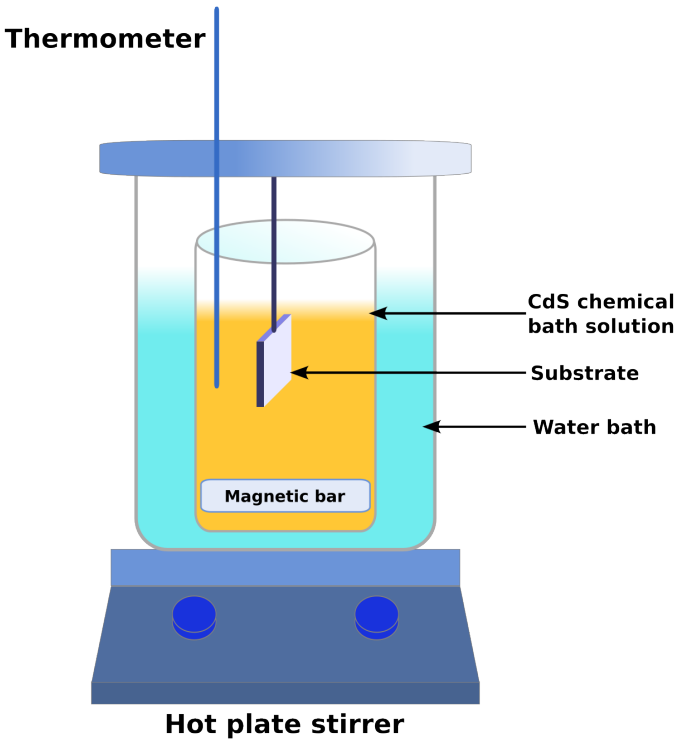

Figure 4.2: Schematic diagram of chemical bath deposition (CBD).

The substrates were immersed in a solution of 2.5 mg cadmium sulphate ($CdSO_4$),

ammonium hydroxide (15 ml), and thiourea ($CS(NH_2)_2$). The total solution volume was adjusted with water to 150 ml. Ammonium hydroxide was added to cadmium sulphate ($CdSO_4$), and the mixture was then stirred. Thiourea was added to the solution after soaking the glass substrates in it for 2 minutes, the stirring process was continued. After the CdS layer formed on the glass surface, the substrates were removed from the bath, rinsed with deionized water to remove the extra chemicals and solvents, and allowed to dry in air. Homogenous CdS thin film deposition was observed on the glass substrates. CdS thin films were subjected to characterisation studies.

4.1.5 Annealing of the CZTS thin film

Annealing is the process of heating a film to a specific temperature and then slowly cooling it to room temperature. Thermal annealing is a crucial stage in the manufacturing process that has a substantial impact on the material's morphology, improves the material's interface characteristics, and reduces the recombination centres at the *p*-n junction interface [155]. Annealing CZTS thin films in different atmospheres and its effect on their structural and optical properties was studied by many research groups. To improve the growth of CZTS films, the samples were annealed in a variety of atmospheres, including vacuum, nitrogen (N_2), sulphur (S), and vacuum followed by sulphurisation under H_2S + N_2 [77]. The results of the studies show that thermal treatments improve the crystalline quality of CZTS films. It is obvious from these results that vacuum annealing (alone or combined with other annealing processes) plays a crucial role in eliminating the secondary phases in CZTS thin films. Olgar et al. examined the impact of sulphurisation time and temperature on CZTS thin films and concluded that sulphurisation at 560 °C for 60 s is the most promising condition for CZTS growth [116]. Maeda et al. (2011) investigated how varying H_2S concentrations 3, 5, 10, and 20% affected the characteristics of CZTS during the sulfurization process. Increasing the H_2S concentrations affected the chemical compositions. The copper content decreases,

and the sulphur content increases when the H_2S concentrations are increased from 5% to 20%, and when the H_2S concentrations are decreased to 3%, the sulphur content increases [157]. In another study, the precursor elements should be kept at a higher sulphur vapour pressure to prevent the decomposition of quaternary compounds, to improve the single phase CZTS synthesis, and to reduce secondary phases [158]. In our work the thin films are annealed at high temperatures in an annealing atmosphere of hydrogen sulphide and nitrogen H_2S+N_2 at temperatures ranging from 375 to 575 °C. Annealing of the CZTS films is performed in a furnace quartz tube, as shown in Figure 4.3. First, insert the samples inside the centre of the furnace. A rotating vacuum pump was used to evacuate the furnace tube, which was then filled with N_2 gas. After closing the rotating vacuum pump, a mixture of H_2S and N_2 with a composition ratio of 20:80 was introduced and left to fill the tube while the pressure was monitored until it reached a required pressure of 0.1 atm, the H_2S supply is then closed. After that, set the temperature of the furnace to the desired temperature with a heating rate of 10 °C/min for one hour. Afterwards, the samples were allowed to cool naturally to room temperature, which took around 24 hours. Finally, the furnace tube was flushed with nitrogen . Overall annealing cycle of CZTS thin films in the furnace system is shown in Figure 4.4 at an annealing temperature of 500 °C.

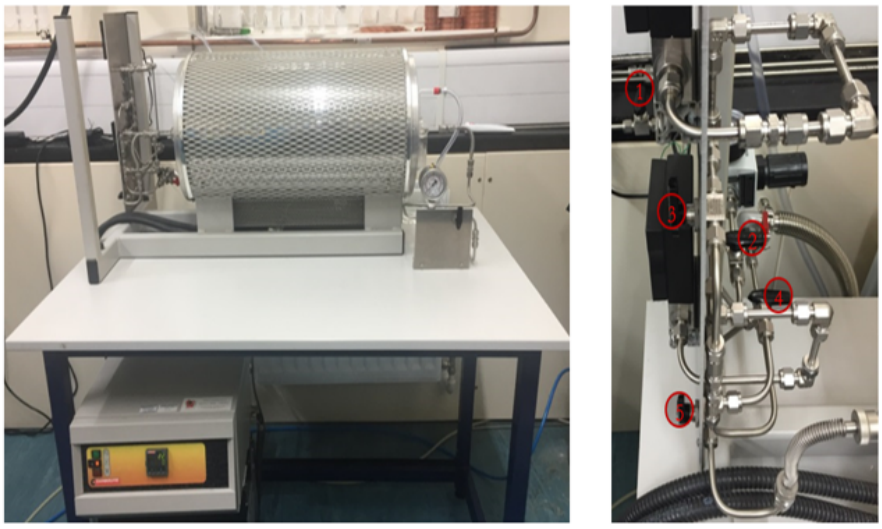

Figure 4.3: The furnace and gas supply sulphurisation annealing system to perform the annealing measurements required for this thesis a) front view; b) side view; and nitrogen valve (1), flush valve (2), the gas mix valve (3), vacuum valve (4), and the furnace valve (5).

4.2 Characterisation techniques

This section describes the characterisation techniques used for CZTS thin films deposited by drop casting and spin coating on different substrates. There are several characterisation techniques used in this research, including the X-ray diffraction (XRD) technique which gives the crystal structures of materials present in CZTS, including associated parameters such as lattice parameters, crystallite scattering domain size, and secondary phases. Raman spectroscopy can be used to identify materials using their vibrational, rotational, and other low-frequency modes. Raman measurements are used as a complementary measurement to detect the secondary phases in CZTS. Electron microscopy techniques such as scanning electron microscopy (SEM) and focused ion beam milling (FIB). SEM and FIB can give both morphological and compositional images of the CZTS surface on the micro- and nanoscale. FIB can be used for cross-section analysis. Finally, the optical properties of CZTS thin films were investigated using UV-Vis spectroscopy.

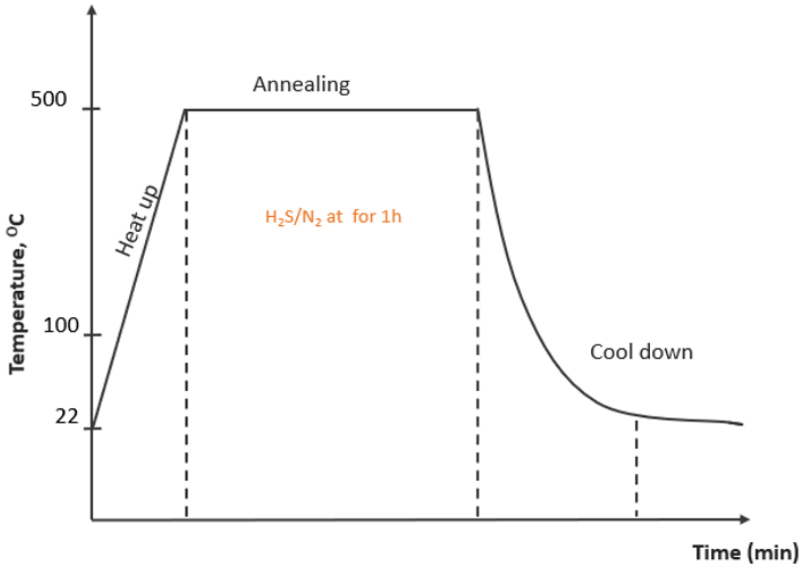

Figure 4.4: A schematic annealing temperature cycle of CZTS thin films in the furnace, not to scale.

4.2.1 Scanning electron microscopy

Scanning electron microscope (SEM) is one of the most useful tools for analysing micro-structure morphology and characterizing chemical composition. SEM is a high-resolution technique for studying the morphological and compositional properties of a sample surface at the micro- and nanoscale. When an electron beam strikes a sample, it scatters for hundreds of nanometers from atoms. The components of a standard SEM include an electron gun, sample stage, condenser, and objective lenses, scanning coils, a control system, and a pumping system. On the top of the microscope chamber sits the electron gun, as shown in Figure 4.5.

4.2.1.1 Sample coating

Prior to SEM analysis, all samples are coated with a conductive coating, such as gold (Au), with 30 nm thickness to increase the surface conductivity. For this purpose, a Chessington Sputter Coater (108 auto) and argon gas were used. The

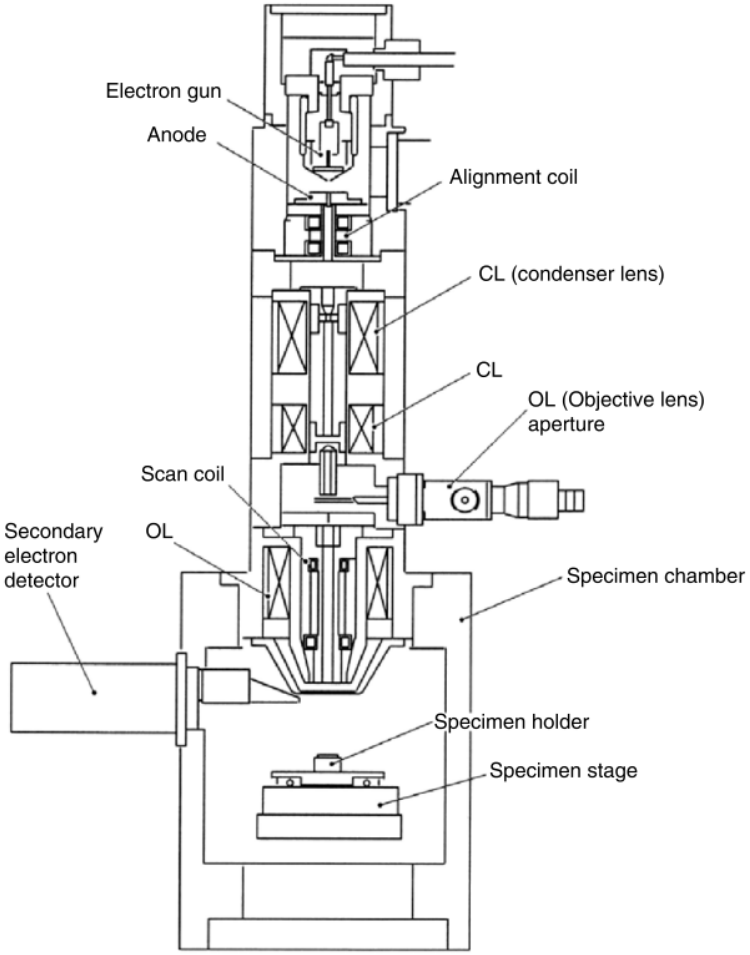

Figure 4.5: Schematic diagram of scanning electron microscope (SEM) [159].

prepared samples are attached to the sample holder with conductive adhesive to ground them electrically.

4.2.1.2 SEM imaging

Electrons are accelerated to an energy that ranges from 1 to 50 keV. The electrons continue to travel as they pass through the condenser and the objective lenses, which reduce the magnification of the electron beam, until they reach the sample. Scanning coils are used to divert the electron beam so that it may scan the specimen in the x and y directions. This finally leads to surface imaging by the various electron detectors. The acquisition of signals produced by the electron beam and

specimen interactions is required for image formation in the SEM. Figure 4.6 shows the different signals created by the electron beam-sample interaction in the scanning electron microscope, as well as the locations from which the signals may be detected. These interactions are classified into two types: elastic interactions and inelastic interactions. Elastic scattering is caused by the incident electron's deflection by the sample atomic nucleus or by outer shell electrons with a similar energy. The electron scattered during this type of interaction changes direction at a wide angle and loses very little energy during the collision. Backscattered electrons (BSE) are incident electrons that are elastically scattered at angles greater than 90 and produce a signal that is helpful for imaging the sample. When inelastic scattering takes place, a significant amount of energy is transferred from the primary beam electron to the sample atom through various interactions between the incoming electrons and the electrons and atoms of the specimen. Energy loss depends on whether the binding energy of the electron to the atom or specimen electrons is excited singly or collectively. Excitation of sample electrons during ionisation of sample atoms leads to the generation of secondary electrons (SE), at much lower energy which are used for imaging and analysing the sample [159]. When an electron beam contacts a sample, many other signals are generated in addition to those that are used to create an image. These additional signals include the emission of distinctive x-rays, Auger electrons, and cathodoluminescence. Depending on the signals from secondary electrons, backscattered electrons, or diffracted backscattered electrons, SEM is employed in various ways. Backscattered electrons reveal contrast in various phases based on detecting an atomic number in a multiphase specimen. Secondary electrons are utilized for image viewing and provide information about the morphology and topography of a specimen. A Hitachi SU-70 FEG was used to capture the SEM images shown in this study. A 12 kV acceleration voltage is typically used when obtaining them at working distance (15 mm), and the condenser and objective lenses are both set to the number 3, 2 respectively.

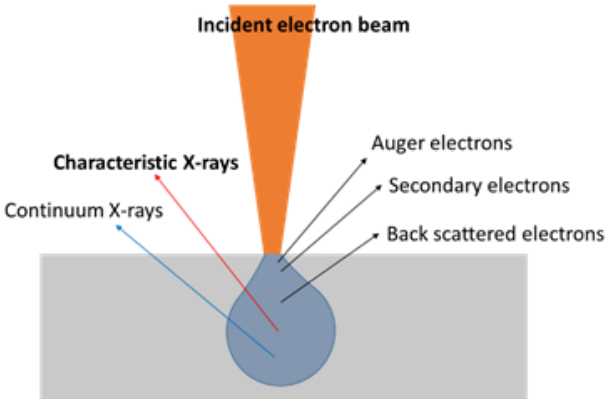

Figure 4.6: Signals emitted by incident electron beam-sample interactions.

4.2.1.3 Atomic composition

Energy-dispersive X-ray (EDX) is a technique used for chemical characterisation and elemental analysis. EDX is frequently performed with an electron microscope. When a beam of X-rays or electrons is used to excite core electrons in the sample, it emits X-rays which are detected by the EDX method. An inner K electron is knocked out of an excited atom. To relax the atom, an outer shell L (M) electron jumps in. During this transition, the extra energy may be released in the form of a characteristic X-ray, as shown in Figure 4.7. Each element emits characteristic X-rays at a distinct wavelength. Because the energies and wavelengths of various elements are distinct from one another, a chemical analysis may be performed simply by measuring them. The EDX software of today allows for the retrieval of point, line, and map chemical analyses. In this study, EDX analysis was performed with a Hitachi SU-70 FEG SEM in combination with the X-MaxN 50 Silicon Drift Detector and the analysis software Aztec 3.2 from Oxford Instruments. To characterize the CZTS thin film acceleration voltage of 12 keV, the condenser and objective lenses are set to 3, 2, and the working distance is set to 15 mm, respectively. A beam measurement with a cobalt (Co) standard is performed to ensure proper calibration. In this study, For composition determination, two or three areas distributed over the sample surface are averaged, where each of these areas is divided into nine subareas.

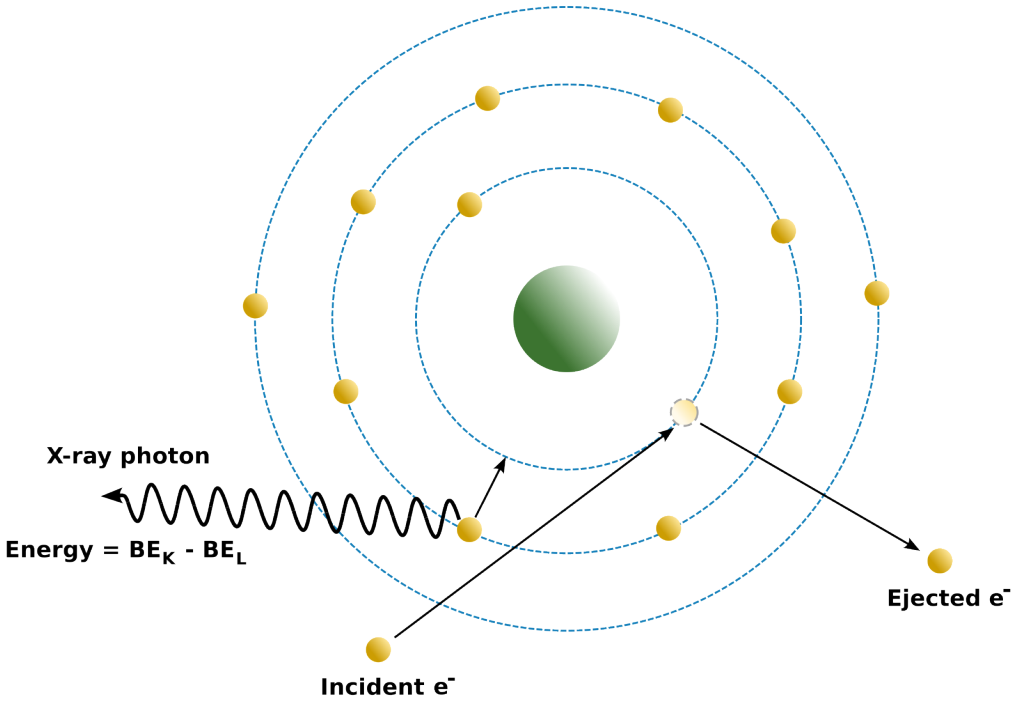

Figure 4.7: Schematic diagram of the characteristic X-ray generation.

4.2.2 Focused ion beam milling

Many scientific disciplines use focused ion beam (FIB) technologies for specific analysis, imaging, milling, and deposition. Dual-beam platforms which combine a FIB column and a high-resolution scanning electron microscope (HR-SEM) [160]. Figure 4.8 shows a schematic diagrams of the FEI Helios Nano Lab 600 Dual Beam system, where some of the cross-section images were performed.

In FIB , a relatively massive element's high-energy ionized atoms are focused onto the sample by a FIB column. The larger mass of the ions makes it simple for them to displace surface atoms from their positions and generate secondary electrons (SE) from the surface, which enables the ion beam to image the sample [160]. Most current commercial dual-beam platforms and FIB systems use gallium (Ga^+) as the ion source. Ion milling, which primarily depends on the beam current, and voltage utilized in the procedure, is essentially an atomic collision process that results in the removal of material from the ion-sample interaction volume.

Ion milling may be used to create different shapes in the material, such as lines, rectangles, or circles. In this work, the surface morphology and the cross-section of the heterojunction were examined on a FEI Helios Nano Lab 600 FIB microscope. A platinum layer was deposited on the sample's surface, and the sample stage was tilted at 52°. FEI Helios Nano Lab 600 focused ion beam (FIB) and scanning electron microscopy system are used for the imaging and cross-section imaging of CZTS thin film samples. The instrument can operate in both ion beam and electron beam regimes.

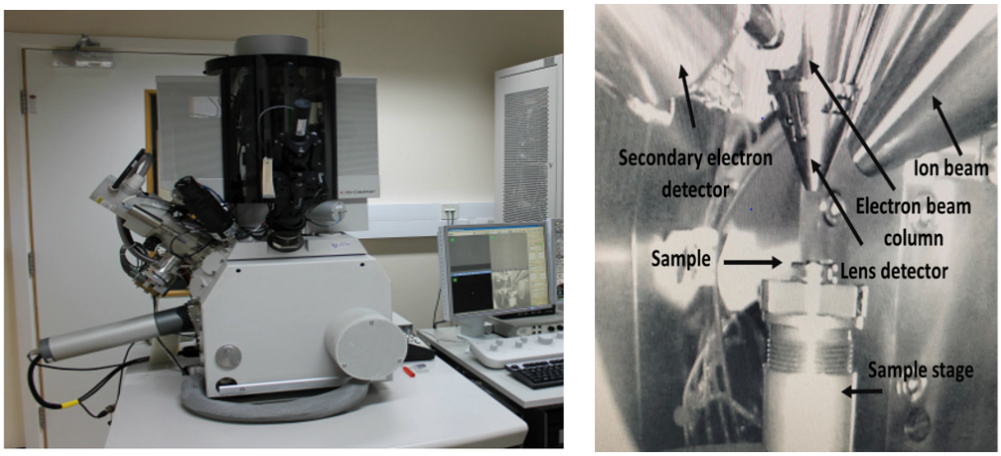

Figure 4.8: Schematic diagrams of the FEI Helios Nano Lab 600 Dual Beam system available in the laboratory where some of the work for this thesis was performed.

4.2.3 X-ray diffraction

4.2.3.1 Estimation of lattice parameters and grain size

XRD is a standard technique to investigate the crystal structures of samples and associated parameters. X-rays are electromagnetic waves with a shorter wavelength than visible light. X-ray diffraction techniques are based on wave interferences. Constructive interference happens when incident rays are "in phase," or when their phases differ by n (n is an integer). Completely destructive interference occurs when they are completely out of phase, or when their phase differences are $(n/2)\lambda$.

The interaction of two x-rays with repeating atomic lattice planes is shown in Figure 4.9.

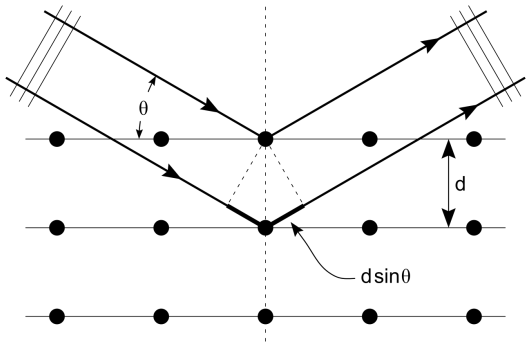

Figure 4.9: The interaction of two x-rays with repeating atomic lattice planes.

The distance between the planes is denoted by the symbol d, and the angle of incidence of the x-rays is denoted by θ, where $2d\sin(\theta)$ equals the difference in travelled path length between the x-rays interacting with the first and second planes of atoms. The x-rays will constructively interfere when the Bragg condition for diffraction is satisfied.

$$n\lambda = 2d\sin(\theta) \tag{4.1}$$

Where n is the order of diffraction (assumed to be 1), λ is the wavelength of the X-rays, and d_{hkl} is the atomic planar spacing of the (hkl) planes, where h, k, and l are the Miller indices. The peaks give information about the lattice parameters of the phases in a sample. Each crystalline material, therefore, has a characteristic pattern of peaks and peak intensities, which can be used to identify all the phases present in a sample. This pattern acts almost like a fingerprint for any material and varies for different crystal structures. Smaller grain size, resulting in smaller x-ray scattering domains, increases peak width, which is determined using the Debye–Scherrer formula:

$$D = \frac{K\lambda}{W\cos\theta} \tag{4.2}$$

where K is a dimensionless shape factor with no dimensions (0.94 for spherical grains), λ is the Cu-$K\alpha$ X-ray 0.154 nm, and W is the peak width at the Diffraction angle (full width at half maximum , in radians). As previously stated, the lattice parameters a and c for the CZTS tetragonal structure were estimated using the following equation:

$$\frac{1}{d^2} = \frac{h^2 + k^2}{a^2} + \frac{l^2}{c^2} \tag{4.3}$$

where (hkl) are the miller indices corresponding to XRD peaks, and d is the interplanar distance; and a and c are lattice constants. JCPDS Card No. 26-0575 provided the standard values of lattice parameters (a = 5.435 Å, c = 10.843 Å).

4.2.3.2 Identification of secondary phases

Identification of crystalline substances and crystalline phases in a sample can be achieved by comparing the sample's diffraction pattern with the patterns of known crystalline substances. In a powder diffraction file, X-ray diffraction information from a known substance is stored (PDF). Using CuK radiation, most PDFs are produced. The International Centre for Diffraction Data (ICDD) has published standard diffraction data that is periodically updated and expanded. X-ray diffraction from materials is detected by a diffractometer, which also records the intensity of the diffraction as a function of the diffraction angle, for identifying thin films' crystal structures. Only the detector rotates during operation to obtain the diffraction signal. CZTS samples are in the form of thin films on SLG slides. The sample remains in the same place while the source and detector scan the spectrum. The scans cover an angle range of 10° to 90°. In this work, XRD measurements were performed for all samples by using Cu-$K\alpha$ x-ray in Bruker d7 diffractometers. The XRD spectra were compared to reference patterns of kesterite CZTS (PDF 00-026-0575) stored in the International Centre for Diffraction Data (ICDD) database.

4.2.4 Raman spectroscopy

Raman spectroscopy is a complementary technique to XRD when analysing the crystal structure of a material. It is a non-destructive method of chemical analysis that can reveal information about a substance's chemical structure, phase, crystallinity, and molecular interactions. Raman spectroscopy detects specific light-matter interactions. Figure 4.10 shows three different types of scattering by molecules that have been stimulated by photons with energy $E = hv$. The method entails shining a monochromatic light source (such as a laser) on a sample and detecting the energy shift of dispersed light. Rayleigh or elastic scattering occurs when the bulk of the scattered light has the same frequency as the excitation source. Raman spectroscopy is a technique based on inelastic scattering of monochromatic laser light. Inelastic scattering means that the frequency of photons in laser changes upon interaction with a sample. This technique makes use of the existence of Stokes and Anti-Stokes scattering to investigate molecule structure. The Raman effect is classified into two types: Stokes scattering and anti-Stokes scattering. In Stokes scattering, an electron decays to a higher energy vibrational level than the one from which it was produced. As a result, the excess energy is ejected as a photon with a lower frequency than the incident photon. A photon with a frequency higher than the incident one is produced when an electron decays to an energetically lower vibrational state in the anti-Stokes scattering. When light is incident on a certain material, it interacts with the system's vibrational modes, changing the wavelength of the light that is reflected. As a result of that interaction the energy of the laser photons is being shifted up or down. This shift provides information about vibrational, rotational, and other low-frequency transitions in the system. The Raman shift in wave numbers and can be expressed by:

$$\delta\omega = \frac{1}{\lambda_I} - \frac{1}{\lambda_S} \tag{4.4}$$

where λ_I and λ_S are the wavelength of the incident and scattered photon wavelength

respectively. Thus, by measuring the energies of scattered radiation, a spectrum may be obtained as a function of Raman shift, with peaks at frequencies equivalent to the vibrational modes of a material.

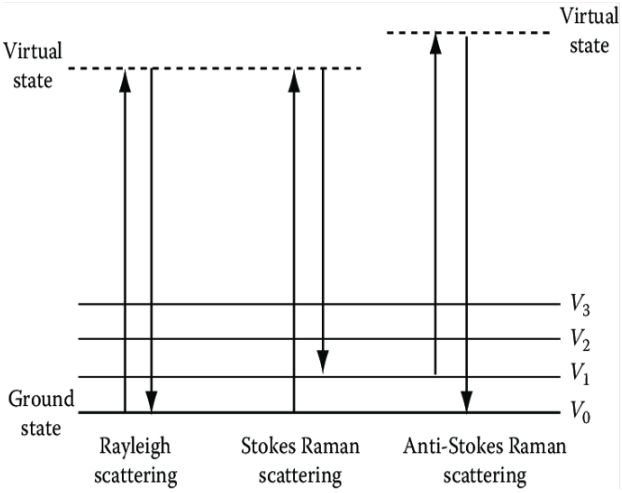

Figure 4.10: Energy-level diagram involved in the Raman Effect. Displays anti-Stokes and Rayleigh scattering by a molecule excited by a photon with energy $E = h\upsilon$.

In this study Raman spectroscopy was performed with a Horiba JY Lab RAM-HR Raman microscope, the acquisition time is 2 s. The sample was illuminated with a laser excitation wavelength of 532 nm and a power of 1.5 mW at the focus. For secondary phases identification, Peak fitting can be done using either Gaussian or Lorentzian functions, both of which are symmetrical around the peak point. The classic "bell-shaped" or "normal" curve or distribution is the Gaussian curve. The Lorentzian has 'wings' because it is a little bit narrower near its maximum and stretches outward a little bit more on its sides than the Gaussian. Gaussian fitting might not be as good near the wings of Raman peaks as it is in the center. Since a Lorentzian shows the best agreement with the measured peaks, it is used in this case for fitting.

4.2.5 Optical spectroscopy measurements

When light has passed through the sample solution and is detected in a UV/Vis spectrophotometer, its intensity is measured. The transmitted intensity, abbreviated I, refers to this portion of the light that the detector has detected. Because of, for example, the absorption of light at wavelengths, the sample solution reduces the intensity of the transmitted light. Consequently, it has a lower value than the light source's initial intensity, I_0.

$$T = I/I_0 \tag{4.5}$$

Transmittance T is defined as the ratio of the two intensities I and I_0 and has a unit of percent. The absorbance, denoted by A, is calculated as the inverse logarithm of the transmission

$$A = -\log(T) = \log(I_0/I). \tag{4.6}$$

The absorption coefficient of material α at a particular wavelength can be determined by absorption measurements at the corresponding wavelength following equation 2.1 which related the energy bandgap E_g to absorption [161]. The absorption was measured by (UV–Vis) spectro-photometer between 250 and 1250 nm. Using a so-called Tauc plot, which plots the squared absorbance A^2 against the photon energy, it is possible to extract the band gap energy from an absorbance spectrum. The energy band gap values were estimated by using a Tauc plot and extrapolating the linear region of the plot of $(\alpha h\upsilon)^2$ versus photon energy curves to intercept the horizontal photon energy axis. The ultraviolet–visible spectroscopy (UV–vis) was performed with the UV-vis spectrophotometer UV-3600 from Shimadzu in combination with the software UV Probe. The instrument is operated with a halogen lamp; it is operated at medium scan speed with a slit width giving a spectral resolution of 8.0 nm. The samples investigated are thin films on SLG

substrates in the wavelength range 250–1250 nm with a 0.2 nm step to record the absorbance of thin films. The absorption coefficient of a material α at a particular wavelength can be determined by absorption measurements at the corresponding wavelength. The following equation relates the energy bandgap E_g to absorption as follows:

$$\alpha h\upsilon = A\left(h\upsilon - E_g\right)^{\frac{1}{2}} \tag{4.7}$$

where α is the optical absorption coefficient, A is absorbance, h is Planck's constant, υ is frequency, and E_g is the optical band gap. The band gap values were estimated using equations (4–7) by extrapolating the linear portion of the $(\alpha h\upsilon)^2$ versus photon energy $(h\upsilon)$ curves to intercept the horizontal photon energy axis.

4.3 Summary

This chapter discussed the synthesis of CZTS nanocrystals using the hot injection method and described the two techniques used to deposit CZTS thin films, such as drop casting and spin coating. It also overviewed the films' characterisation techniques. X-ray diffraction (XRD) technique, which gives the crystal structures of materials present in CZTS, including associated parameters such as lattice parameters. Raman spectroscopy which can be used to identify materials using their vibrational, rotational, and other low-frequency modes, and to detect secondary phases in CZTS, scanning electron microscopy (SEM), which can give morphological images of the CZTS surface on the micro/nanoscale and nanoscale, and focused ion beam milling (FIB) for cross-section analysis. And finally, UV-Vis spectroscopy was used to study the optical properties of the CZTS thin films.

Chapter 5

Spin coated kesterite Cu_2ZnSnS_4: optical, structural, and morphological investigations for photovoltaic applications

5.1 Introduction

In this work, Cu_2ZnSnS_4 (CZTS) ink was synthesized using a simple and low-cost hot-injection method. Thin films of CZTS were then prepared by spin coating. The structural, morphological, and optical properties of CZTS nanocrystals can be controlled by optimizing synthesis parameters such as reaction temperature, reaction time, and precursor concentrations. CZTS nanocrystal-based approaches start with the controlled synthesis of nanocrystals and end with the deposition and post-treatment of films using the resulting inks [12]. After the synthesis of nanocrystals and fabrication of CZTS ink, nanocrystal ink was deposited onto different substrates such as glass, and Mo for use in different analyses. In this work, nanoparticle inks are applied onto a substrate by spin-coating followed by a soft-bake to remove the residual solvent using a hot plate. The spin-coating and soft-baking

procedures are repeated several times to yield the thin film with the desired thickness which is around 1 to 2 μm. The precursor inks were prepared by hot injection at different reaction temperatures and times, and were investigated to obtain phase pure CZTS films. Different aspects of CZTS thin films were characterized. The elemental composition, crystal structure, and phase purity of the films were investigated using EDX, X-ray diffraction (XRD), and Raman spectroscopy, respectively. In addition optical spectroscopy measurements were used to determine energy band gaps.

5.2 characterisation of the absorber layer

5.2.1 CZTS thin film as deposited characterisation

5.2.1.1 Composition analysis

The chemical composition is a very important parameter for high-performance photovoltaics. According to different studies, high efficiencies were obtained using Cu-poor and Zn-rich compositions for the absorber layer of CZTS thin films [7, 162, 163, 164]. In this study, the chemical composition of CZTS was determined using EDX. The composition ratios of films grown at 225 °C for 0.5 h, Cu/Zn+Sn and Zn/Sn, are 0.93, 1.53, respectively, as shown in Table 5.1

5.2.1.2 Morphological characterisation

To study the surface morphology of the CZTS thin film, a film deposited on a 25 x 25 mm^2 glass substrate coated by Mo, was investigated using SEM secondary electron imaging. As shown in Figure 5.1, from the SEM image the film exhibited uniform and compact morphology with cracks on the surface.

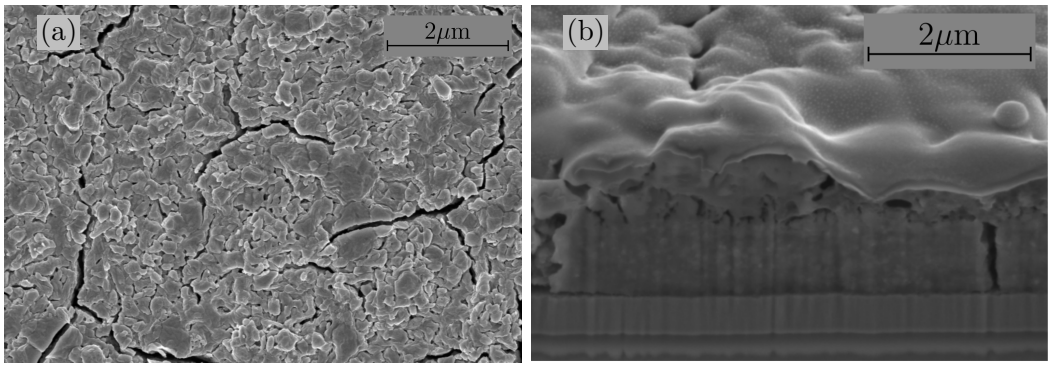

Figure 5.1: Top view(a) and cross section (b) SEM images of the as-deposited CZTS film on SLG coated by Mo substrate at reaction temperature 225 °C at 30 min at a magnification of 5k and 20k respectively

.

5.2.1.3 Structural characterisation

The crystal structure for CZTS thin films was characterized by X-rays using a Siemens D-5000 diffractometer using a Cu Kα radiation source ($\lambda = 0.15406$ nm) with a step size of 0.02°. XRD measurements were used to identify the crystalline phases present in the as deposited films. The XRD pattern of the CZTS thin film deposited by the spin coating method at a reaction temperature of 225 °C for 30 min is shown in Figure 5.2 (a). Four main peaks of the kesterite structure were found. The major XRD diffraction peaks appear at 28.5°, 33.3,°47.5°, and 56.3°can be attributed to the (112), (200), (220), and (312) planes of kesterite CZTS. In addition, week peaks were observed at 18.2°, 58.9°, 69,°and 76.4°and can be attributed to (101), (224), (008), and (332) planes of kesterite CZTS. These values are in agreement with ICDD 26-0575 [165, 166, 167]. The lattice parameters have been obtained from the XRD pattern $a = 5.413$ Å and $c = 10.788$ Å. This result agrees with the lattice parameters of single kesterite CZTS (PDF026-0575), where $a = 0.542$ nm and $c = 1.0848$ nm [166, 168, 169, 170, 171]. The size of the crystalline scattering domains was given by the Debye–Scherrer formula, equation 4.2. The nanocrystal domain size was found to be 17.81 nm. Some secondary phases in CZTS, such as $Cu_{2-x}S$, can be easily identified by XRD analysis. Because their diffraction peaks are distinct from those of CZTS, XRD can easily detect them. In

addition, XRD makes it simple to distinguish between the Sn_xS_y phases such as SnS, SnS_2, and Sn_2S_3 [15]. However, the XRD identification of ZnS and Cu_2SnS_3 phases is difficult because they have similar crystalline structures to CZTS, leading to the overlap of XRD peaks for CZTS, Cu_2SnS_3, and ZnS [172]. However, the positions of Raman peaks of CZTS and these secondary phases are different. Therefore, a Raman investigation was performed to discern secondary phases from the CZTS phase by using a single wavelength such as 532 nm [7]. Figure 5.2(b) shows the Raman spectra of the CZTS thin film synthesised at a reaction temperature of 225 °C for 30 min. The fitting with Lorentzian function curves of the Raman spectrum of the as-deposited sample gives evidence that the strong peaks in the spectra are located at 337 cm^{-1} and the shoulder peaks at 297 cm^{-1}, in addition to other peaks located at 251, 361, and 374 cm^{-1}. This is attributed to the kesterite phase of CZTS, which agrees with the results of previous studies [15]. Other peak observed at 277 cm^{-1}might be attributed to the ZnS phase [15].

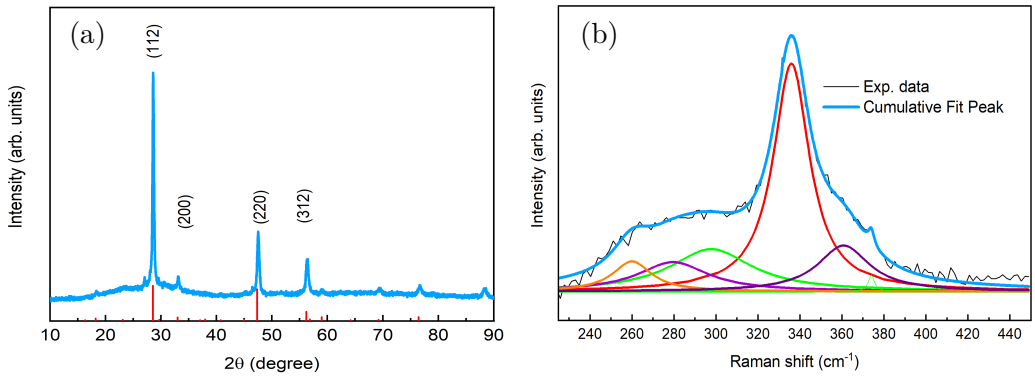

Figure 5.2: XRD patterns (a) and Raman spectra (b) of CZTS thin films deposited on glass substrate using ink synthesised for 0.5 hour at 225 °C.

5.2.1.4 Optical characterisation

Absorbance was measured using a UV–Vis–NIR Spectrophotometer between 450 and 1200 nm. The absorbance curve of the CZTS nanoparticle film grown at 225 °C for 0.5 h is shown in Figure 5.3. The band gap of the CZTS nanoparticle film value is shown in the inset using the Tauc relation. . By extrapolating the linear

portion of the $(\alpha h\nu)^2$ versus photon energy $(h\nu)$ curve with the interception of the horizontal photon energy axis, the value of the energy gap of the CZTS thin film was determined as 1.5 eV as shown in the inset of Figure 5.3. This result agreed with the reported value in the literature [7, 171, 173, 174].

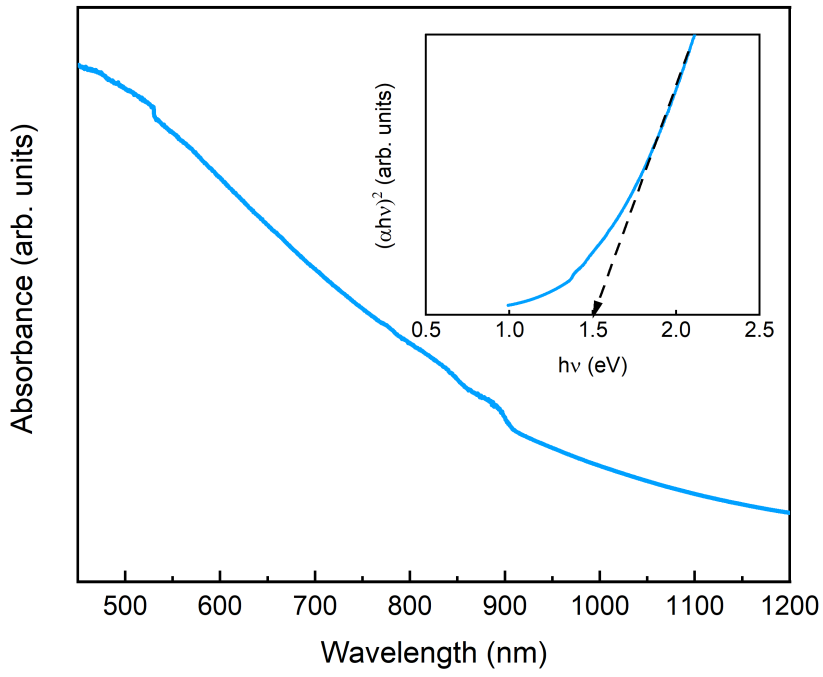

Figure 5.3: Absorption versus wavelength of CZTS film grown for 0.5 hour at 225 °C. The inset shows the Tauc Plot of $(\alpha h\nu)^2$ vs. $h\nu$.

5.3 The influence of reaction time

To investigate the effect of reaction time on the structural and optical properties of CZTS thin films deposited by spin coating, CZTS thin films were synthesized at 225 °C for three different annealing times (30, 45 and 60 min).

5.3.1 Chemical composition

Table 5.1 shows the chemical composition of CZTS thin films at different reaction times (30, 45, and 60 minutes at 225 °C). The ratios of Cu/(Zn+Sn) were less than one, indicating that the films are Cu-poor and Zn-rich.

Table 5.1: The chemical composition of CZTS thin films at various reaction times.

Reaction Time (min)	S (At %)	Cu (At %)	Zn (At %)	Sn (At %)	Cu/(Zn+Sn)	Zn/Sn	S/Cu+Zn+Sn
30	42.2	27.8	18.3	11.7	0.93	1.53	0.73
45	41.8	25.8	22.1	10.1	0.80	2.17	0.72
60	44.4	26.1	16.6	12.3	0.90	1.35	0.81

5.3.2 Crystal structure

5.3.2.1 X-ray diffraction

Figure 5.4 shows the XRD patterns of CZTS thin films prepared at different reaction times of 30, 45 and 60 min. Three major diffraction peaks of all samples are located at 28.5°, 47.1°, and 56.2°, which correspond to (112), (220), and (312) planes of the kesterite phase of CZTS, respectively [167, 175, 176]. The main peak increased in intensity significantly and became sharper and more intense for a reaction time of 60 min. Lattice constants a and c were determined as shown in Table 5.2 and agree with theoretical values [169, 175, 177]. The crystallite scattering domain size was calculated using the Debye-Scherer formula by measuring full-width half maxima corresponding to (112) planes. The domain size increases from 17.81 nm to 21.01 nm for 30 and 60 min reaction times, respectively.

Table 5.2: Lattice parameters, FWHM, and crystal scattering domain size for CZTS thin films at different reaction times.

Reaction time (min)	Lattice parameter a (nm)	Lattice parameter c (nm)	FWHM (degree) Peak (112)	scattering domain size (nm)
30	0.5413	1.078	0.46	17.81
45	0.5421	1.073	0.55	14.90
60	0.5421	1.085	0.39	21.01

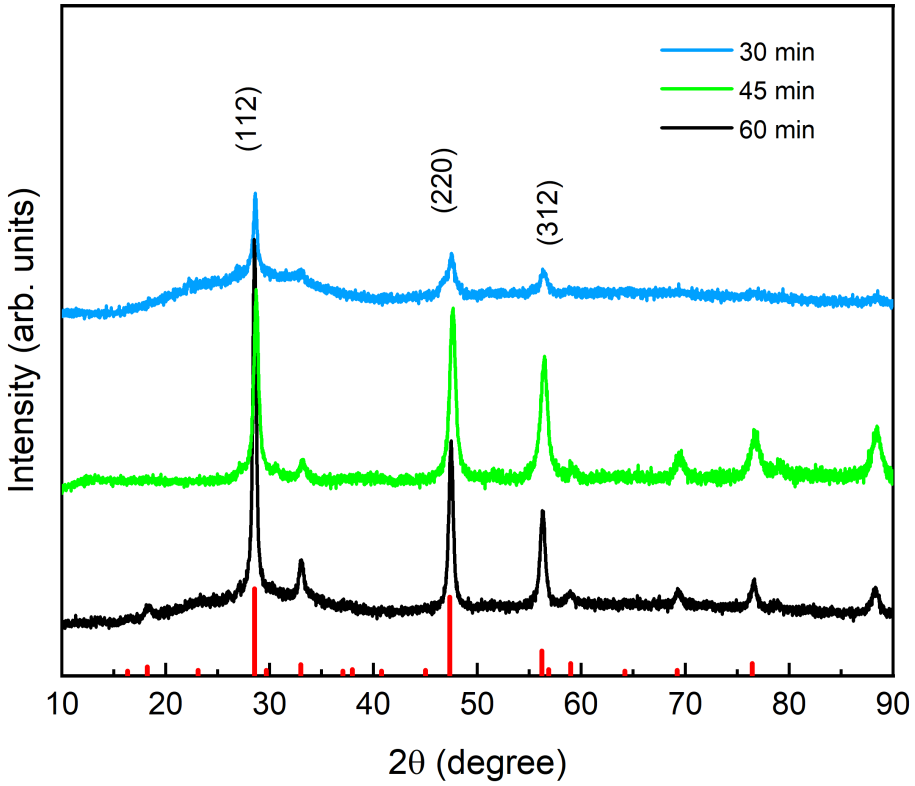

Figure 5.4: The XRD spectra of CZTS thin films deposited on glass and synthesised at different reaction times at 225 °C. The reference values PDF026-0575 are shown in the red stick plot.

5.3.3 Optical characterisation

The Tauc plot calculated from absorbance spectra for CZTS thin films with different reaction times 30 and 60 min is shown in Figure 5.5. The estimated energy gap decreased from 1.5 to 1.3 eV as a result of increasing annealing time from 30 to 60 min, which agrees with previous studies [178]. The change in the band gap may be due to the improved crystallinity of the CZTS thin film synthesis at 30 min reaction time [172].

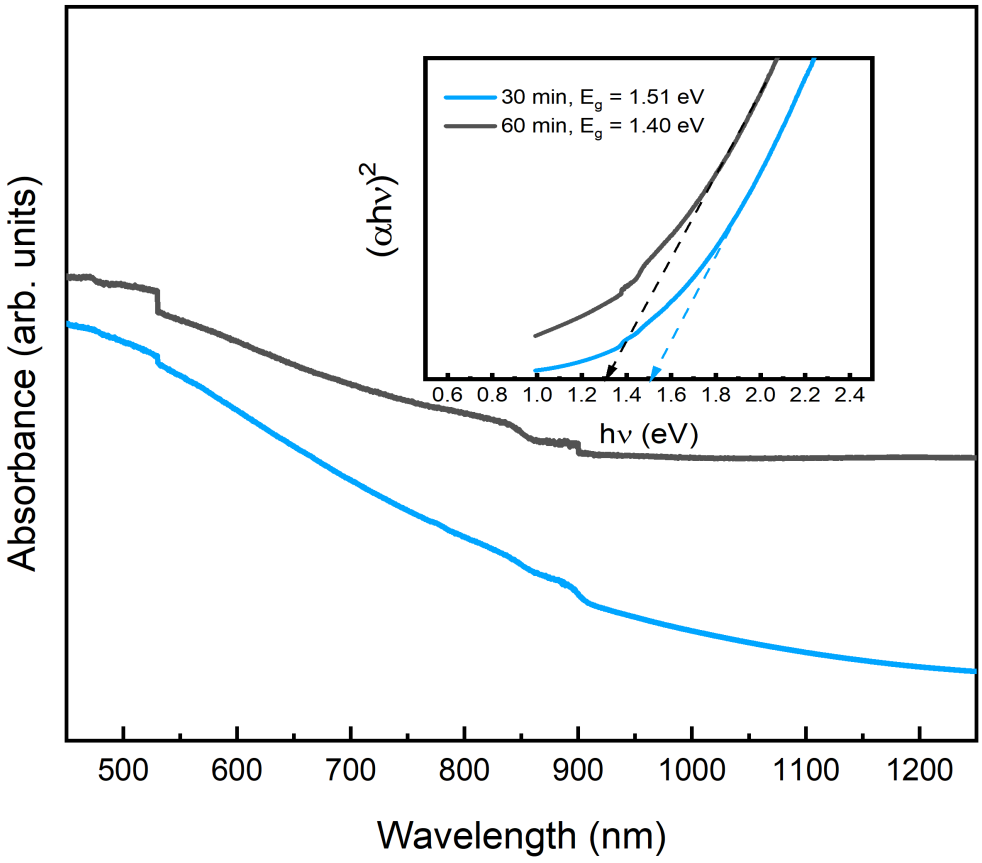

Figure 5.5: Absorbance versus photon energy for CZTS thin films synthesised at reaction time (30, 60 min). The inset shows a plot of $(\alpha h\nu)^2$ vs. $(h\nu)$ used to determine the optical band gap.

5.4 Influence of reaction temperature

The reaction temperature is one important parameter as it can be used to minimize the formation energy of CZTS in relation to other stable secondary phases. However, this parameter can also have an influence on the crystallographic disorder in the growing crystal as well as the growth mechanism during the reaction. An increase in reaction temperature will enhance the crystal growth rate [7]. To investigate the effects of synthesis at lower and higher reaction temperatures on the structural and optical properties of CZTS thin films, different thin films were synthesized at a reaction temperature range of 175-250 °C.

5.4.1 Chemical composition

The chemical composition of CZTS thin films at different reaction temperatures is shown in Table 5.3. At reaction temperatures of 175, 185, 200, 220, 225, 235, and 250 °C, the compositional ratio was Cu/(Zn+Sn) = 0.78, 0.93, 0.94, 0.93, 0.96, and 0.49, respectively. The ratio of Cu/(Zn+Sn) was less than one, indicating that the films are Cu-poor and Zn-rich. Furthermore, at 250 °C, there was a significant decrease in the atomic percentage of S and an increase in the relative content of Sn and Zn.

Table 5.3: Chemical composition for CZTS thin films at different reaction temperatures (RT) at a reaction time of 30 min.

RT (°C)	**S (At %)**	**Cu (At %)**	**Zn (At %)**	**Sn (At %)**	**Cu/(Zn+Sn)**	**Zn/Sn**	**S/Cu+Zn+Sn**
175	43.4	24.7	23.0	8.6	0.78	2.68	0.77
185	42.2	27.8	24.1	5.7	0.93	4.17	0.73
200	44.0	27.6	24.8	4.3	0.94	5.74	0.77
220	44.8	26.1	16.6	12.3	0.91	1.37	0.81
225	42.2	27.8	18.1	11.7	0.93	1.53	0.73
235	45.2	25.8	19.6	9.2	0.96	2.13	0.82
250	26.8	24.1	27.9	21.1	0.49	1.32	0.54

The sudden change in the ratios over the temperature range 210-240 °C is consistent with the occurrence of the CZTS order-disorder transition in this temperature range previously observed in CZTS polycrystals [179].

5.4.2 Film morphology

Figure 5.6 shows the SEM surface images of the CZTS thin films with different reaction temperatures in the range of 175-235 °C. At reaction temperatures of 175-235 °C, the films generally have compact arrangements of nanoparticles with spherical particles observed at high resolution. Films synthesised at 175, 185 and 235 °C demonstrate cracks. Cracks are less prominent at other ink synthesis temperatures. This implies that the presence of cracks may be a function of film deposition procedures as well as synthesis temperatures. Moreover, surface particles were ob-

served at the surface at reaction temperatures of 185, 200, and 235 °C which might be an indication of the presence of secondary phases.

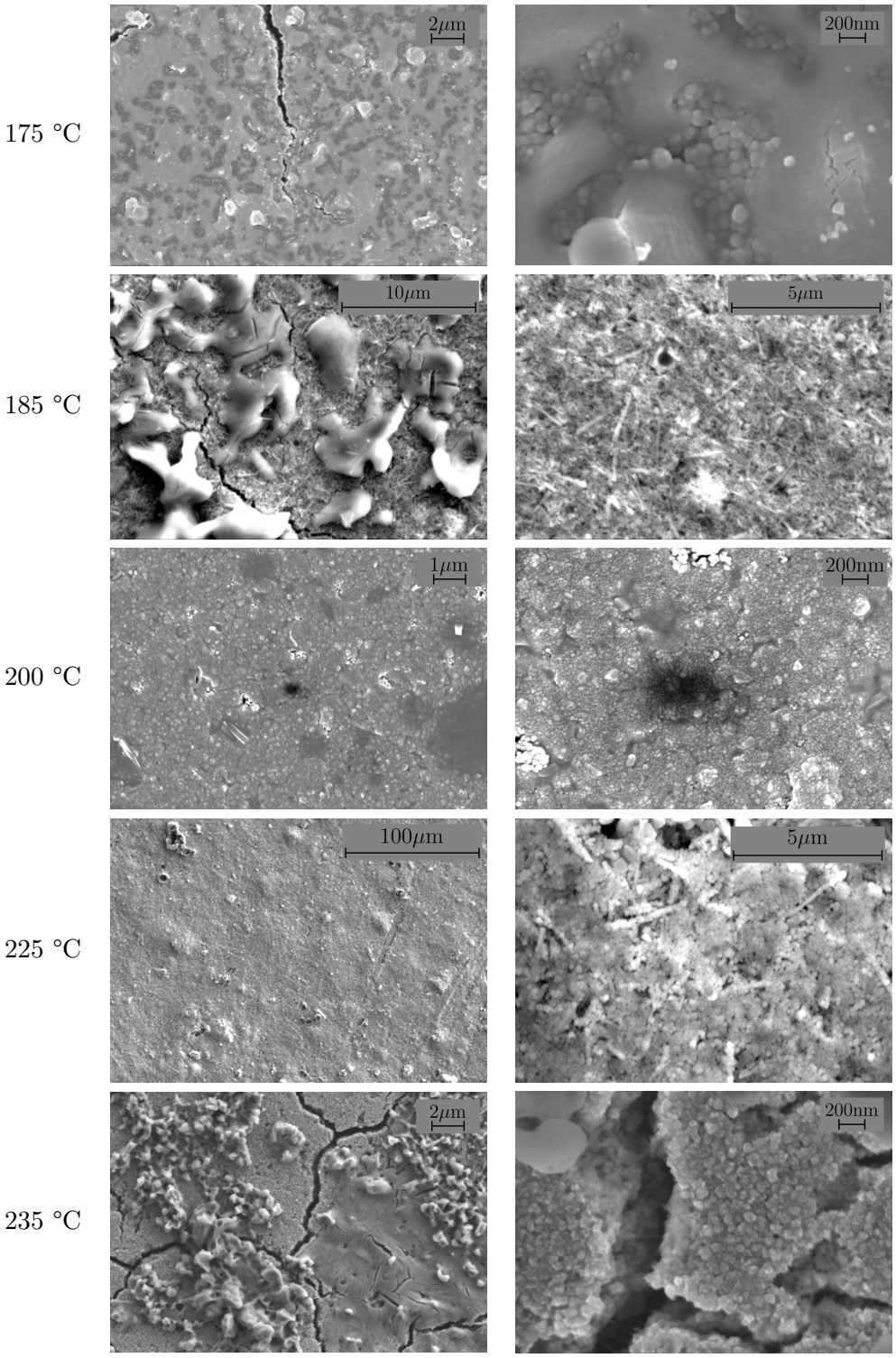

Figure 5.6: SEM plan view images of the thin film synthesised at different reaction temperatures 175-250 °C at reaction times of 0.5 h.

5.4.3 Crystal structure

5.4.3.1 X-ray diffraction

Figure 5.7 shows the XRD patterns of CZTS films synthesised at different reaction temperatures. Three major diffraction peaks of all samples are located at 28.5°, 47.2°, and 56.4°, which correspond to (112), (220), and (312) planes of the kesterite phase of CZTS, respectively . These values are in agreement with (PDF 026-0575) [168]. The calculated values of lattice parameters a and c in Table 5.4 are in good agreement with theoretical values in the literature [168, 169]. In addition to the main peaks, weak diffraction peaks were observed at reaction temperatures of 175 °C and 185 °C located at 26.5°, 31°, and 51.8°, which might correspond to (210), (211), and (213) planes of wurtzite structure of CZTS. Some particles observed on the film surface at 175, 185 °C, as shown in Figure 5.6 might be attributed to secondary phases. They disappeared at higher reaction temperatures of 225 and 250 °C. Table 5.4 shows a variation in the crystallite scattering domain size at different reaction times, as determined from the XRD FWHM. A significant increase in crystallite scattering domain size is observed for films with an increase in reaction time in the range of 185–225 °C, then decreases at a higher reaction time. The estimated values of crystallite scattering domain size and lattice constants are shown in Table 5.4. The largest crystallite scattering domain size at 225°C reaction temperature is estimated at 26.54 nm.

Table 5.4: Lattice parameter, FWHM, and scattering domain size for deposited CZTS thin films synthesised at different reaction temperatures.

Reaction temperature (°C)	**Lattice parameter $a = b$ (nm)**	**Lattice parameter c (nm)**	**FWHM (degree) Peak(112)**	**Scattering domain size (nm)**
175	0.5406	1.0955	0.46	16.73
185	0.5402	1.0746	0.56	13.74
200	0.5408	1.0858	0.50	15.39
220	0.5415	1.0830	0.44	17.49
225	0.5411	1.0811	0.29	26.54
235	0.5415	1.0830	0.45	17.10
250	0.5409	1.1068	0.48	16.03
ICDD 26–0575	0.5427	1.0848		

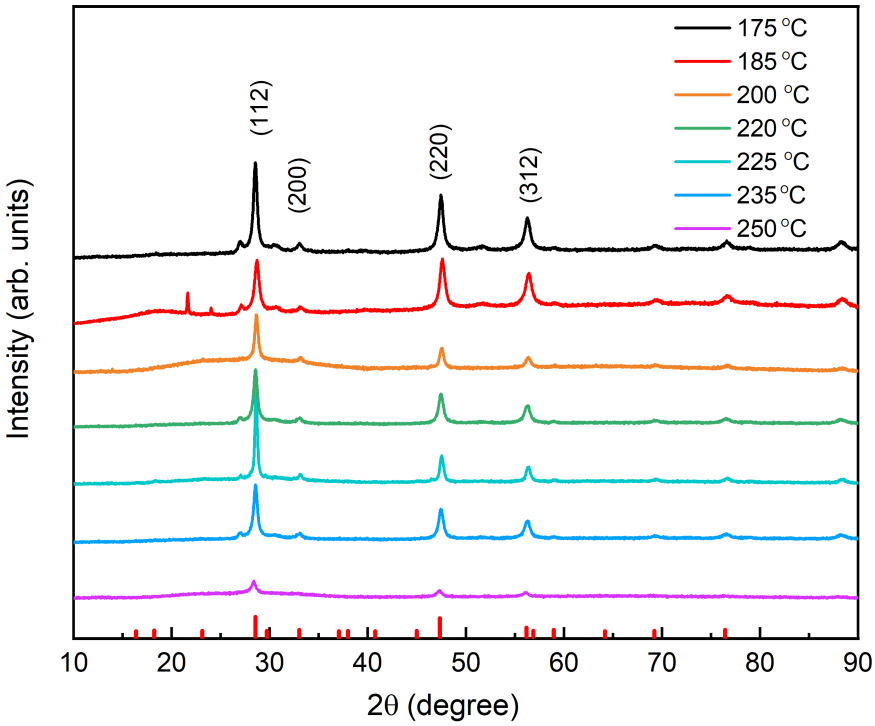

Figure 5.7: The XRD patterns of CZTS thin films synthesised at different reaction temperatures in the range (175-250 °C). The reference PDF026-0575 is shown in the red stick plot.

5.4.3.2 Raman spectroscopy

Figure 5.8 shows Raman spectra obtained with the 532 nm excitation of thin films synthesised at different reaction temperatures. The main Raman peaks are located at 337, 339, 339, 339, 336, and 338 cm^{-1} for reaction temperatures of 175, 185, 200, 220, 225, and 235 °C respectively, which is close to the reported values of the characteristic CZTS peak (325-339 cm^{-1}). These are obtained from fitting Lorentzian curves to the Raman spectra. At reaction temperatures of 175 and 220 °C peaks were also observed at 351 cm^{-1}, which indicates the existence of ZnS. For a reaction temperature of 185 °C a peak was observed at 474 cm^{-1} and it might correspond to Cu_2S [15]. Peak broadening and peaks observed at 354 cm^{-1} indicate the presence of the ZnS phase at reaction temperatures of 200 °C and 250 °C, respectively.

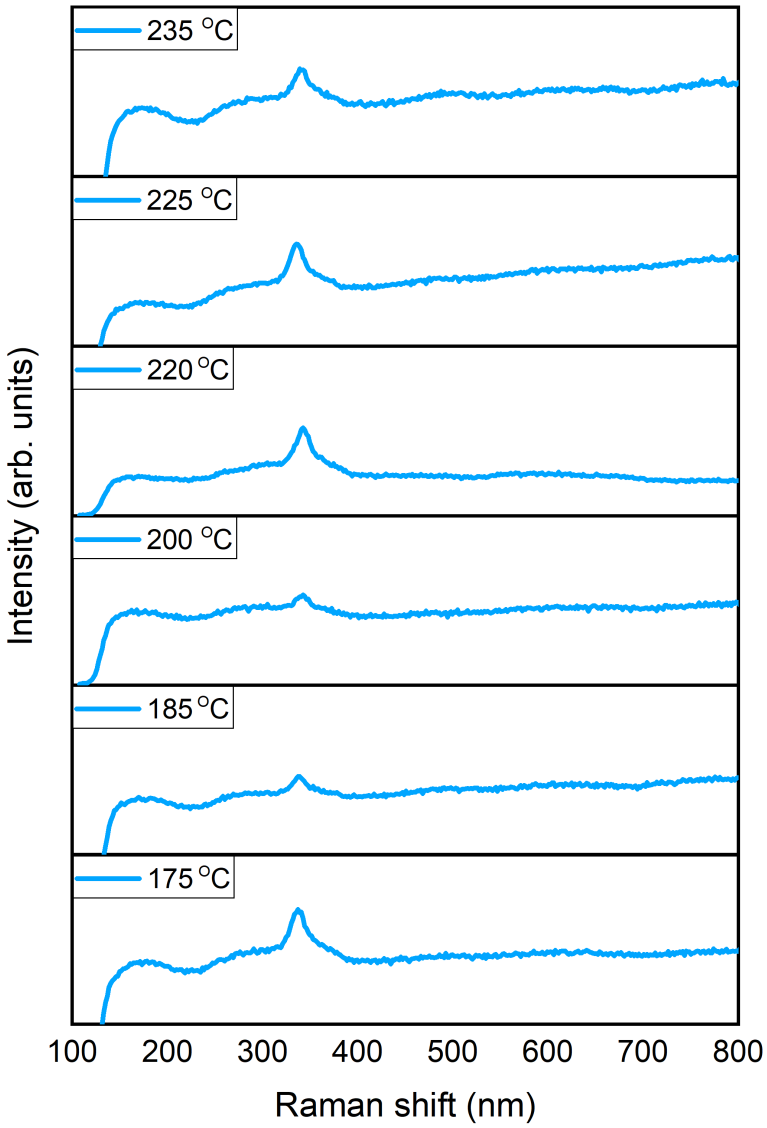

Figure 5.8: Raman spectra of CZTS thin films synthesised at different reaction temperatures.

5.4.4 Optical characterisation

The absorption spectra for CZTS thin films were measured at wavelengths in the range of 250–1250 nm for different film reaction temperatures. Figure 5.9 shows the Tauc plot of $(\alpha h\nu)^2$ versus photon energy $(h\nu)$. The optical band gap was

determined to be in the range of 1.20-1.42 eV and matches the previous studies [12, 164, 178]. Figure 5.9 shows the increase in optical band gap with increasing reaction temperature, up to a reaction temperature of 200 °C. Above this, there is a decrease in the energy gap. The optical band gap of CZTS thin films is correlated with the phase purity, crystalline phase, elemental composition, grain size, etc [20]. With an increasing reaction temperature from 220-235 °C, the decrease in CZTS band gap energy could be attributed to an increase in the Cu/(Zn + Sn) ratio [180]. Whereas the presence of secondary phases may explain the increase in energy gap at lower temperatures [20], such as the ZnS phase at reaction temperatures of 175, 185, and 200 °C. This is in agreement with EDX measurements which show that the Zn/Sn ratios at reaction temperatures of 175, 185, and 200 °C are 2.68, 4.17, and 5.74, respectively.

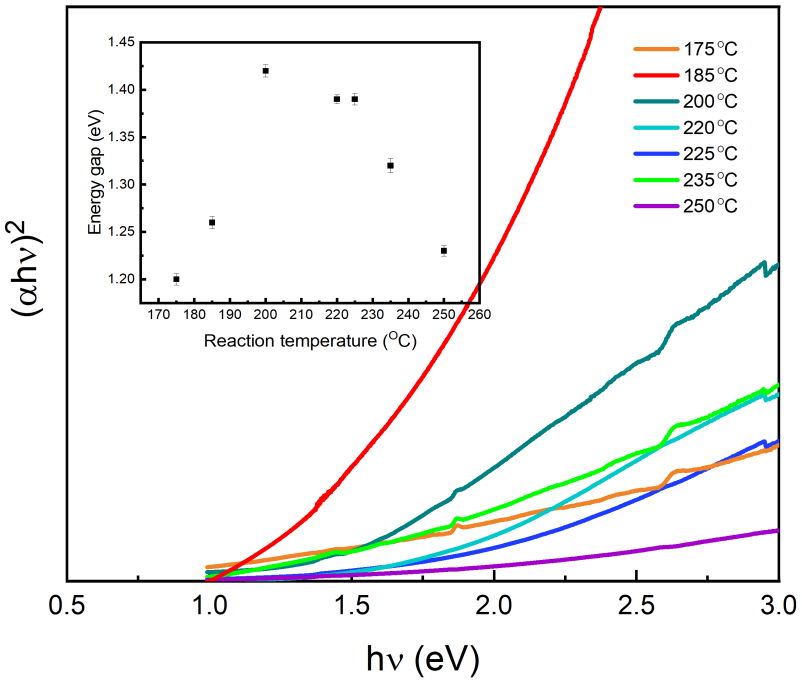

Figure 5.9: Tauc Plot of $(\alpha h\nu)^2$ versus photon energy $(h\nu)$ for CZTS for samples at different reaction temperatures, used to determin the energy band gap.

Table 5.5: Variation of optical band gap with the variation of reaction temperatures

Reaction temperature (°C)	**Energy gap (eV)**
175	1.20
185	1.26
200	1.42
220	1.39
225	1.39
235	1.32
250	1.23

5.5 Summary

The hot injection method was used to successfully synthesize CZTS nanoparticles at different reaction times and temperatures. Inks were deposited onto clean glass using spin coating procedures at a high speed (2500 rpm) for 15 seconds after being synthesized at 225 °C for 30 minutes. A CZTS nanoparticle-based control sample that was synthesized at 225 °C for 30 minutes had a kesterite crystal structure. The average composition of the CZTS nanoparticles was controlled by adjusting the precursor molar ratios into a Cu-poor and Zn-rich region of the phase diagram. The synthesised Cu/(Sn+Zn) ratio was 0.93, and the Zn/Sn ratio was 1.53. The CZTS nanoparticles were almost spherical in form. The XRD pattern shows three main peaks of the kesterite structure were found. The major XRD diffraction peaks appear at 28.5°, 47.5°, and 56.3° and can be attributed to the (112), (220), and (312) planes of kesterite CZTS. The lattice parameters have been obtained from the XRD pattern: $a = 5.413$ Å and $c = 10.788$ Å. Optical spectroscopy shows the energy band gap to be 1.50 eV. Investigations were done into how the fabrication parameters of temperature and time affected the properties of CZTS thin films. It was revealed that band gap, composition, and crystal structure are significantly influenced by temperature (175, 185, 220, 225, 235, and 250 °C) and time (30, 45, and 60 min).

Chapter 6

Effects of heat treatments on Cu_2ZnSnS_4 thin films deposited by the spin coating technique

6.1 Introduction

Many studies have been conducted to improve CZTS photovoltaic conversion efficiency by reducing secondary phase formation, reducing interface recombination, and improving the crystal quality of CZTS solar cells through various thermal treatments of the CZTS absorber layer. Shi et al. found that a photovoltaic conversion efficiency of 9.80% was achieved by air-annealing because of the pre-treatment of a Cu_2ZnSnS_4 precursor thin film prior to selenisation, which can lead to sodium diffusion into the CZTS precursor thin film and surface oxidation of the CZTS thin film. The surface oxidation of the CZTS precursor thin film and the Na diffusion can promote the crystal growth of the CZTSSe thin film, which can lead to the removal of the small-particle bottom layer and the formation of a large grain-spanned CZTSSe thin film [117]. Zhang et al. investigated how air annealing of CZTS affected the crystal quality of the CZTSSe absorber. In a different group investigation, the impact of air-annealing on the photovoltaic performance of CZTSSe

solar cells was studied. CZTS precursor films were annealed in the range of 100 to 500 °C before selenisation. It has been discovered that air-annealing the CZTS precursor film increased conversion efficiency from 7.50 % to 8.94 % [181]. Ziti et al. investigated how CZTS thin films' structural, optical, and electrical properties are affected by annealing in air at different temperatures. CZTS which was made using the sol-gel method, and deposited using the spin coating technique, was studied to determine how the annealing temperature affected its structural, optical, and electrical characteristics. For 10 minutes, the samples were annealed in air at 300, 325, and 350 °C. Additionally, a higher electrical resistivity in the region of 0.1-0.15 Ωcm was reported, and the band gap energy increased from 1.5 to 1.63 eV [182]. The effects of different substrate temperatures on the optoelectronic and structural characteristics of spray pyrolysis CZTS were examined by Thiruvenkadam et al. XRD experiments showed that increasing substrate temperature increased crystallinity. They discovered that as the substrate temperature rose, the average roughness and grain size increased [183]. Ahmoum et al. investigated the impact of preheating spin-coated CZTS films in air, argon, and nitrogen atmospheres before sulphurisation on the material properties of the resulting CZTS thin films [169]. Long et al. found that preheating treatment factors such as preheating temperature and preheating time have a significant impact on the characteristics of CZTS thin films [184]. These studies confirm that heat treatment has a significant impact on properties of CZTS relevant to PV performance. There is therefore a need to investigate the impact of heat treatment on nanocrystal ink samples.

In our study, the effect of preheating treatment of CZTS thin films before sulphurisation on the morphology and structural, optical, and electrical properties of the films was investigated. Different CZTS nanoparticles were synthesized via the hot injection route, previously described in Chapter 5. Samples with off-stoichiometric Cu-poor and Zn-rich compositions were preheated on a hot plate in air (hot plate annealing).The films have been characterized by X-ray diffraction (XRD), Raman spectroscopy, scanning electron microscopy (FIB, TEM), energy dispersive X-ray

spectroscopy (EDX), and UV-Vis-IR spectroscopy.

6.2 The influence of preheat treatment on Cu_2ZnSnS_4 thin films

In this work, Cu_2ZnSnS_4 thin films are deposited on a SLG substrate using spin coating at speed 2500 rpm for 15 sec. The films' composition ratios, Cu/(Zn+Sn) and Zn/Sn, are set at 0.85 and 1.25, respectively. The deposited films were subjected to preheat treatment, which was carried out in air using a hot plate at different temperatures and times. The influence of hot plate preheating parameters such as temperatures and times on the structural, compositional, optical, and morphological properties of the spin coated CZTS thin films were studied.

6.2.1 Influence of preheat treatment time on CZTS thin films

6.2.1.1 Structure characterisation

Figure 6.1 shows the XRD pattern of a CZTS thin film preheated on a hot plate for 3, 12, and 30 min at a fixed temperature of 310 °C. In all films, the main peaks are observed at 28.46°, 47.35° and 56.17° which correspond to the (112), (220), and (312) planes of the kesterite CZTS phase which agrees with the kesterite reference phase (PDF 026-0575). The major peaks' intensity become sharper because of the increasing preheating time. However, after 30 minutes of heating, the intensity decreased and the main peaks shifted slightly to the left, as shown in Figure 6.1. The main peaks are shifted at 27.98°,32°, 46.60° and 55.51°. Table 6.1 shows the full width at half maximum (FWHM) as calculated from XRD peak for as-deposited and the annealed samples. The decrease in the value of FWHM indicates improvement in the calculated scattering domain sizes. The scattering domain size increases with increasing time except for the 30 minute sample. The lattice

parameters a and c of CZTS have been calculated for all the XRD patterns as shown in Table 6.1.

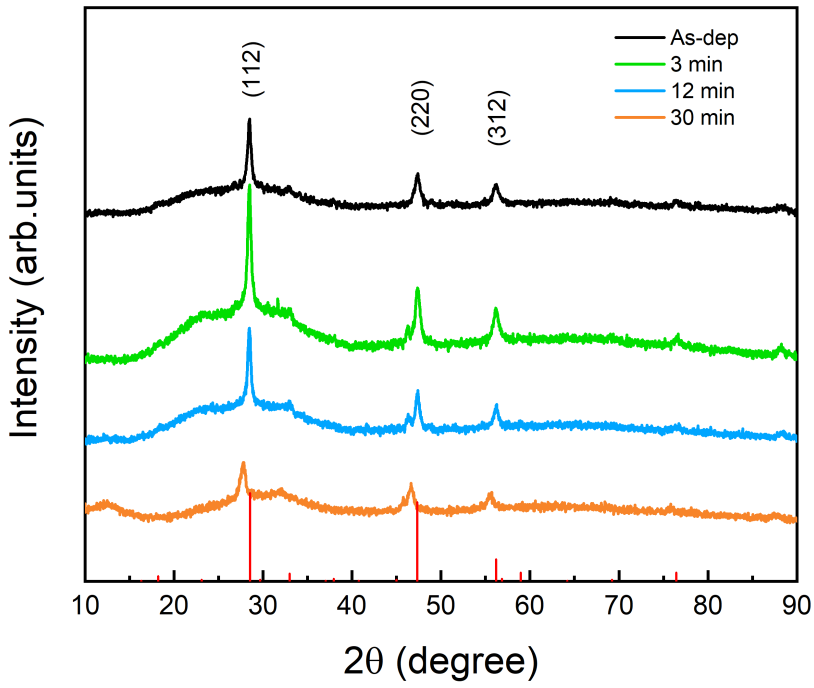

Figure 6.1: XRD patterns of as deposited and preheated films at 310 °C on a hotplate at different times.A reference pattern from the ICDD database for kesterite Cu_2ZnSnS_4 (PDF 00-026-0575) is shown as a stick plot.

Table 6.1: The peak intensity, lattice parameters a and c, FWHM, and scattering domain size of CZTS thin films at different preheating times.

Time (min)	$I_{112}/(I_{220}+I_{312})$	**Lattice parameter**	**Lattice parameter**	**FWHM (degree) Peak**	**Scattering domain size (nm)**
		a **(nm)**	c **(nm)**	**(112)**	
As-dep	663	0.5410	1.0832	0.55	14.90
3 min	1214	0.5425	1.0828	0.45	18.21
12 min	1209	0.5411	1.0833	0.44	18.62
30 min	331	0.5422	1.0837	0.62	13.19

6.2.1.2 Optical characterisation

The absorption spectra of the CZTS thin films were measured on the films with different preheating times of 3, 6, 9, and 12 minutes at hot-plate temperature of 310 °C, in the wavelength range 450-900 nm, as shown in Figure 6.2. The absorbance decreased as the wavelengths increased. In Figure 6.3, the energy bandgaps are estimated from the absorbance spectra by plotting the data on a Tauc plot. It is obvious that there is variation in the optical band gap as a result of preheating time. The differences in the estimated energy gaps might be due to the existence of secondary phases in the films, or changes to the composition of the CZTS films. The bandgap increases with annealing time for shorter anneals, it reduces after the 12 minute anneal, increasing for the 30 minute anneal.

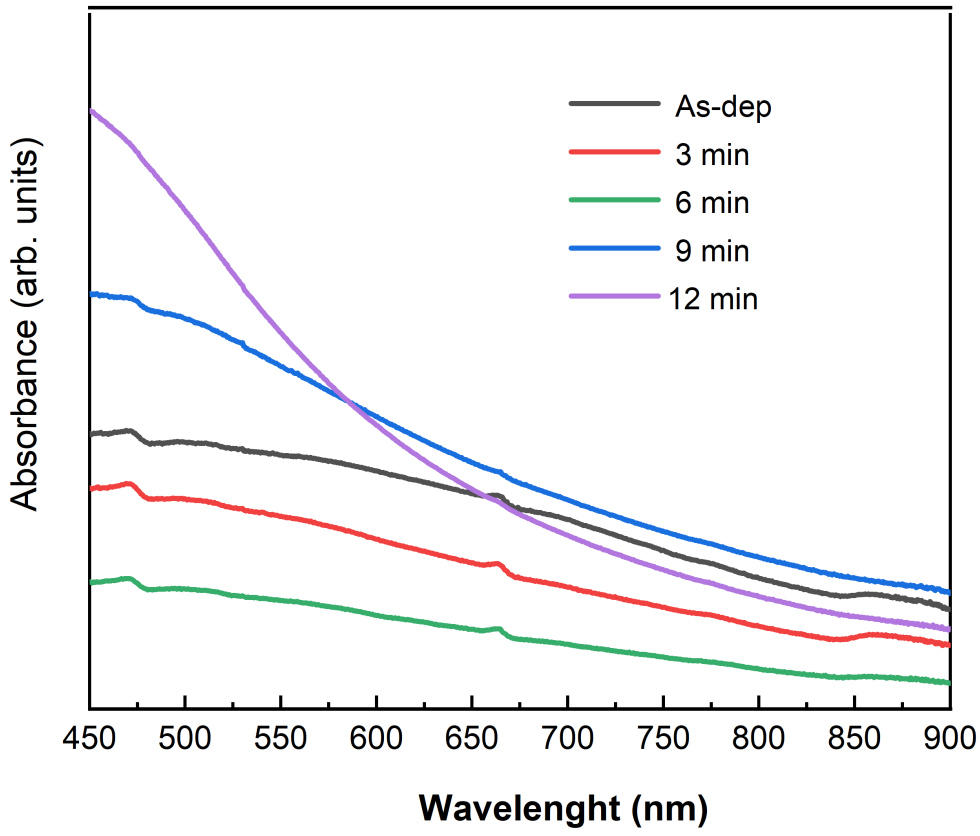

Figure 6.2: Absorption spectra of CZTS thin films heated on a hotplate at a temperature of 310 °C at different times.

6.2.2 Influence of preheating temperatures on CZTS thin films

In this section, the impact of different preheating (hot plate annealing) temperatures on the CZTS thin film properties was investigated. Different CZTS thin films were preheated at different hotplate temperatures from 150 °C to 230 °C for 3 min.

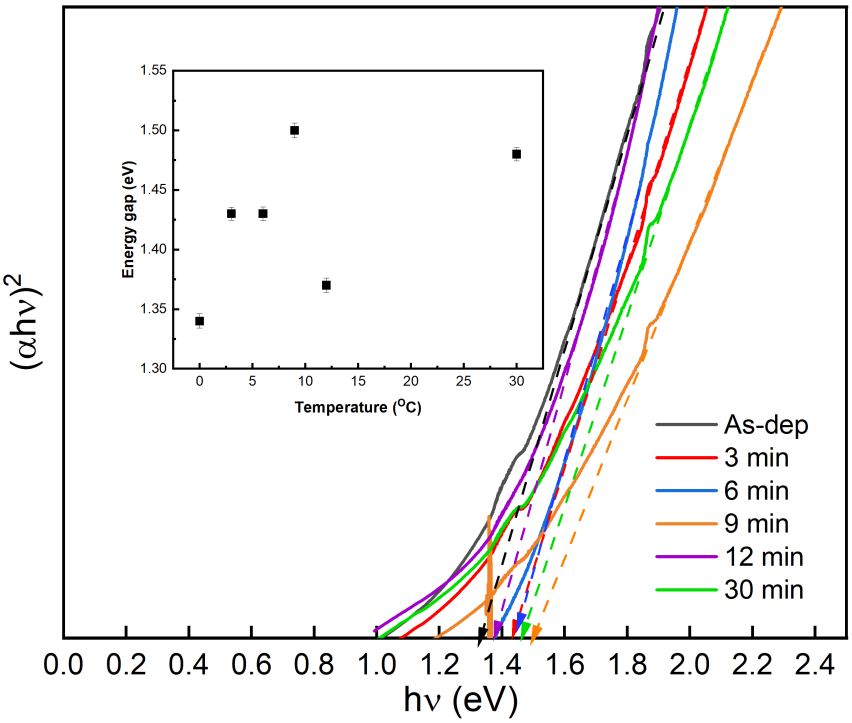

Figure 6.3: Tauc plot of $(\alpha\ h\nu)^2$ versus photon energy $(h\nu)$ for CZTS thin films heated at various times at a constant temperature of 310 °C. The intercept of the straight line fit gives the values of the energy bandgap.

6.2.2.1 Structure analysis

Raman spectroscopy provides a reliable method of identifying secondary phases. The Raman spectra of CZTS thin films preheated on a hot plate for 3 minutes at temperatures of 150, 170, 190, 210, and 230 °C are shown in Figure 6.4. The fitting with the Lorentzian function shows the main Raman peak is located at

338 cm^{-1}. Other peaks at 330 cm^{-1} are attributed to the A vibrational mode of kesterite phase CZTS and 331 cm^{-1} to the disordered mode corresponding to the other vibrational mode of CZTS. In addition, secondary phases such as CuS and $Cu_4Sn_7S_{16}$ were detected at 471 and 365 cm^{-1}, respectively.

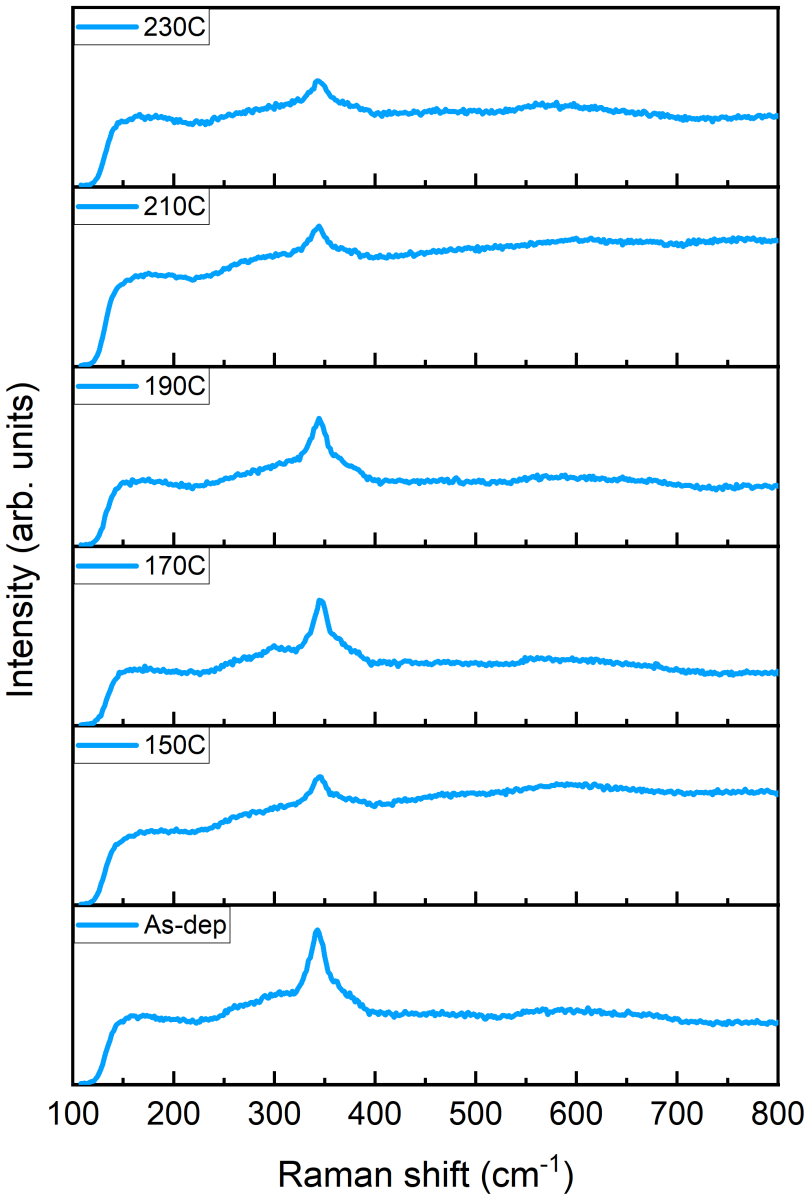

Figure 6.4: Raman spectra of CZTS thin films heated at 150–230 °C for 3 min.

6.2.2.2 Morphology analysis

Figure 6.5 shows the morphology of the films at different preheating temperatures 170, 190 and 230 °C. It is obvious that the film heated at 170 °C has a uniform and compact cross section without any cracks or holes, which thereby assist in absorption as shown in Figure 6.6, whereas at higher preheating temperatures there are holes that appear in the CZTS cross section .

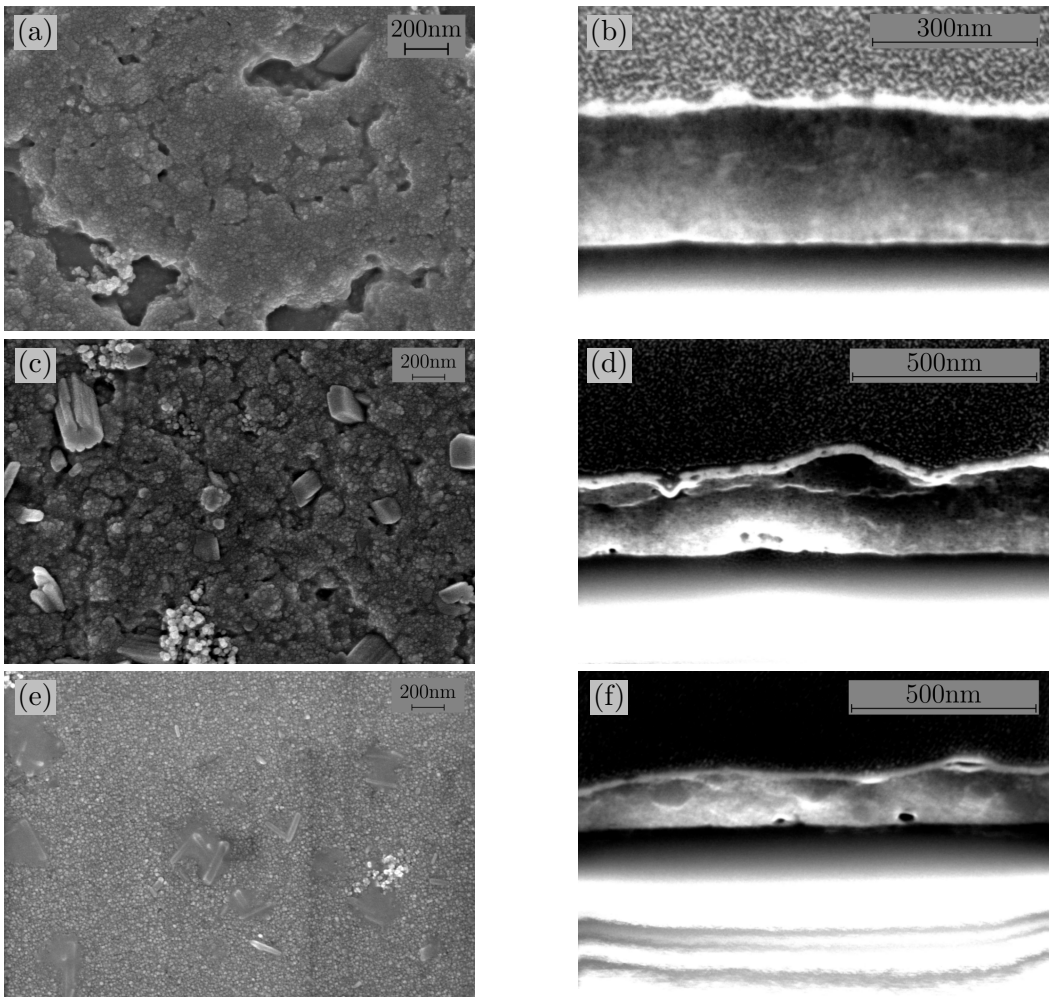

Figure 6.5: Top view and cross-sectional SEM image view of preheated CZTS films,at a magnification of × 40k in the left-hand column and of × 100k in the right-hand column respectively. (a, b) 170 °C, (c, d) 190 °C, and (e, f) 230 °C

6.2.2.3 Optical analysis

Figure 6.6 shows the absorption spectra of preheated CZTS films at different hot-plate temperatures from 150-230 °C for thin films synthesised at a reaction time of 30 min, in which the film preheated at 170 °C shows enhanced absorption in the visible region. The enhanced absorption of the light assists efficient electron-hole charge separation and thus contributes to increasing solar cell performance.

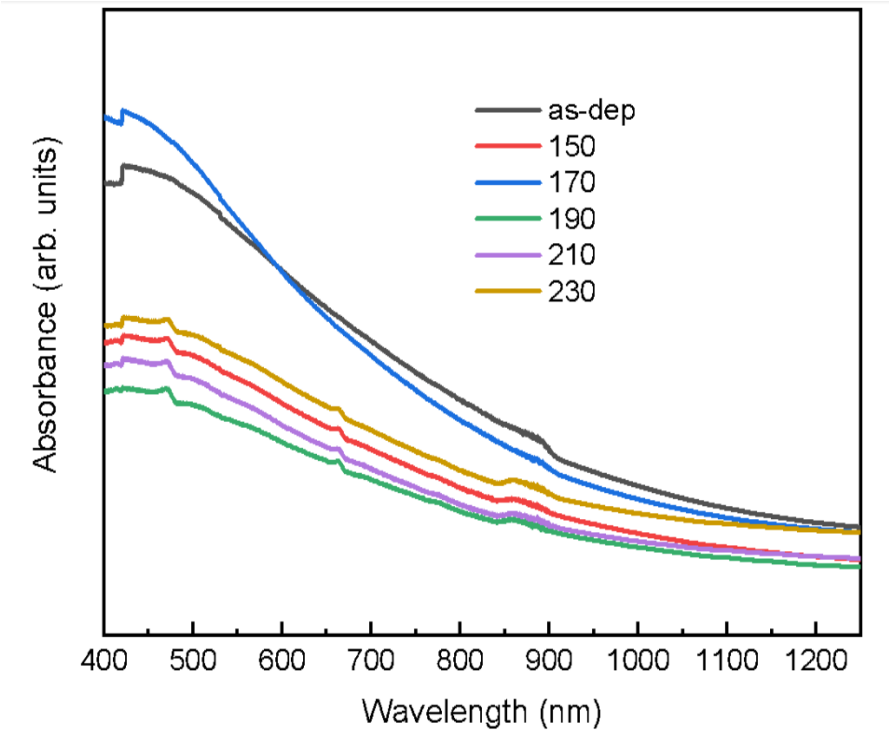

Figure 6.6: UV-Vis absorption spectra of the as-synthesized CZTS thin film and preheated thin films at different hot-plate temperatures 150-230 °C for 3 min.

There is variation in the energy bandgap (Eg) between different hotplate heat treatments that is observed in all pre-heat treatments, as shown in Figure 6.7. The energy gaps are estimated to be 1.38, 1.30, 1.35, 1.41, and 1.40 eV. The increase in optical band gap can be attributed to the decrease in Cu/(Zn+Sn) ratio or the existence of secondary phases, which have a higher optical band gap [20].

For a reaction time of 60 min, the absorption spectra shown in Figure 6.8 for different preheating temperatures with their estimated energy gaps shown in Figure

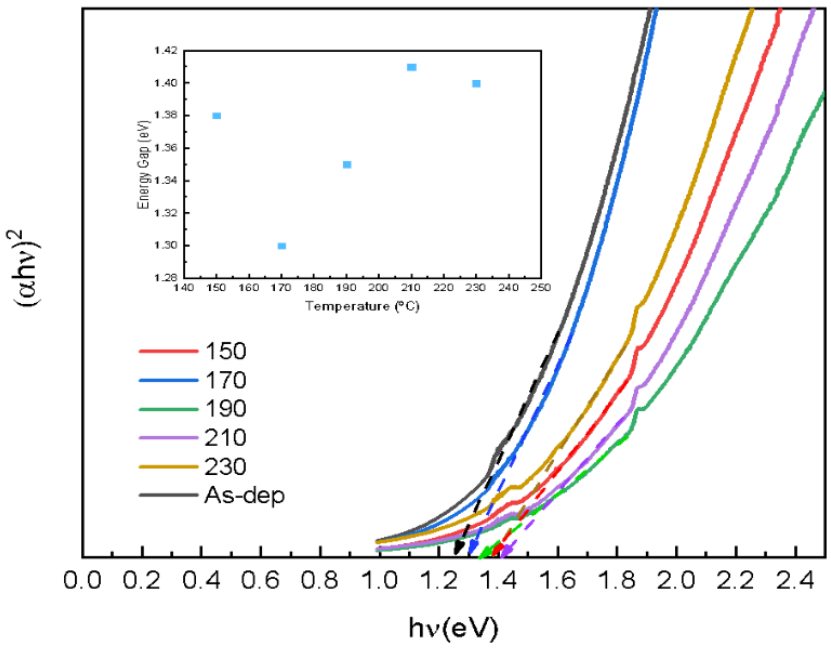

Figure 6.7: Plot of $(\alpha\ h\nu)^2$ vs photon energy at different preheating temperatures. The estimated energy gaps are shown in the inset.

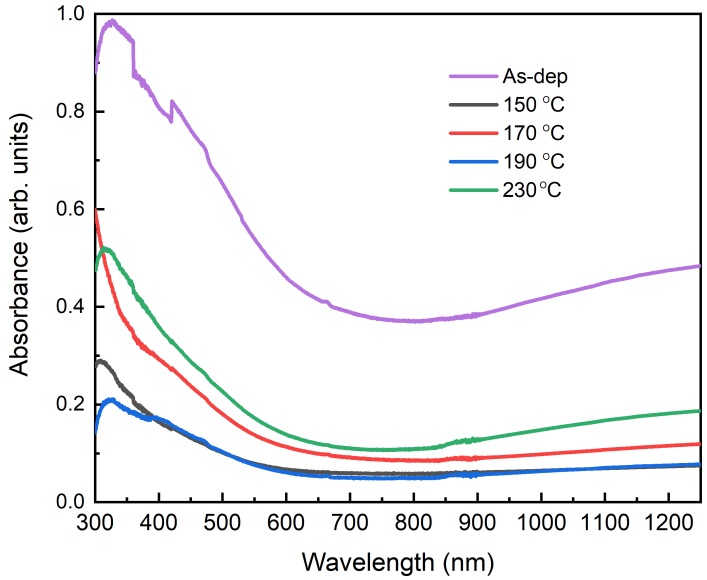

Figure 6.8: UV-vis absorption spectra of the as-synthesized CZTS thin film at reaction time of 60 min and preheated films at different hot plate temperatures.

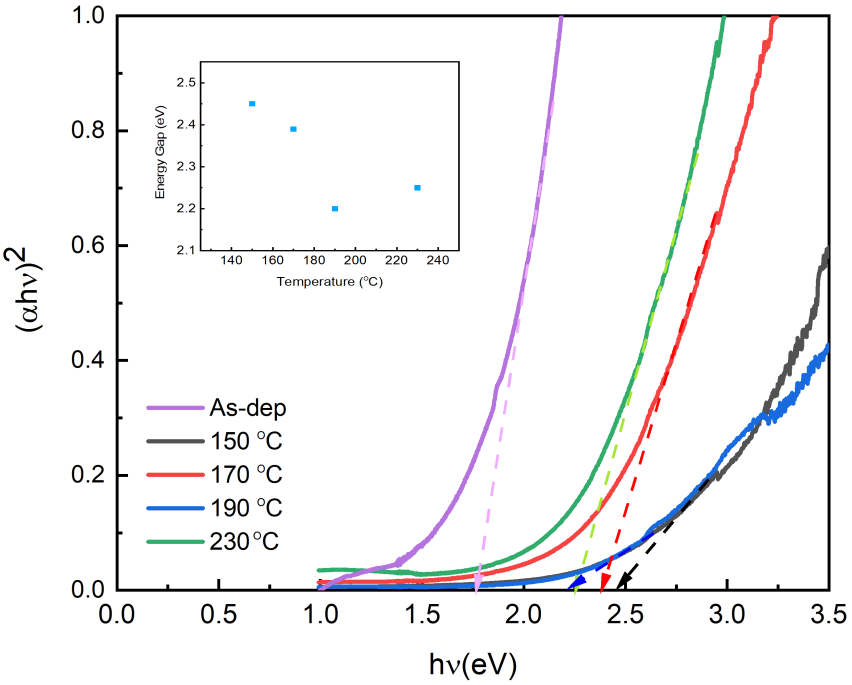

Figure 6.9: Plot of $(\alpha\ h\nu)^2$ vs photon energy at different preheating temperatures treated for 60 minuutes. The estimated energy gaps are shown in the inset.

6.9. Energy bandgaps for long preheating times are significantly larger in the range 2.2-2.5 eV. This is indicative of the formation of secondary phases with much larger bandgaps than CZTS, possibly ZnS or ZnO from annealing in air. Energy gaps increase as preheating temperatures rise, which could be attributed to the formation of secondary phases at long preheating times.

6.3 Effect of annealing on Cu_2ZnSnS_4 thin films

CZTS thin films were then annealed for one hour at various temperatures in a H_2S+N_2 atmosphere (sulphurisation). Sulphurisation of thin films promotes grain growth and controls the distribution of secondary phases. It is necessary to enhance the solar cell device performance [100]. Annealing (sulphurisation) has been carried out in the tubular furnace described in Chapter 4. Thin films were annealed

under H_2S+N_2 20:80 at temperatures of 450, 500, and 550 °C for one hour. Baid et al. [187] found that at high-temperature annealing of films, typically between 450 and 550 °C in an H_2S environment, reduced the amount of binary and ternary sulphide present, resulting in better device performance [187]. Chemical bath deposition, described in Chapter 4, was used to complete the CZTS/CdS heterojunction. Different studies on CZTS/CdS and CZTS/Mo interfaces aimed to achieve high-performance devices. Kauk et al. (2021) [185, 186] found that the high-performance devices' potential is demonstrated by the CZTS/CdS interface post-annealing. According to several studies, an efficient method to raise the quality of the interface is to anneal a CZTS/CdS sample in an alternative atmosphere such as air, vacuum, or inert gases. Cd and Zn diffusion lead to the formation of a thin layer of $CuCdZn_{1-x}SnS_4$ on the CZTS surface and a $Zn_{1-x}Cd_xS$ layer between the CZTS and CdS. These layers were proposed to change the cliff-like band alignment between the absorber and buffer layers to a spike-like band alignment [185, 186]. Sanchez et al. found that applying hotplate heat treatment to the solar cell structure will enhance the diffusion of cadmium from the n-type semiconductor to the absorber structure, increasing cell efficiency and improving J_{sc} and EQE. These modifications result from the partial replacement of Zn by Cd in the Cu_2ZnSnS_4 structure [188]. During high temperature annealing, sodium diffusion from soda lime glass (SLG) influences grain boundary formation and defect passivation in chalcogenide/kesterite solar cells [189]. Various characterisation techniques were carried out here to study the properties of CZTS thin films and heterojunctions.

6.3.1 Heterojunction fabrication

A molybdenum layer with a thickness of about 800 nm was deposited on the cleaned SLG by RF magnetron sputtering, as described in Chapter 4. The precursor solution CZTS was then deposited on the molybdenum-coated SLG (MSLG) substrates using spin coating at 2500 rpm for 30 seconds, followed by soft baking on a hot

plate at 150 °C, then 300 °C for 15 seconds, and the process was repeated several times to form the desired thickness of CZTS film. CZTS films were annealed at temperatures of 450, 500, and 550 °C, respectively, in H_2S+N_2 20:80. Finally, CdS layer was then deposited by chemical bath deposition, as described in Chapter 4.

6.3.1.1 Structure analysis

Figure 6.10 shows the XRD pattern of annealed samples at different annealing temperatures 450, 500, and 550 °C. The main peaks at 28.46°,33.3°, 47.35°, and 56.17°, which correspond to the (112), (200) (220), and (312) planes of the kesterite CZTS phase, In addition, week peaks were observed at 18.2°, 58.7°, 69.2,°and 76.4°and can be attributed to (101), (224), (008), and (332) planes of kesterite CZTS. These values are in agreement with ICDD 26-0575 [165, 166, 167].

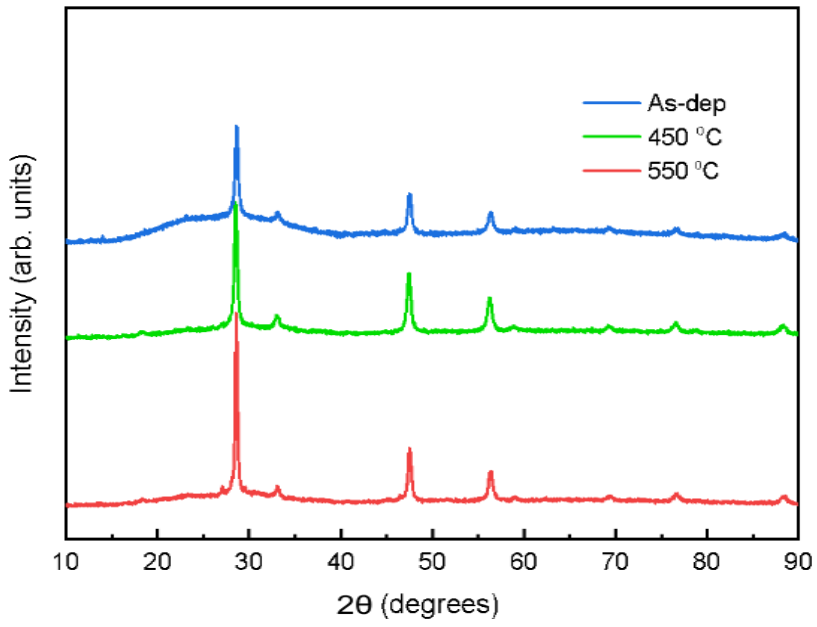

Figure 6.10: XRD patterns of the CZTS thin films annealed at different temperatures.

The major peaks in intensity become sharper because of the increasing annealing temperature. To further reveal or confirm the existence of secondary phases,

Raman spectroscopy was carried out, and the Raman spectra of as-deposited and annealed films are shown in Figure 6.11 with laser excitation wavelength 532 nm.

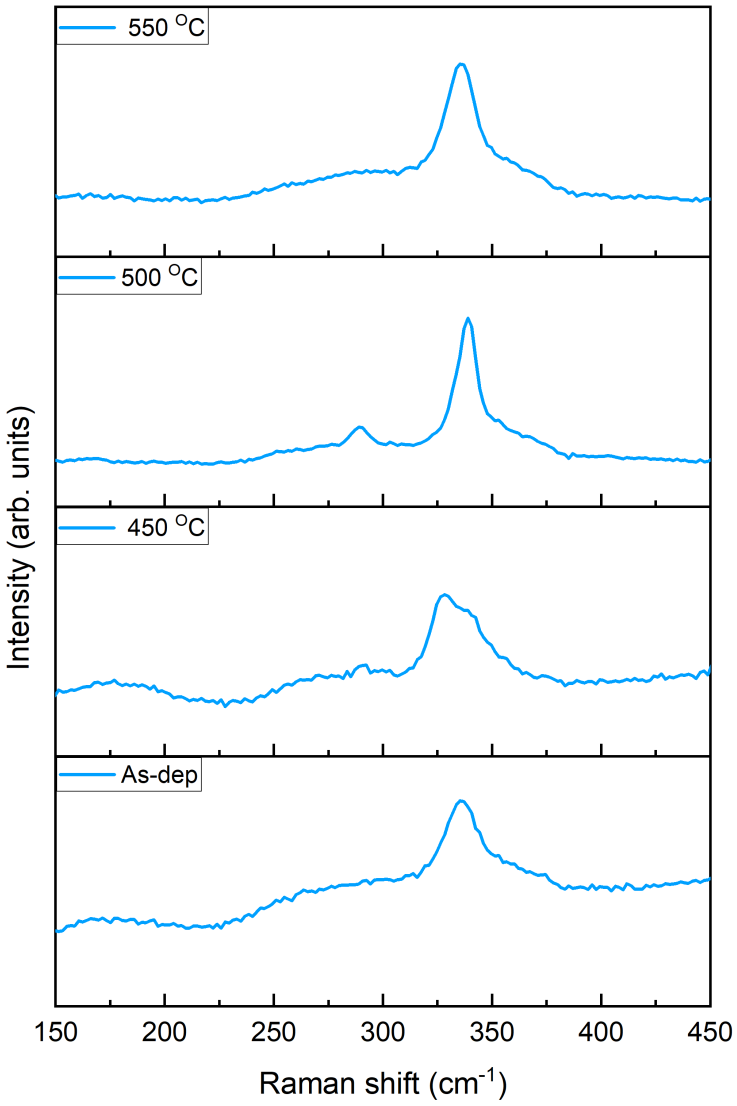

Figure 6.11: Raman spectra of annealed CZTS thin films at different annealing temperatures.

The Raman peaks become sharper upon annealing. From Lorentzian fitting in Figure 6.12, Raman peaks of CZTS and its secondary phases are given in Table 6.2. Raman spectra confirm the kesterite phase in all as-deposited and annealed samples, with its main peak located in the range of 336-338 cm^{-1} (mode A). In addition to other peaks that might be attributed to secondary phases such as ZnS at annealing temperature 450 °C and ZnS and SnS at annealing temperature 500

°C.

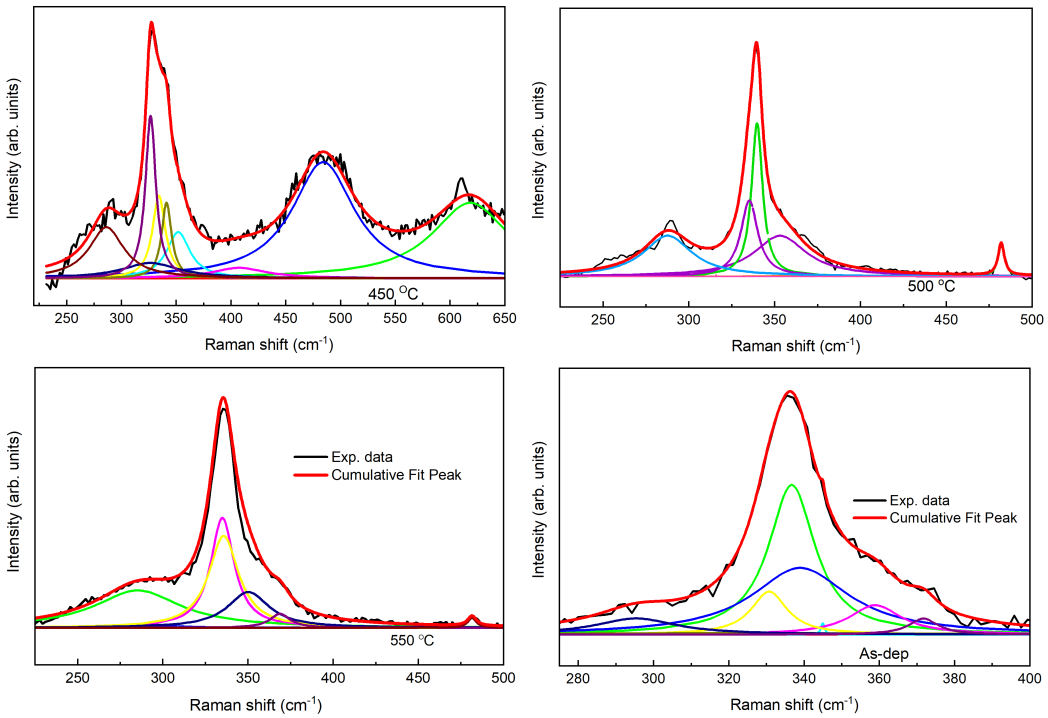

Figure 6.12: Raman spectra of CZTS as-deposited and annealed at different temperatures in a sulphur atmosphere; the spectra were fitted using Gaussian–Lorentzian shape components.

Table 6.2: The peaks identified in the Raman spectra of annealed samples at various temperatures.

Annealing Temperature	**Peak value (cm^{-1})**	**Phase**	**Symmetry**
As-dep	336	CZTS	A
	339	CZTS	A
	372	CZTS	A
	331	CZTS	disorder
450 °C	336	CZTS	A
	286	CZTS	A
	352	ZnS	-
	484	-	
500 °C	337	CZTS	A
	338	CZTS	A
	290	ZnS	-
	288	SnS	-
550 °C	300	CZTS	A
	336	CZTS	A
	319	CZTS	B
	255,	CZTS	E
	365	CZTS	E

6.3.1.2 Optical properties

Figure 6.13 shows the Tauc plot obtained from the absorption spectra of annealed CZTS films at different annealing temperatures (450, 500, and 550 °C). For annealing temperatures of 450, 500, and 550 °C, the energy gaps are 1.55, 1.40, and 1.30 eV, respectively. The enhanced absorption of the light assists efficient electron-hole charge separation and thus contributes to increasing solar cell performance.

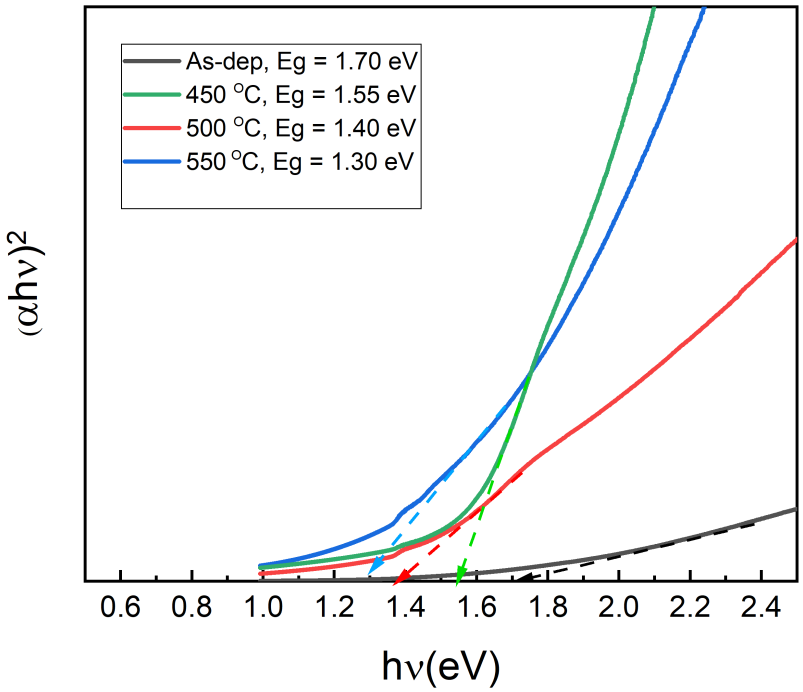

Figure 6.13: A Tauc plot based on the UV-Vis absorption spectra of the as-synthesized and annealed CZTS thin films at different temperatures, showing $(\alpha\ h\nu)^2$ vs. photon energy $(h\nu)$ to determine the energy band gap.

6.3.1.3 Electron microscopy morphology analysis

High-quality, defect-free CZTS(Se) films with fewer secondary phases and contaminants are needed to improve the performance of kesterite solar cells. To enhance the quality of the absorbing material, CZTS films are frequently post-annealed at high temperatures in an environment containing sulphur. The loss of volatile com-

ponents like tin or sulphur during high-temperature annealing might promote material decomposition [134]. In this section, we examine the effects of sulphurisation at various temperatures on the characteristics of CZTS and the Mo/CZTS/CdS heterojunction. Figure 6.14 depicts SEM top view and cross-sectional images of annealed film at 450 °C with compositional ratios Cu/(Zn+Sn) = 0.82, 0.51 before and after annealing.

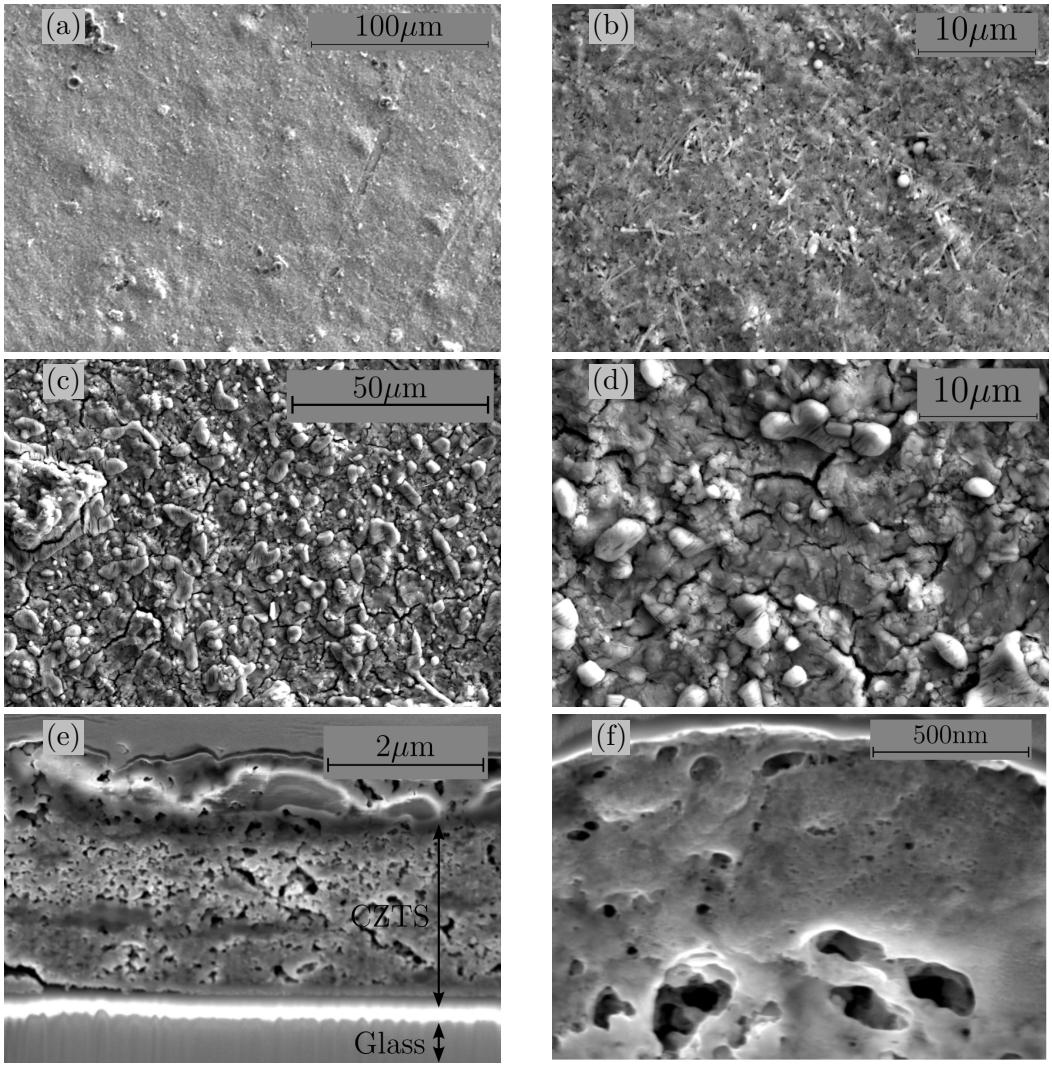

Figure 6.14: Top view images of as-deposited CZTS thin film deposited on glass substrate synthesised for 30 minutes at 225°C reaction temperature (a, b) and top view and cross section images of annealed film at 450°C for 1 hour under H_2S and N_2 pressure (20:80) (c-f), (e) and (f) at a magnification of 20k and 80k respectively.

6.3.1.4 Cross section element mapping

Figure 6.15 depicts a microscopy cross section of CZTS with a thickness of 1 micrometer that was annealed for one hour at 500 °C in H_2S and N_2 atmosphere (20:80). The figure shows uniform distribution of the constituent elements throughout the thickness of the CZTS absorber layer. It also shows significant diffusion of Na from the glass into the CZTS. The elements Si and O are most intense in the glass substrate as seen by the greater colour intensity. The other elements Mg, Al and Ca also show significant diffusion into the CZTS layer from the glass substrate.

To look at the properties of interfaces, heterojunction a Mo/CZTS/CdS layer structure was prepared. Figure 6.16 shows the cross-sectional images of a heterojunction (Mo / CZTS / CdS) where CZTS and Mo were annealed at 500 °C for one hour in H_2S+N_2 (20:80) atmosphere before CdS deposition. Images show a non homogeneous distribution of the constituent elements Cu, Zn Sn and S in the CZTS absorber layer. A thick, dense layer of CZTS, and at the top, an additional porous structure of CZTS is observed. This is identified as the CZTS floor layer with abnormal CZTS grains growing above the floor layer during the annealing process because of vapour transport to the surface during annealing [191, 192]. The copper in the CZTS layer is concentrated in the dense CZTS layer and also partly in the upper layer of CZTS. The higher Cu concentration in the upper left region of the image indicates growth of a phased with a different composition, possibly CuS. Zinc has a much more uniform distribution in all CZTS layers, with a higher concentration in the main CZTS layer. The tin concentration is higher in the main layer of CZTS. Sn diffuses toward the surface of the CZTS, leaving voids that might result in poor ohmic contact and shunting routes [134]. Uniform sulphur concentration is seen in the CZTS layer, higher (brighter) sulphur concentration in molybdenum layer, and less S in the CZTS which indicates the formation of a MoS_2 interface layer. Mo concentration is highest in the Mo layer with a small amount of residual Mo in the CZTS layer, confirming it is diffusing into the CZTS to form MoS_2.

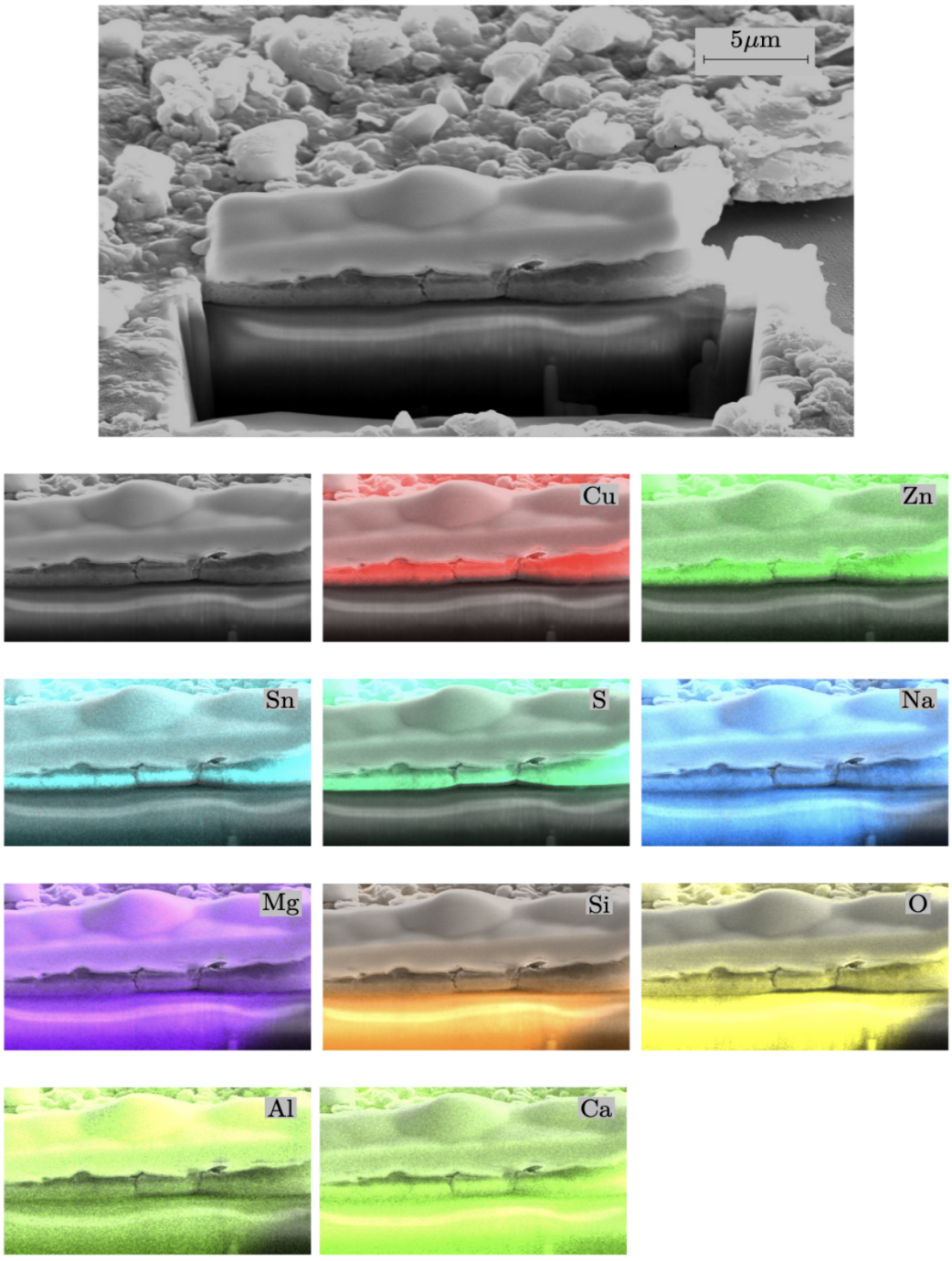

Figure 6.15: Elemental mapping of elements in CZTS/glass thin film cross section after annealing at 500 °C in a H_2S+N_2 (20:80) atmosphere (at a magnification of × 6.5k). Each element concentration profile is indicated as a different colour and overlayed on the original microscopy image. The greater intensity of colour indicates a higher element concentration.

A very thin conformal layer of CdS can be seen on top of CZTS, with additional Cd diffusing throughout the CZTS. Zn-rich and Cu-rich zones were also identified

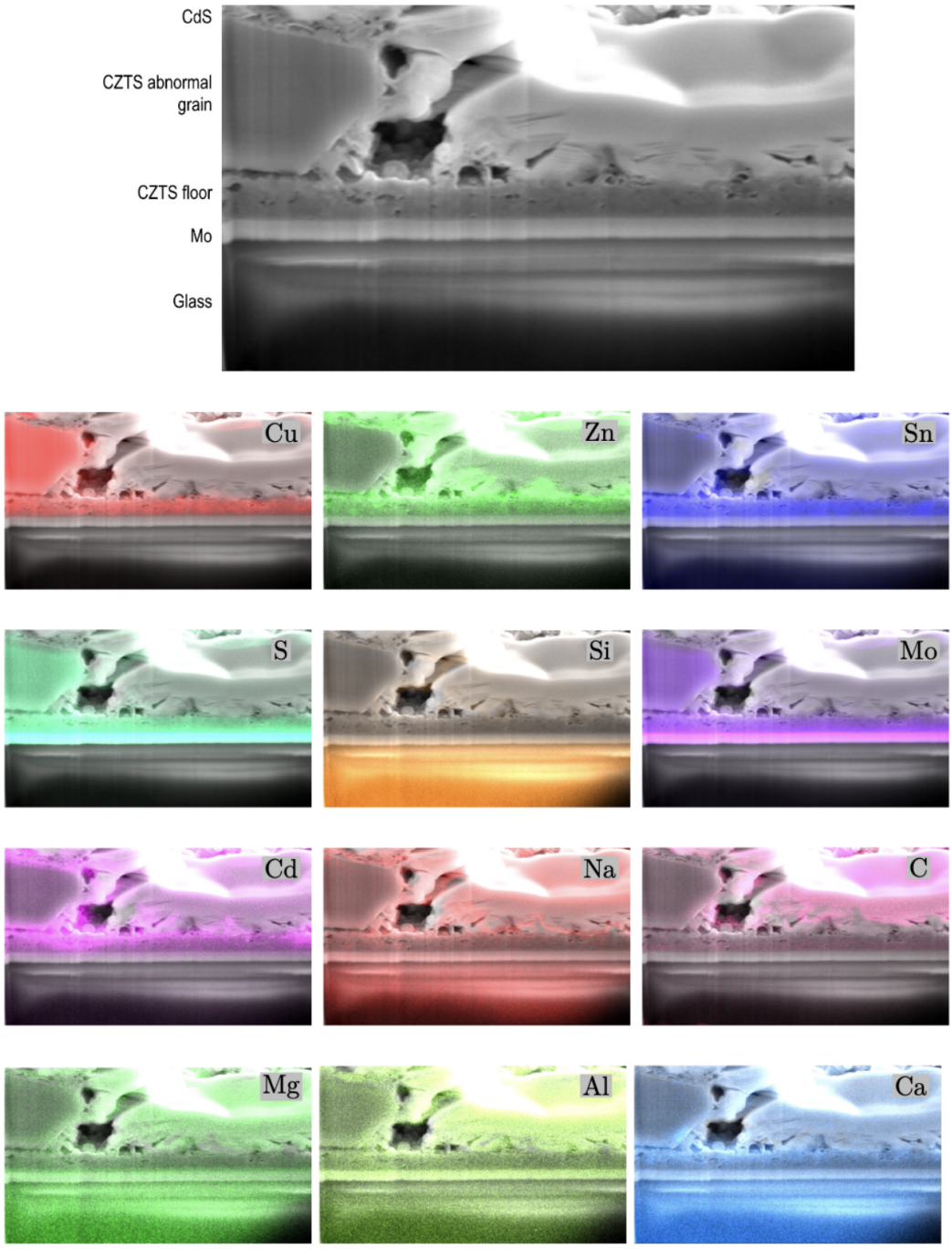

Figure 6.16: Elemental mapping of elements in the cross section of Mo/CZTS/CdS heterojunction films at annealing temperatures of 500 °C in a H_2S+N_2 (20:80) atmosphere, at a magnification of 8k. Each element concentration profile is indicated as a different colour and overlayed on the original microscopy image. The greater intensity of colour indicates a higher element concentration.

from the brighter regions by this mapping with the greatest variation of Zn and Cu concentrations in the abnormal CZTS grains above the floor layer. These

regional compositional irregularities can be attributed to a partial phase separation of Cu_2ZnSnS_4 into secondary phases (single or binary sulphides of Cu, Zn, or Sn) during annealing. Other elements, such as carbon, present in the precursor solution leave residues in the production of the CZTS thin film, thereby lowering the efficiency of the solar cell. In this structure, the main region of residual carbon is not in the main CZTS layer, but in the upper layer, indicating that carbon can diffuse through the entire CZTS layer. The main elements of glass such as silicon, calcium, magnesium, and aluminium diffuse into the CZTS and are farily uniformly distributed with the highest concentrations remaining in the glass. Cd diffusion was found to have a positive impact on the performance of thin-film solar cells [14, 15]. Xie et al. (2015) found that the presence of a Cu-related secondary phase is detrimental because it introduces shunting routes that lower the devices' FF due to its metallic nature and low resistivity profile. It has also been reported that the presence of a Zn-related secondary phase that forms at the Mo/CZTS interface reduces FF and increases R_s by limiting the conduction pathway of hole carriers towards the Mo back-contact.

Figure 6.17 shows the SEM surface image of an annealed film at 550 °C for one hour in H_2S and N_2 (20:80) and the EDX spectra of the CZTS films (site 1). The average composition ratio Cu/(Zn+Sn) = 1.28 and Zn/Sn = 0.39. A Cu rich area at the surface of the film is shown in Figure 6.17 (purple arrows). This corresponds to ceystas with different structure as seen in Figure 6.17(a) and (b). This is indicative of the formation of secondary phases. Scanning electron microscopy (SEM) images and associated energy dispersive spectroscopy (EDX) maps of the CZTS/CdS interface are shown in Figure 6.18. It illustrates the EDX elemental distribution profile of all the constituent elements throughout the thin film. This mapping also revealed the presence of Zn-rich and Cu-rich zones.in addition to diffusion of Cu and Zn in to glass substrate as shown in Figure 6.17. These local inhomogeneities in composition in some areas can be explained by a partial phase segregation of Cu_2ZnSnS_4 into secondary phases upon annealing. The images show

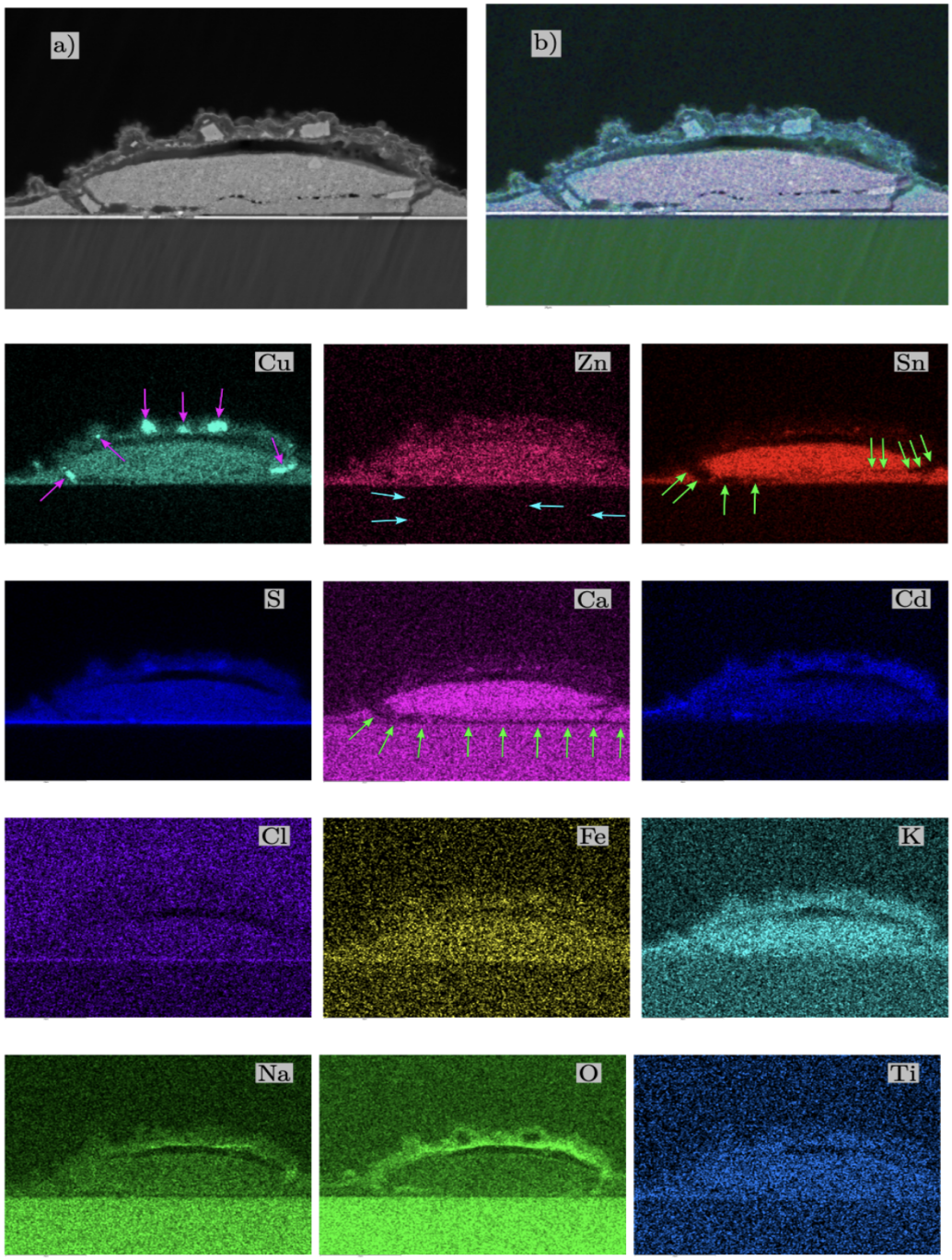

Figure 6.17: Elemental mapping of elements in a cross section of Mo/CZTS/CdS film at annealing temperature of 550 °C in H_2S and N_2 at a magnification of × 1.23k (Site 1).

a relative concentration of copper with more concentrated Cu at the top of the layer and excess sulphur (bright region) in the same upper region which may lead to CuS phase formation. The line profile in Figure 6.18 indicates that an increase in S and

Cu concentrations may result in the formation of the CuS phase. This corresponds to the bright cubic crystal in the top part of Figure 6.18, suggesting the presence of a crystal of CuS. Zinc is distributed much more uniformly in the CZTS layer. Sn is mostly concentrated in the CZTS layer, but loss of Sn in some areas was observed (green arrows) due to the relatively high vapout pressure of Sn at high annealing temperature. There is a uniform concentration of S in the CZTS layer and a higher concentration of sulphur in the molybdenum layer which is due to the formation of MoS_2, Mo diffusion into the CZTS layer, or both. A very thin layer of CdS can be seen on top of CZTS, with additional Cd diffusing throughout the CZTS layer. The main elements of glass are silicon, calcium, magnesium, and aluminium. The main concentration of silicon is observed in the glass, the calcium diffuses uniformly into the CZTS. Na, Mg, Al and Mo diffuse into the CZTS layer. The presence of a Cu-related secondary phase is undesirable because it introduces shunting routes that lower the devices' FF due to its metallic nature and low resistivity profile. It has also been reported that the presence of a Zn-related secondary phase that forms at the Mo/CZTS interface reduces FF and increases R_s by limiting the conduction pathway of hole carriers towards the Mo back-contact [134].

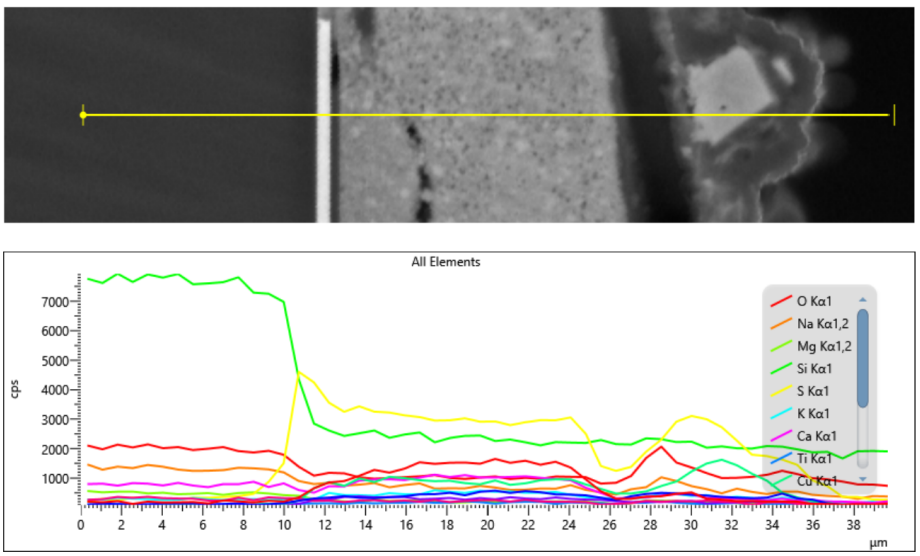

Figure 6.18: SEM surface image and EDX spectrum of deposited CZTS thin film annealed at 500 °C for one hour in H_2S and N_2 (20:80).

Figure 6.19 shows the elemental mapping of site 2, where the top layer of the CZTS film has large grains whereas the bottom layer has relatively small grains similar to that seen in Figure 6.16. Both CZTS layers are extremely dense, with no obvious voids. As a result of the annealing process, the film has a MoS_2 layer above the Mo substrate with a higher S concentration. Cu-rich regions are obserevd at the top of the CZTS layer. In contrast to CIGS, it has been established that the Mo thin film back contact on CZTS can have a negative effect on the performance of CZTS devices. In the presence of Mo, Cu_2ZnSnS_4 is unstable at high processing temperatures (500–600 °C). The decomposition of Cu_2ZnSnS_4 is explained by the following reaction:

$$2\,Cu_2\,Zn\,Sn\,S_4 \longleftrightarrow 2\,Cu_2\,S + 2\,Zn\,S + 2\,Sn\,S + 2\,S\,(g) \tag{6.1}$$

Mo combines with S at the CZTS/Mo interface to form MoS_2 via the reactions described below:

$$Mo + 2\,S \longrightarrow MoS_2 \tag{6.2}$$

The instability of the Mo back contact at the CZTS/Mo interface during thermal processing can be represented by combining the two reactions above.

$$2\,Cu_2\,Zn\,Sn\,S_4 + Mo \longrightarrow 2\,Cu_2\,S + 2\,Zn\,S + 2\,Sn\,S + MoS_2 \tag{6.3}$$

The instability of the Mo back contact has the potential to result in losses of V_{oc}, J_{sc}, and FF in the CZTS device [193].

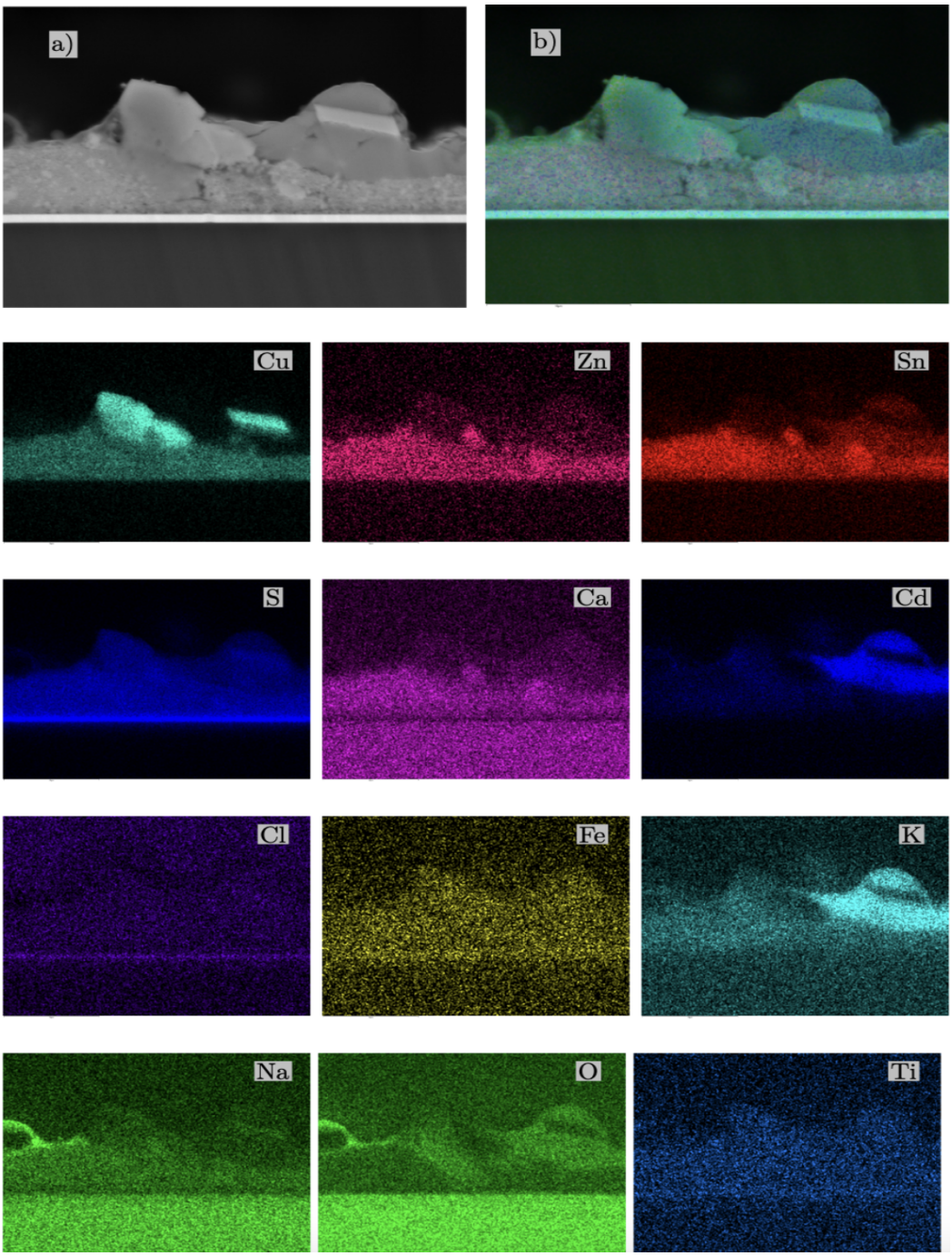

Figure 6.19: Elemental mapping of elements in a cross section of Mo/CZTS/CdS films at annealing temperature of 550 °C for one hour in a H_2S and N_2 at a magnification of × 3.19k (Site 2).

6.4 Summary

A study of the effect of preheat treatment using a hot plate under an air atmosphere on the properties of CZTS thin films has been presented. It was found that the thermal treatment parameters, temperature and time, affect the absorber bandgap and crystallite scattering domain size. A further study of the effect of high temperature annealing on a Mo/CZTS/CdS heterojunction was carried out at temperatures ranging from 450°C to 550°C at an annealing time of one hour in a H_2S+N_2 20:80 atmosphere in a tube furnace. Annealing promotes cadmium diffusion from the n-type semiconductor to the absorber. According to various studies, Cd diffusion improved the performance of thin-film solar cells. However, at annealing temperatures of 500 and 550 °C, the presence of a Cu-related secondary phase is detrimental because it introduces shunting routes that lower the devices' FF due to its metallic nature and low resistivity profile. In addition, in the presence of Mo, Cu_2ZnSnS_4 is unstable at high processing temperatures (500–600 °C). Mo combines with S to result in the decomposition of Cu_2ZnSnS_4 at the CZTS/Mo interface to form MoS_2 which leads to losses of V_{oc}, J_{sc}, and FF in CZTS devices.The findings presented here indicate that there is significant interdidffusion of the elements from the different layers in a Mo/CZTS/CdS heterojunction which occur at the temperatures commonly used to fabricate CZTS devices. Further improvements in CZTS devices will require strategies to control this interdiffusion.

Chapter 7

Structural, morphological and optical properties of Cu_2ZnSnS_4 thin films deposited by the drop-casting technique

In the present study, an investigation of the effects of the post-deposition annealing treatment on the morphological, structural, and optical properties of Cu_2ZnSnS_4 (CZTS) thin films deposited by the drop-casting technique is presented.Annealing at high temperatures in a sulphur atmosphere enhances grain growth, decreases the presence of surface defects and grain boundaries, improves the crystallinity of the film, and reduces secondary phases. Drop casting is a simple film-deposition technique that has been used by many research groups because it does not requires special equipment. the solution containing the required material is cast on a substrate. However, obtaining a homogeneous coating and controlling its thickness is difficult. The CZTS ink was synthesised by the hot-injection method as described in chapter 5 and deposited on a cleaned glass (SLG) substrate by drop casting. Films were then dried at 200 °C in a vacuum furnace for 10 min. Finally, all films were annealed at different annealing temperatures and times. This annealing was

carried out in a quartz tube furnace by introducing a mixed gas of H_2S and N_2 in a 20:80 ratio at a heating rate of 10 °C/min at various annealing temperatures (375, 400, 500, 550, and 575 °C) for one hour. Another set of samples was annealed at different annealing times (15, 30, 45, 60, and 75 min) at an annealing temperature of 550 °C. The films were characterized by X-ray diffraction (XRD), Raman spectroscopy, scanning electron microscopy (SEM, FIB), and UV-Vis-IR spectroscopy. Many researchers report the synthesis and deposition of CZTS thin films using the drop-casting method [194, 195, 196, 197, 198].

Figure 7.1 shows the SEM top views and cross-section images for thin film deposition with drop-casting of nanocrystal ink synthesised at reaction temperature 225 °C at reaction time 30 min. From the surface morphology shown in Fig. 7.1 (a, b), the film deposited by drop casting have large, densely packed grains with a lot of cracks. The cross-section images show Large agglomerated micro-grains are observed, as shown in figure7.1 (c, d).

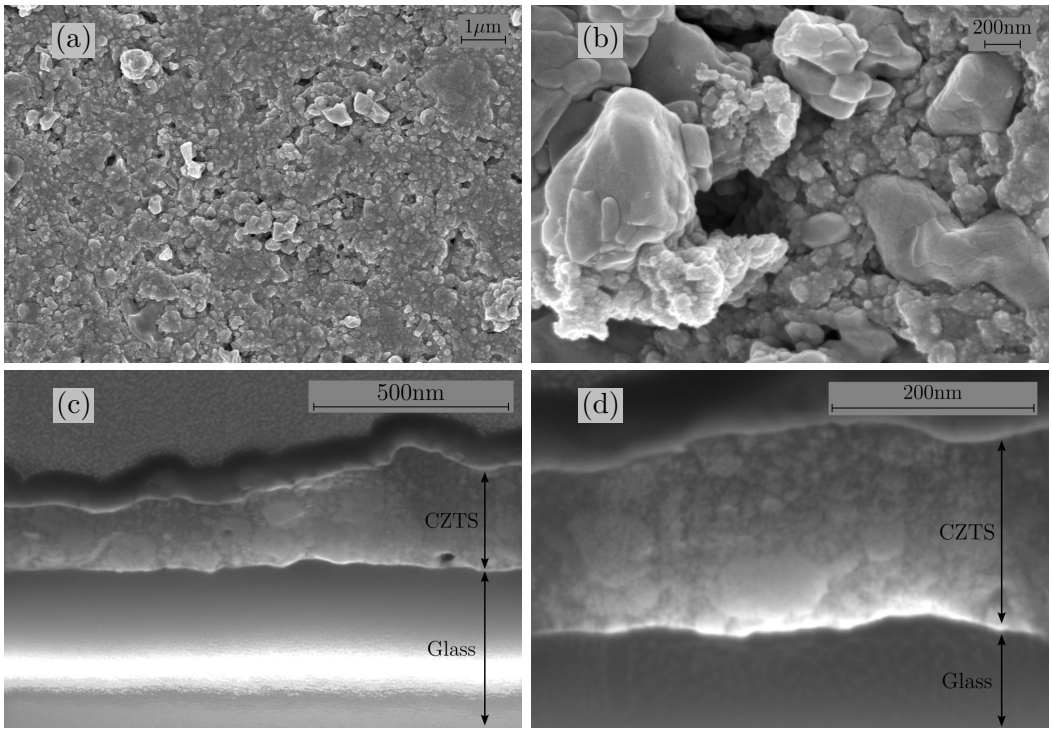

Figure 7.1: SEM top views (a, b) and cross-sectional images (c, d) of CZTS thin films deposited by drop-casting before annealing at different magnifications (10k, 40k, 100k, and 200k, respectively).

7.1 Effect of annealing temperature

7.1.1 Composition analysis

The chemical composition of annealed drop cast CZTS thin films was determined using EDX. Table 7.1 shows the composition of films annealed at different temperatures (375, 400, 550, and 575 °C) for one hour, along with the Cu/(Zn+Sn) and Zn/Sn ratios for CZTS thin films. As-deposited films are Cu-poor and Zn-rich, the ratio Cu/(Zn+Sn) was less than one. Many studies have found that the best solar cells performance have a copper-poor, zinc-rich region with ratios of (Cu/Zn+Sn) =0.79 to 0.85 and (Zn/Sn) =1.05 to 1.25 [199]. The composition ratios of the as-deposited ink samples Cu/(Zn+Sn) and (Zn/Sn) were chosen as 0.79 and 1.22, respectively from the initial precursor ratios for hot injection synthesis. After annealing, the atomic ratio of Cu/(Zn+Sn) decreased from 0.79 to 0.38 as shown in Table 7.1. The Zn/Sn ratio reduces from 1.22 to 0.88 for annealing up to 550 °C, then increases to 4.26 after annealing at 575 °C. Together these changes indicate a loss of Cu and an increase in the ratio of Zn and Sn with a further loss of Sn after annealing at 575 °C. This behaviour after annealing is different in drop cast films compared with that in spin-coated films, where the Cu loss is less prominent. A significant change in the composition and ratios is seen at the highest annealing temperature 575 °C where there is also a significant deacrease in the percentage of Sn from 34% to 11%, arising from the increased vapour pressure of Sn at higher temperatures.

Table 7.1: The composition of the CZTS thin films annealed for one hour at different annealing temperatures.

Annealing temperature (°C)	**S (At %)**	**Cu (At %)**	**Zn (At %)**	**Sn (At %)**	**Cu/(Zn+Sn)**	**Zn/Sn**
As-deposited	42.2±0.1	25.6±0.1	17.6±0.1	14.4±0.1	0.79±0.1	1.2±1.6
375	30.8±0.7	17.7±0.6	16.9±0.9	34.4±0.5	0.34±0.4	0.4±1.9
400	31.4±0.3	18.5±0.9	15.8±1.2	34.2±0.3	0.37±0.6	0.4±3.8
550	30.8±2.1	18.2±1.6	27.1±4.6	23.70±4.	0.3±0.2	0.8±1.3
575	32.8±0.1	7.4±0.9	48.3±1.1	11.3±0.4	0.1±0.5	4.2±2.7

7.1.2 Morphology characterisation

The surface morphology of all CZTS thin films was investigated using SEM secondary electron imaging. Figure 7.2 shows the plan-view SEM images of the CZTS thin films annealed for one hour at different annealing temperatures of 375, 400, 550, and 575 °C under H_2S+N_2 20:80 atmosphere. From the SEM images, the films annealed at the lower annealing temperature of 375 °C have a uniform surface with round bumps with small voids and cracks. Furthermore, samples annealed at higher temperatures 500 and 550 °C, revealed formation of abnormal grains, which might be related to secondary phases or incorporated components during the reaction process. According to the literature, each element has a vapour pressure, and at high annealing temperatures, elements with high vapour pressure, such as Cu and Zn, diffuse out of the films, which might lead to grain growth. The observation of abnormal grain growth on top of a fine-grained layer described by a previous study [118].

7.1.3 Crystal structure

7.1.3.1 X-ray diffraction

Figure 7.3 shows the XRD patterns of the CZTS thin films annealed at different annealing temperatures: 375, 400, 500, 550, and 575 °C at one-hour annealing time. All annealing temperatures show diffraction peaks around four major CZTS diffraction peaks: 28.35°, 33.23°, 47.5°, and 56.3°. These correspond to the (112), (200), (220), and (312) planes of kesterite CZTS which confirms formation of kesterite CZTS [199, 175, 176, 200]. The CZTS reference powder diffraction spectra PDF 026-0575 is shown in Figure 7.3 for comparison. The major peak intensities become sharper and stronger with increasing annealing temperature up to 500 °C. Table 7.2 shows estimated values for lattice constants a and c of the films calculated from the (112), (220), and (312) peaks and is in good agreement with theoretical

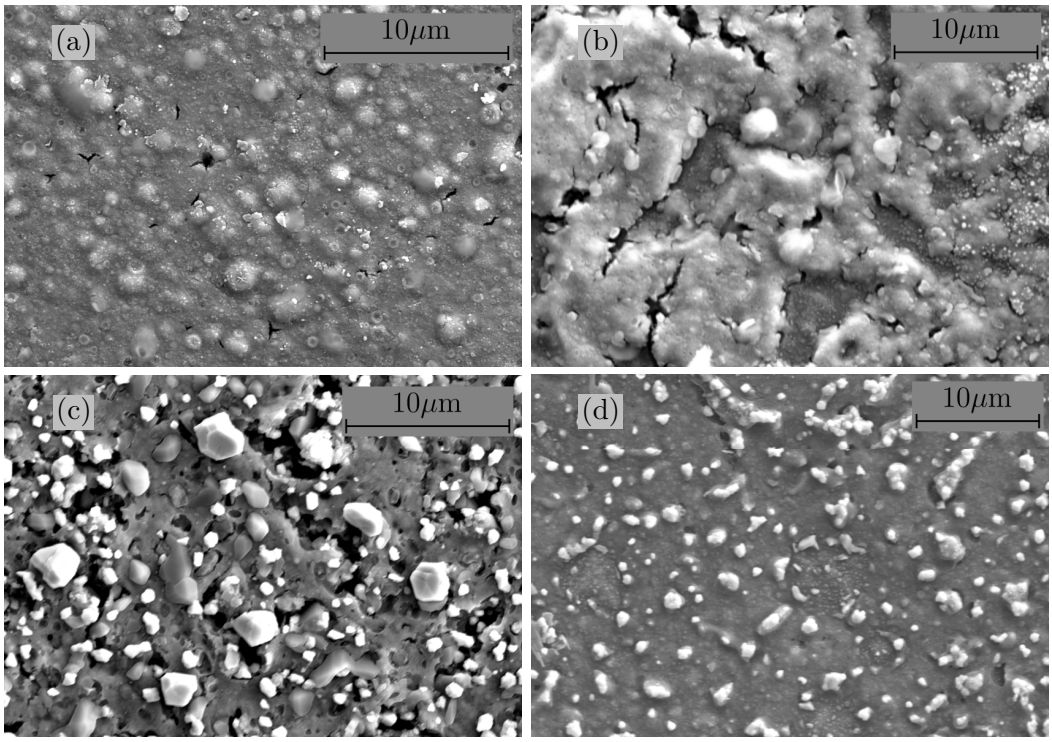

Figure 7.2: SEM images of a CZTS drop cast thin film deposited on a glass substrate and annealed for 1 hour under H_2S + N_2 20:80 pressure at temperatures of (a) 375, (b) 400, (c) 500, and (d) 550 °C

values [169, 170, 168, 165, 166, 177]. The (112) X-ray peak FWHM shown in Table **??**for different annealing temperatures was extracted from the the main (112) peak diffraction lines. FWHM peak widths generally decrease as annealing temperature increases for all annealing temperatures except 550 °C. The FWHM can be used to determine the X-ray scattering domain size and indicates the increasing crystalline nature of the films annealed at higher annealing temperatures. The scattering domain size was estimated using the Debye-Scherrer equation 4.2. The small grain size of CZTS can be confirmed by large FWHM values in XRD spectra in films that are observed to have larger grain boundary limitations which leads to larger pinholes and larger voids in the thin film, as can be seen in scanning electron microscopy (SEM) images for annealing temperatures of 375 and 400 °C. The scattering domain size increases with annealing temperature, as shown in Table 7.2, demonstrating enhanced crystallinity with increasing annealing. These results demonstrate that annealing has a significant influence on crystallinity.

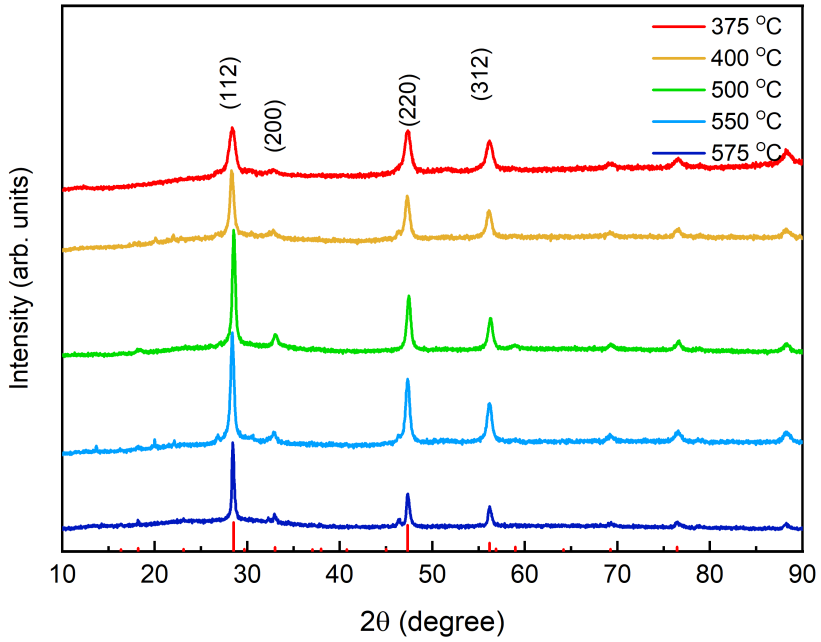

Figure 7.3: XRD patterns of annealed CZTS thin films at various temperatures for 1 hour. A reference pattern from the ICDD database for kesterite Cu_2ZnSnS_4 (PDF 00-026-0575) is shown in the red stickplot.

Table 7.2: XRD lattice parameter, FWHM of (112) diffraction peak, and scatttering domain of as-deposited CZTS thin films and after annealing at different temperatures for one hour.

Annealing temperature (°C)	**Lattice parameter**		**FWHM (degree) peak (112)**	**Scattering domain (nm)**
	Peak intensity (112)	a **(nm)** c **(nm)**		
375	1466	0.5432 1.0958	0.76	10.78
400	2391	0.5435 1.0909	0.60	13.65
500	4306	0.5417 1.0833	0.47	17.43
550	3993	0.5431 1.0975	0.52	15.75
575	2860	0.5404 1.1031	0.38	24.09

7.1.3.2 Raman spectroscopy

The existence of secondary phases can influence the performance of devices because these secondary phases can induce differences in the band alignment or a mismatch in the crystal structure leading to higher recombination losses. Raman spectroscopy was used to detect the presence of secondary phases. Secondary phases such as ZnS, SnS, and Cu_2SnS_3 have similar XRD pattern structures to the kesterite CZTS phase. Therefore, it's difficult to distinguish these secondary phases using the XRD

technique. However, Raman spectroscopy is used as a complementary technique to distinguish between them [201, 202, 203, 204, 7, 15, 163]. A 532 nm laser excitation wavelength was used to excite the Raman spectra at room temperature. The Raman spectra of CZTS films annealed at different temperatures are shown in Figure 7.4 which shows the fitting with Lorentzian functions curves of the Raman spectrum, that can determine the Raman peak position for each mode.

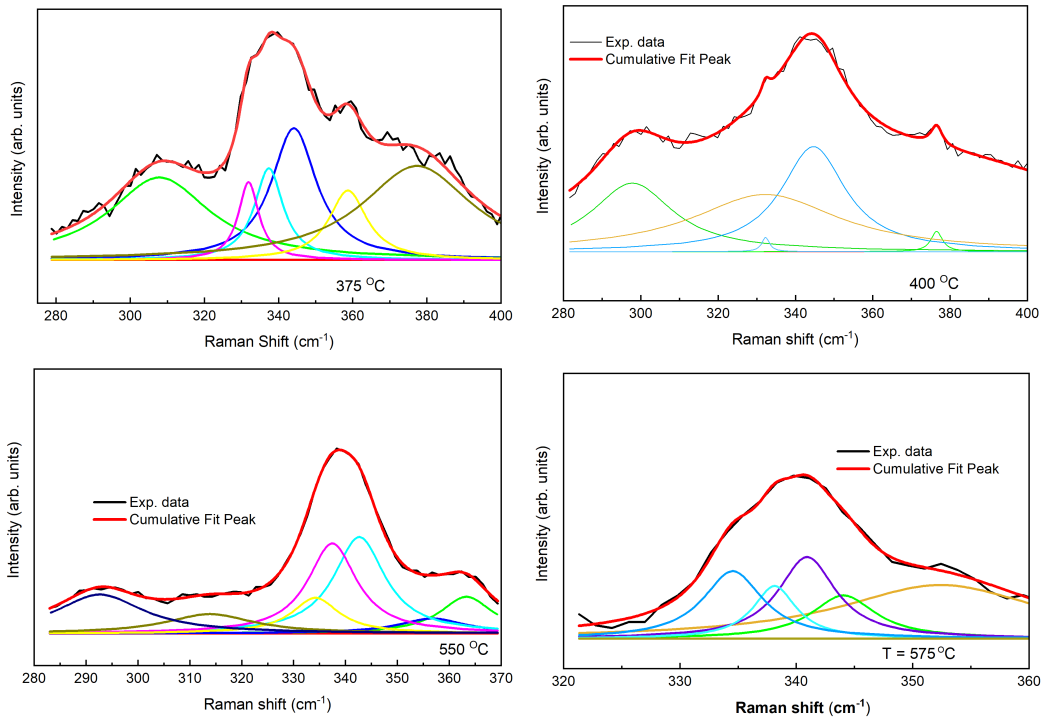

Figure 7.4: The fitting with Lorentzian functions curves of the Raman spectrum with different annealing temperatures for one hour.

All Raman spectra of all films are dominated by a strong peak at 337, 332, 334 and 334 cm^{-1} for annealing temperatures of 375, 400, 550 and 575 °C, respectively. Raman peaks become sharper with stronger intensity at 500 °C and 550 °C, and lower intensity at lower annealing temperature of 400 °C compared to as-deposited film. Individual plots of deconvoluted Raman spectra of CZTS thin films with Lorentzian peak fitting function for different annealing temperatures show that samples annealed at temperature 550 °C, show the presence of the secondary phase SnS_2 with peak Raman positions at 314 cm^{-1} [205] and 356 cm^{-1}. Fitting at 375

°C indicates the existence of the Sn_2S_3 phase with a Raman peak at 307 cm^{-1} [205]. The more sensitive nature of Raman spectroscopy allows the observation of secondary phases at levels which would not appear in X-ray diffraction spectra.

7.1.4 Optical characterisation

The energy band gap is estimated using the Tauc Plot of $(\alpha h\nu)^2$ versus photon energy $(h\nu)$ as shown in Figure 7.5. A variation is observed in the energy gap because of the variation in annealing temperatures. The increase in optical band gap at annealing temperature 575°C might be attributed to the decrease in atomic ratio Cu/(Zn+Sn) for the annealed films from 0.79 to 0.26 as reported by Feng et al. [20]. The film annealed at 575 °C has an estimated optical band gap of 1.5 eV, which is close to the optimum band gap range for solar energy conversion [7, 178].

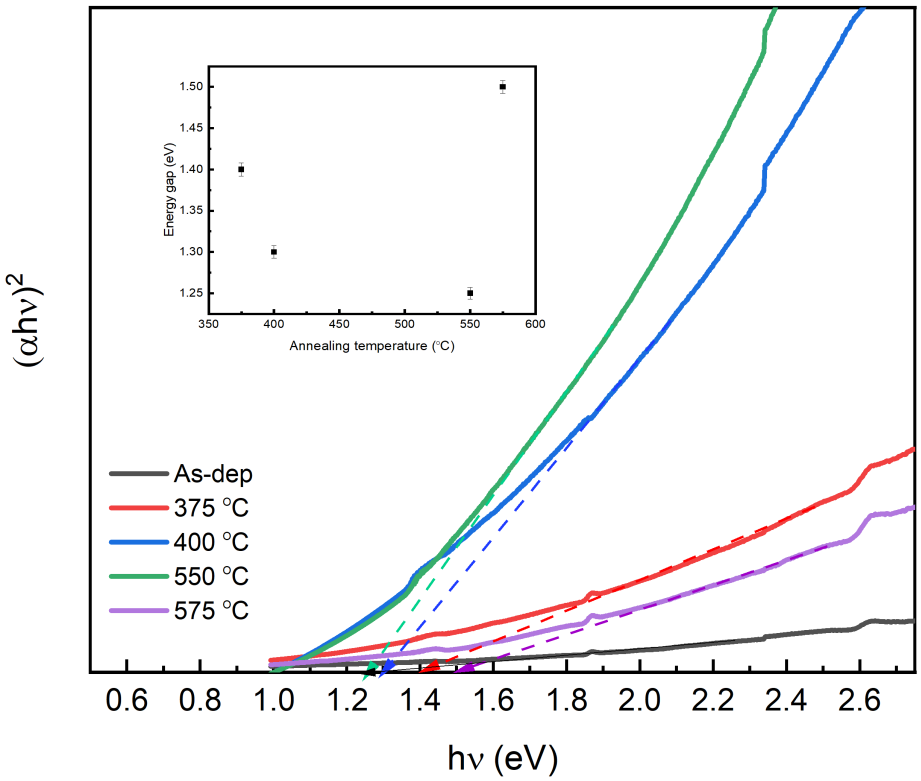

Figure 7.5: Tauc Plot of $(\alpha h\nu)^2$ versus photon energy $(h\nu)$ for CZTS for annealed samples at different temperatures for 1 h. The inset shows the variation of energy band gap with annealing temperature.

7.2 Influence of annealing time

7.2.1 Composition analysis

Table 7.3 shows the chemical compositions of CZTS films annealed at 550 °C for different annealing times of 15 min, 30 min, 45 min, 60 min, and 75 min. All annealed films were observed to be Cu-poor and Zn-rich compositions after annealing. The Cu/(Zn+Sn) ratio shows a decreasing trend with increasing annealing time, whereas the Zn/Sn ratio shows a general increasing trend with annealing time.

Table 7.3: CZTS thin film compositions at annealing temperatures of 550 °C and different annealing times.

Annealing time (min)	**S (At %)**	**Cu (At %)**	**Zn (At %)**	**Sn (At %)**	**Cu/(Zn+Sn)**	**Zn/Sn**
As-dep	42.2	27.8	24.1	5.7	0.93	4.17
15	27.9	18.2	17.3	15.2	0.55	1.14
30	31.0	28.0	31.0	10.0	0.68	3.10
45	50.4	13.7	29.6	6.1	0.38	4.80
60	31.3	33.1	29.5	5.9	0.93	4.94
75	30.6	19.9	37.7	11.9	0.40	3.16

7.2.2 Morphology characterisation

Figure 7.6 shows the plan-view SEM images of the CZTS thin films annealed at 550 °C with different annealing times of 30, 45 and 75 min. The film annealed for 30 and 45 min appears uniform, with small voids and cracks. At a higher annealing time of 75 min, as shown in Figure 7.7, a fine grained floor layer emerges (labelled by red stars) with larger abnormal grains (labelled by blue stars) appearing on the surface. grain growth on the surface could be attributed to ZnS. EDX measurements show that the surface grains are richer in Zn and poorer in Cu compared to the floor layer.

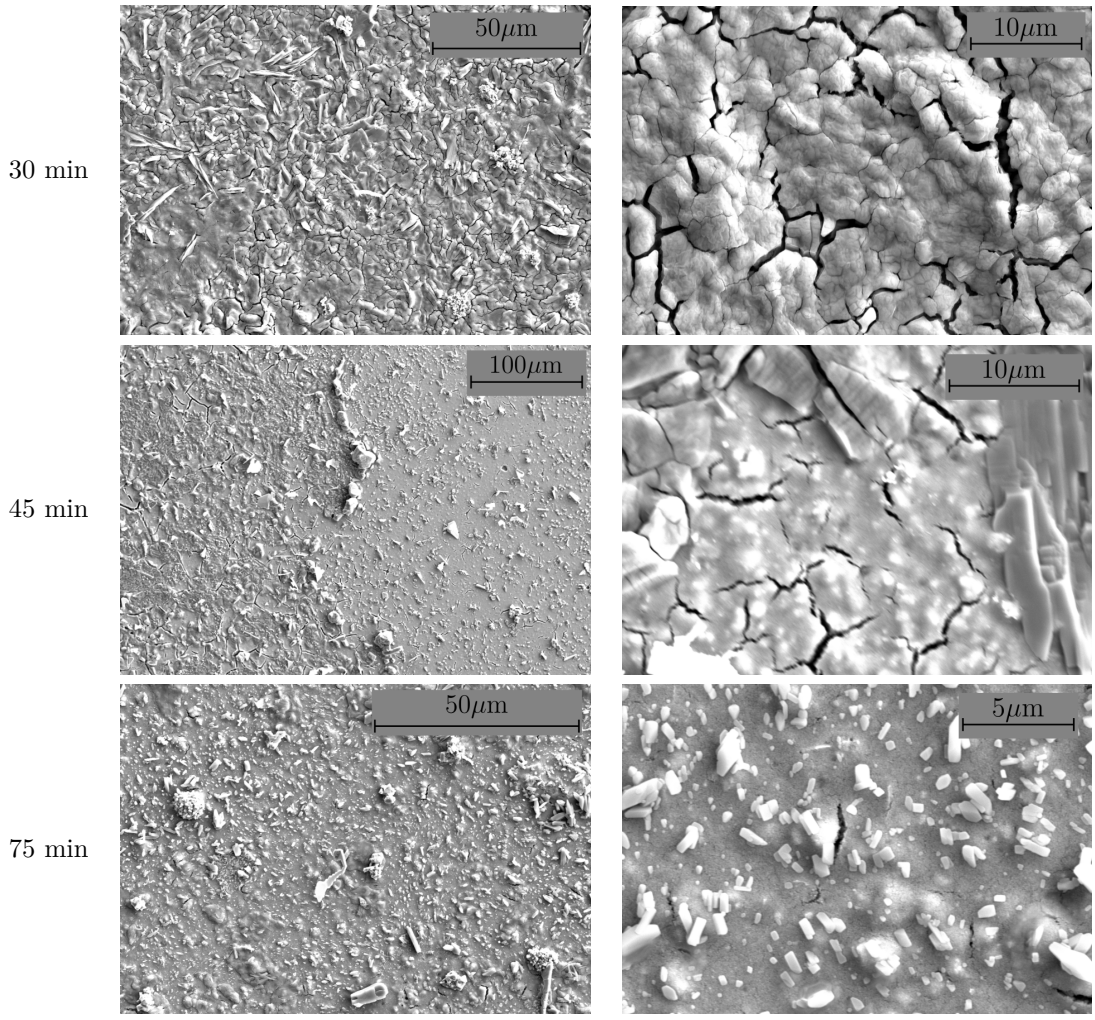

Figure 7.6: Top view SEM images of a CZTS thin film deposited on a glass substrate and annealed at 550 °C for (a) 30, (b) 45, and (c) 75 minutes.

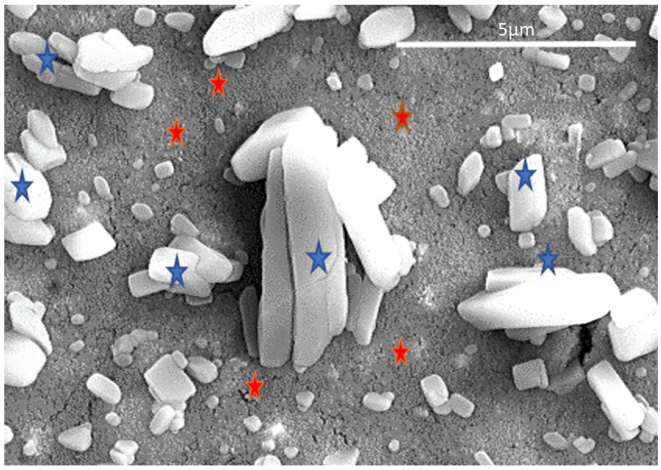

Figure 7.7: SEM image of the film annealed at 550 °C for 75 min. The floor layer with red stars and large grains is indicated by blue stars (magnification of ×1k).

7.2.3 Crystal Structure

7.2.3.1 X-ray diffraction

Figure 7.8 shows the XRD spectra of the CZTS thin films annealed at 550 °C at different annealing times. All three major peaks occur at 28.3°, 47.1°, and 56.3°, which correspond to (112), (220), and (312) planes of kesterite CZTS, and these values are in good agreement with the ICDD-260575 reference spectra [199]. The major peak intensities become sharper and stronger as the annealing time increases, except for the longest time of 75 min, where it decreases as shown in Figure 7.8. Additional small peaks appear at 13.6°, 18.1°, 19.9°, 22.1°, 26.8°, 30.6°, and 58.9° after 45 minutes of annealing. After one hour of annealing, a lot of these peaks disappear, but other peaks start to increase in intensity, and at an annealing time of 75 min, some disappear, such as the peaks at 13.6°and 26.8°. Table 7.4 shows the estimated values of CZTS lattice parameters a and c, and is in good agreement with reported values [169, 168, 171]. The X-ray scattering domain size increases with increasing annealing time except for 75 min, as shown in Table 7.4.

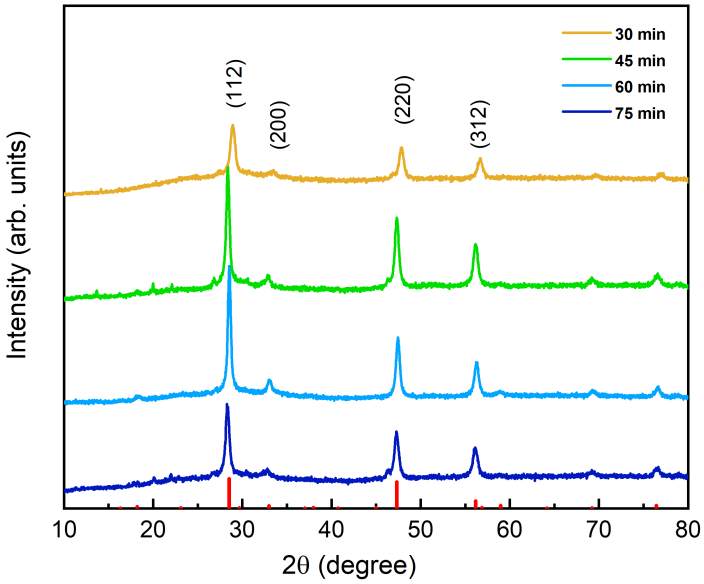

Figure 7.8: XRD pattern of CZTS thin films annealed at 550 °C for various annealing times. The ICDD-260575 reference spectra is shown in the red stick plot.

Table 7.4: Lattice parameters, FWHM, and scattering domain size of CZTS thin films as-deposited and annealed at 550 °C for various annealing times.

Annealing time (min)	**X-ray peak intensity (112)**	**Lattice parameter** a **(nm)** c **(nm)**	**FWHM (degree) Peak (112)**	**Scattering domain (nm)**
As deposited	4156	0.5413 1.078	0.49	16.72
30	1534	0.5375 1.065	0.80	10.24
45	3869	0.5425 1.094	0.51	16.06
60	2860	0.5404 1.103	0.38	21.56
75	2300	0.5422 1.092	0.51	16.06

7.2.3.2 Raman spectroscopy

The Raman spectra of CZTS films annealed for different annealing times are shown in Figure 7.9. It shows the broad peaks are deconvoluted with several possible peaks of different vibrational modes. The fitting with Lorentzian function curves of the Raman spectrum gives evidence that in all spectra the main peak is around (334, 336, 337, and 338 cm^{-1}) for annealing times of 30, 45, 60, and 75 min and is in agreement with reported values [15, 12, 206]. In addition, other Raman shifts, 346, 336 cm^{-1} (45 min), 349 cm^{-1} (60 min), 347, 321, 313 cm^{-1} (75 min), and 345, 313 cm^{-1} (30 min), correspond to different vibrational symmetry modes of CZTS. Moreover, there is evidence of the existence of different secondary phases

such as SnS_2, ZnS and $Cu_4Sn_7S_{16}$ as shown in Table 7.5. At an annealing time of 75 min, the existence of ZnS is shown in agreement with EDX measurement where an increase of Zn atomic percent is observed.

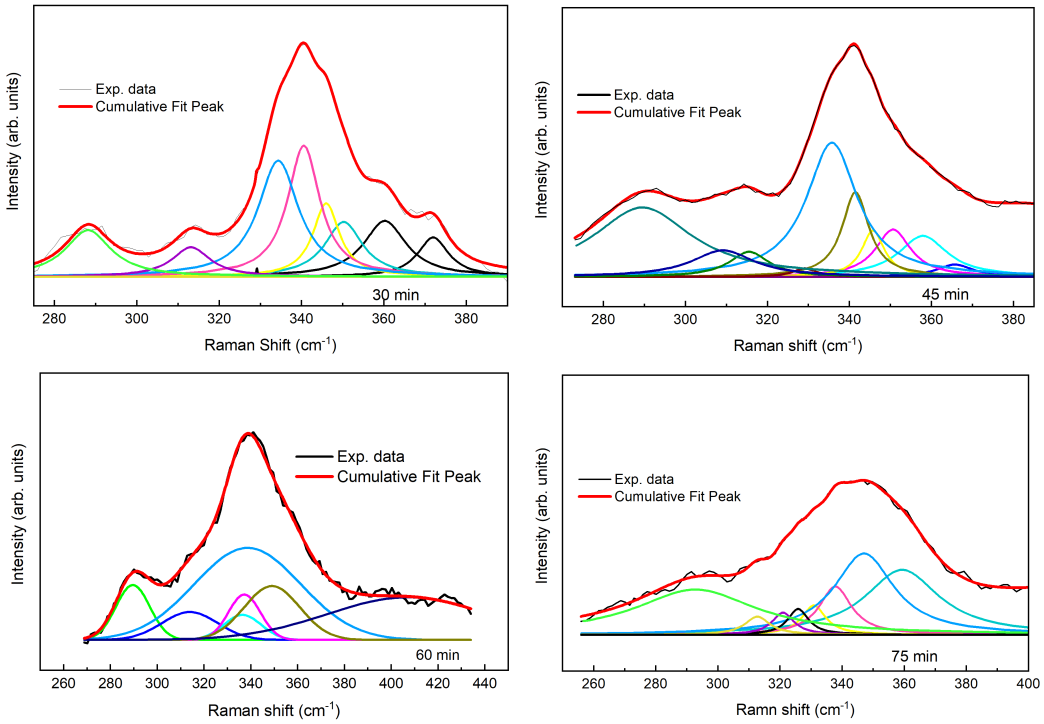

Figure 7.9: The fitting with Lorentzian function curves of the Raman spectra for CZTS samples annealed at 550 °C at different annealing times.

Table 7.5: Phase analysis of the measured spectra at different annealing times.

Annealing time (min)	**Phases**	**Raman Shift (Present work (cm^{-1})**	**Reported Raman Shift (cm^{-1})**
30	SnS_2	315	[207]
	ZnS, $Cu_4Sn_7S_{16}$	350	[208]
45	SnS_2	314	[207, 164]
	ZnS, $Cu_4Sn_7S_{16}$	290, 350	[209]
60	ZnS	290	[209]
	$Cu_4Sn_7S_{16}$	350	[209]
75	ZnS	313, 351	[200, 207, 164, 172]

7.2.4 Optical characterisation

Figure 7.10 shows the Tauc Plot of $(\alpha h\nu)^2$ versus photon energy $(h\nu)$ for annealed CZTS films at 550 °C at various annealing times. The extrapolation to determine

the energy band gap is shown for each film. The band gap increases with increasing annealing time. The energy gap is 1.16, 1.25, and 1.3 eV for annealing times of 30, 60, and 75 min, respectively. The increase in CZTS band gap energy could be explained by a decrease in the Cu/(Zn+Sn) ratio as shown in Table 7.3, as reported by a previous study [180].

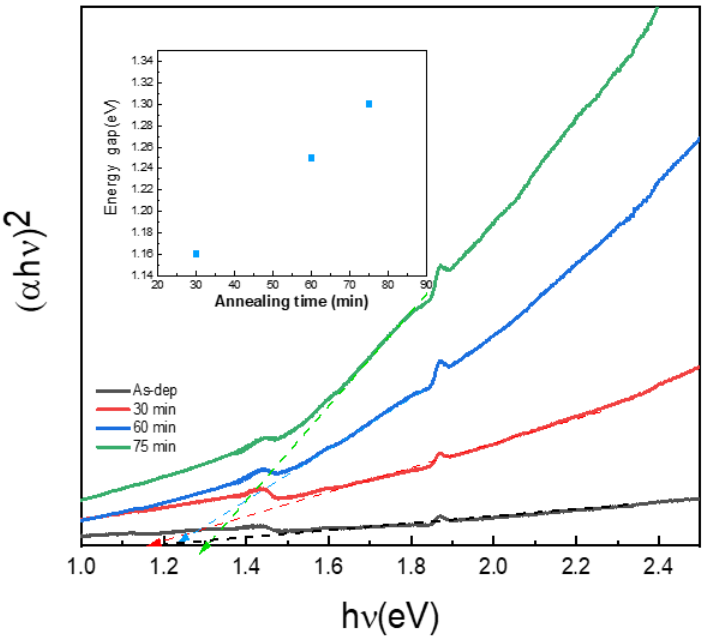

Figure 7.10: Tauc Plot of $(\alpha h\nu)^2$ versus photon energy $(h\nu)$ for as-deposited and annealed CZTS thin films at 550 °C for different annealing times. The inset shows the energy band gap as a function of annealing time.

7.3 Summary

A study on the effect of annealing parameters temperature and time on the compositional, morphologycal, crystal, and optical properties of the CZTS thin films deposited on SLG substrate by drop casting were investigated. All films were annealed in a H_2S+N_2 (20:80) atmosphere at different annealing temperatures (375, 400, 500, 550, and 575 °C) for one hour and different annealing times (15, 30, 45, 60, and 75 min) at annealing temperature 550 °C. A significant change in the composition and ratios is seen at the highest annealing temperature of 575 °C, where

there is also a significant decrease in the percentage of Sn . Morphology analysis shows films annealed at 550–575 °C show abnormal grain growth on the surface, as has been observed in previous studies. Crystal structure analysis shows that the small grain size of CZTS can be confirmed by the large FWHM values in XRD spectra of films that are observed to have larger grain boundary limitations, which leads to larger pinholes and larger voids in the thin film, as can be seen in scanning electron microscopy (SEM) images for annealing temperatures of 375 and 400 °C. The scattering domain size increases with annealing temperature, demonstrating enhanced crystallinity with increasing annealing temperature. All annealed films were observed to have Cu-poor and Zn-rich compositions after annealing. The Cu/(Zn+Sn) ratio decreases with increasing annealing temperature, whereas the Zn/Sn ratio increases with increasing annealing temperature. At a higher annealing time of 75 minutes, a fine grained floor layer emerges with larger abnormal grains appearing on the surface. An abnormal grain growth on the surface could be attributed to ZnS. EDX measurements show that the surface grains are richer in Zn and poorer in Cu compared to the floor layer. The analysis of crystal structure reveals that, except for 75 minutes, the annealing time increases the size of the X-ray scattering domain.

Chapter 8

Conclusions

8.1 Thesis summary

The purpose of the investigation presented in this thesis was to learn more about the properties of CZTS in order to improve its use as a solar photovoltaic absorber layer in a thin-film solar cell. CZTS is a promising quaternary semiconductor material to use as an absorber material for future generations of thin-film solar cells due to its less toxic nature, relative earth abundance of the constituent elements, excellent band gap, and high absorption coefficient.

The hot injection method was used to successfully synthesize CZTS nanoparticles. Inks were coated onto clean glass substrates using spin coating procedures at a speed of 2500 rpm for 15 seconds after being synthesized at 225 °C for 30 minutes via the facile hot injection process. A CZTS nanoparticle-based control sample that was synthesized at 225 °C for 30 minutes had a kesterite crystal structure. The average composition of the CZTS nanoparticles was determined by adjusting the precursor molar ratios into a Cu-poor and Zn-rich region of the phase diagram. The XRD pattern shows three main peaks of the kesterite structure were found confirming the crystal lattice structure as kesterite. The major XRD diffraction peaks appeared at 28.5°, 47.5°, and 56.3° and can be attributed to the (112), (220), and (312) planes of kesterite CZTS. The lattice parameters have been obtained

from the XRD pattern: $a = 5.413$ Å and $c = 10.788$ Å. The nanocrystal crystallite scattering domain size was found to be 15.39 nm. Optical spectroscopy analysis shows that the estimated energy bandgap is 1.50 eV. Investigations were done into how fabrication parameters like temperature and time affected the properties of CZTS thin films. It was revealed that band gap, composition, and crystal structure are significantly influenced by the post deposition annealing temperature (175, 185, 220, 225, 235, and 250 °C) and time (30, 45, and 60 min). The above-mentioned results analysis confirms that CZTS nanocrystals were successfully synthesised. The optimal temperature for synthesising a high quality CZTS absorber layer is 225 °C for 30 minutes, this results in an energy band gap and scattering domain size approximately 1.39 eV and 26.54 nm respectively. Due to its suitable band gap, and scattering domain size, CZTS nanoparticle ink has shown potential for application as the absorber layer in PV systems.

A study of the effect of annealing in a H_2S+N_2 atmosphere on the properties of CZTS thin films has been presented. The effect of annealing temperature on a Mo/CZTS/CdS heterojunction was carried out at temperatures ranging from 450 °C to 550 °C at an annealing time of one hour in a H_2S+N_2 20:80 atmosphere in a quartz tube furnace. There is significant interdiffusion of the elements from the different layers in a Mo/CZTS/CdS heterojunction which occur at the temperatures commonly used to fabricate CZTS devices. Annealing promotes cadmium diffusion from the n-type semiconductor to the p-type CZTS absorber layer. According to various studies, Cd diffusion improved the performance of thin-film solar cells. However, at annealing temperatures of 500 and 550 °C, the presence of a Cu-related secondary phase is detrimental because it introduces shunting routes that lower the devices' FF due to its metallic nature and low resistivity profile. In addition, in the presence of Mo, Cu_2ZnSnS_4 is unstable at high processing temperatures (500–600 °C). Mo combines with S to result in the decomposition of Cu_2ZnSnS_4 at the CZTS/Mo interface to form MoS_2 which leads to losses of V_{oc}, J_{sc}, and FF in CZTS devices. The findings presented here indicate that there is significant interdiffusion

of the elements from the different layers in a Mo/CZTS/CdS heterojunction which occur at the temperatures commonly used to fabricate CZTS devices. This diffusion over a period of time lead to degradation of the device. Further improvements in CZTS devices will require strategies to minimise this interdiffusion of these elements.

A study of different annealing parameters (temperatures and times) on the properties of the Cu_2ZnSnS_4 film deposited on glass by drop casting has been presented. All films were annealed at different temperatures and times. Different annealing temperatures (375, 400, 500, 550, and 575 °C) and different annealing times (15, 30, 45, 60, and 75 min) were investigated. All annealed films were observed to have Cu-poor and Zn-rich compositions after annealing. The Cu/(Zn+Sn) ratio shows a decreasing trend with increasing annealing temperature, whereas the Zn/Sn ratio shows a general increasing trend with annealing temperature. At a higher annealing time of 75 min a fine grained floor layer emerges with larger abnormal grains appearing on the surface. An abnormal grain growth on the surface could be attributed to ZnS. EDX measurements show that the surface grains are richer in Zn and poorer in Cu. The analysis of crystal structure reveals the X-ray scattering domain size increases with increasing annealing time except for 75 min.

8.2 Suggestions for further work

In addition to the work that is described in this thesis, there are a number of research challenges that still need to be addressed, Low efficiency is largely attributable to the interface problem. Additional research is necessary in order to improve performance of CZTS solar cells. Further research will be to develop a practical technique for reducing interface recombination of CZTS and eliminate the existence of secondary phases. More focus should be placed on the characteristics of the interface between the absorber layer and the rear contact. Further research is needed to fully understand the interface reactions between the Mo/CZTS and

CZTS/CdS layers. More emphasis is necessary to understand the interdiffusion of the elements and how they affect the performance of CZTS devices. More investigations of the sulphurisation process are required to minimise any interdiffusion of the elements or secondary phases. The preparation of complete photovoltaic devices will be important for studying the impacts on solar cell performance.

Bibliography

[1] Sachin R Rondiya, Yogesh A Jadhav, Aleksandar Živković, Sagar B Jathar, Ganesh K Rahane, Russell W Cross, Avinash V Rokade, Rupesh S Devan, Sadhu Kolekar, Robert LZ Hoye, et al. Solution-processed Cd-substituted CZTS nanocrystals for sensitized liquid junction solar cells. *Journal of Alloys and Compounds*, 890:161575, 2022.

[2] Siarhei Zhuk, Ajay Kushwaha, Terence KS Wong, Saeid Masudy-Panah, Aliaksandr Smirnov, and Goutam Kumar Dalapati. Critical review on sputter-deposited Cu_2ZnSnS_4 (CZTS) based thin film photovoltaic technology focusing on device architecture and absorber quality on the solar cells performance. *Solar Energy Materials and Solar Cells*, 171:239–252, 2017.

[3] MP Suryawanshi, GL Agawane, SM Bhosale, Seung Wook Shin, PS Patil, Jeong-Hoon Kim, and AV Moholkar. CZTS based thin film solar cells: a status review. *Materials Technology*, 28(1-2):98–109, 2013.

[4] Jatin N Roy and Dwarka N Bose. *Photovoltaic Science and Technology*. Cambridge University Press, 2018.

[5] Sadao Adachi. *Earth-abundant materials for solar cells: Cu_2-II-IV-VI_4 semiconductors*. John Wiley & Sons, 2015.

[6] Kiran Ranabhat, Leev Patrikeev, Aleksandra Antal'evna-Revina, Kirill Andrianov, Valerii Lapshinsky, and Elena Sofronova. An introduction to solar cell technology. *Journal of Applied Engineering Science*, 14(4):481–491, 2016.

[7] K. Ito. *Copper zinc tin sulfide-based thin-film solar cells*. John Wiley & Sons, 2014.

[8] Peter Würfel and Uli Würfel. *Physics of solar cells: from basic principles to advanced concepts*. John Wiley & Sons, 2016.

[9] Mohammad Istiaque Hossain. Prospects of czts solar cells from the perspective of material properties, fabrication methods and current research challenges. *Chalcogenide Letters*, 9(6), 2012.

[10] Albert Polman, Mark Knight, Erik C Garnett, Bruno Ehrler, and Wim C Sinke. Photovoltaic materials: Present efficiencies and future challenges. *Science*, 352(6283):aad4424, 2016.

[11] Laurence M Peter. Towards sustainable photovoltaics: the search for new materials. *Philosophical Transactions of the Royal Society A: Mathematical, Physical and Engineering Sciences*, 369(1942):1840–1856, 2011.

[12] Bharat R Bade, Sachin R Rondiya, Yogesh A Jadhav, Mahesh M Kamble, Sunil V Barma, Sagar B Jathar, Mamta P Nasane, Sandesh R Jadkar, Adinath M Funde, and Nelson Y Dzade. Investigations of the structural, optoelectronic and band alignment properties of Cu_2ZnSnS_4 prepared by hot-injection method towards low-cost photovoltaic applications. *Journal of Alloys and Compounds*, 854:157093, 2021.

[13] Billel Salhi. The photovoltaic cell based on cigs: Principles and technologies. *Materials*, 15(5):1908, 2022.

[14] Martin Green, Ewan Dunlop, Jochen Hohl-Ebinger, Masahiro Yoshita, Nikos Kopidakis, and Xiaojing Hao. Solar cell efficiency tables (version 57). *Progress in photovoltaics: research and applications*, 29(1):3–15, 2021.

[15] PA Fernandes, PMP Salomé, and AF Da Cunha. Study of polycrystalline Cu_2ZnSnS_4 films by Raman scattering. *Journal of alloys and compounds*, 509(28):7600–7606, 2011.

[16] Uma Ghorpade, Mahesh Suryawanshi, Seung Wook Shin, Kishor Gurav, Pramod Patil, Sambhaji Pawar, Chang Woo Hong, Jin Hyeok Kim, and Sanjay Kolekar. Towards environmentally benign approaches for the synthesis of CZTSSe nanocrystals by a hot injection method: a status review. *Chemical communications*, 50(77):11258–11273, 2014.

[17] Erteza Tawsif Efaz, Md Meganur Rhaman, Safayat Al Imam, Khandaker Lubaba Bashar, Fahmid Kabir, Syed Nazmus Sakib, and MD Ehasan Mourtaza. A review of major technologies of thin-film solar cells. *Engineering Research Express*, 2021.

[18] M Ravindiran and C Praveenkumar. Status review and the future prospects of CZTS based solar cell–A novel approach on the device structure and material modeling for CZTS based photovoltaic device. *Renewable and Sustainable Energy Reviews*, 94:317–329, 2018.

[19] Karthik Ramasamy, Mohammad A Malik, and Paul O'Brien. Routes to copper zinc tin sulfide Cu_2ZnSnS_4 a potential material for solar cells. *Chemical communications*, 48(46):5703–5714, 2012.

[20] Jia Feng, Xuan Huang, Wenzhi Chen, Jieyang Wu, Huangding Lin, Qijin Cheng, Daqin Yun, and Fengyan Zhang. Fabrication and characterization of Cu_2ZnSnS_4 thin films for photovoltaic application by low-cost single target sputtering process. *Vacuum*, 126:84–90, 2016.

[21] Qijie Guo, Grayson M Ford, Wei-Chang Yang, Bryce C Walker, Eric A Stach, Hugh W Hillhouse, and Rakesh Agrawal. Fabrication of 7.2% efficient CZTSSe solar cells using CZTS nanocrystals. *Journal of the American Chemical Society*, 132(49):17384–17386, 2010.

[22] Teodor K Todorov, Kathleen B Reuter, and David B Mitzi. High-efficiency solar cell with earth-abundant liquid-processed absorber. *Advanced materials*, 22(20):E156–E159, 2010.

[23] Yongtao Qu, Guillaume Zoppi, Robert W Miles, and Neil S Beattie. Influence of reaction conditions on the properties of solution-processed Cu_2ZnSnS_4 nanocrystals. *Materials Research Express*, 1(4):045040, 2014.

[24] Susan E Habas, Heather AS Platt, Maikel FAM van Hest, and David S Ginley. Low-cost inorganic solar cells: from ink to printed device. *Chemical reviews*, 110(11):6571–6594, 2010.

[25] Naghmehalsadat Mirbagheri, S Engberg, Andrea Crovetto, Søren Bredmose Simonsen, Ole Hansen, Yeng Ming Lam, and Jørgen Schou. Synthesis of ligand-free CZTS nanoparticles via a facile hot injection route. *Nanotechnology*, 27(18):185603, 2016.

[26] Suresh Kumar, Vikash Kumar, Valdek Mikli, Tiit Varema, Mare Altosaar, and Maarja Grossberg. Study of CZTS nano-powder synthesis by hot injection method by variation of Cu and Zn concentrations. *Energy Procedia*, 102: 136–143, 2016.

[27] Ubaidah Syafiq, Narges Ataollahi, Rosa Di Maggio, and Paolo Scardi. Solution-based synthesis and characterization of Cu_2ZnSnS_4 (CZTS) thin films. *Molecules*, 24(19):3454, 2019.

[28] Vincenzo Muteri, Maurizio Cellura, Domenico Curto, Vincenzo Franzitta, Sonia Longo, Marina Mistretta, and Maria Laura Parisi. Review on life cycle assessment of solar photovoltaic panels. *Energies*, 13(1):252, 2020.

[29] Karthikeyan Vijayan, SP Vijayachamundeeswari, Kalainathan Sivaperuman, Nazmul Ahsan, Thirumalaisamy Logu, and Yoshitaka Okada. A review on advancements, challenges, and prospective of copper and non-copper based

thin-film solar cells using facile spray pyrolysis technique. *Solar Energy*, 234: 81–102, 2022.

[30] O Vigil-Galán, Maykel Courel, JA Andrade-Arvizu, Y Sánchez, M Espíndola-Rodríguez, E Saucedo, D Seuret-Jiménez, and Matthew Titsworth. Route towards low cost-high efficiency second generation solar cells: current status and perspectives. *Journal of Materials Science: Materials in Electronics*, 26: 5562–5573, 2015.

[31] MA Olgar, A Seyhan, AO Sarp, and R Zan. Impact of sulfurization parameters on properties of czts thin films grown using quaternary target. *Journal of Materials Science: Materials in Electronics*, 31:20620–20631, 2020.

[32] Indu Gupta, Arnab Dey, and Rahul Jain. Non-toxic solution processed cu2znsn (sse) 4 thin films for photovoltaic applications: A review. *Materials Today: Proceedings*, 2023.

[33] Chuanhe Ma, Xiaoshuang Lu, Bin Xu, Fei Zhao, Xueer An, Bo Li, Fangyu Yue, Jinchun Jiang, Ye Chen, Lin Sun, et al. Effect of czts/cds interfaces deposited with sputtering and cbd methods on voc deficit and efficiency of czts solar cells. *Journal of Alloys and Compounds*, 817:153329, 2020.

[34] D. Sharma, R. Mehra, and B. Raj. Comparative analysis of photovoltaic technologies for high efficiency solar cell design. *Superlattices and Microstructures*, 153:106861, 2021.

[35] N. Rathore. A comprehensive review of different types of solar photovoltaic cells and their applications. *International Journal of Ambient Energy*, 42 (10):1200–1217, 2021.

[36] A.S. Al-Ezzi and M.N.M. Ansari. Photovoltaic Solar Cells: A Review. *Applied System Innovation*, 5(4):67, 2022.

[37] Martin A Green, Keith Emery, Yoshihiro Hishikawa, Wilhelm Warta, and ED Dunlop. Progress in photovoltaics: research and applications. *Prog. Photovoltaics*, 21:827–837, 2013.

[38] M. Dhankhar, O.P. Singh, and V. Singh. Physical principles of losses in thin film solar cells and efficiency enhancement methods. *Renewable and Sustainable Energy Reviews*, 40:214–223, 2014.

[39] J.N. Roy and D.N. Bose. *Photovoltaic Science and Technology*. Cambridge University Press, 2018.

[40] K. Ito. *Copper zinc tin sulfide-based thin-film solar cells*. John Wiley & Sons, 2014.

[41] E.C. Cho. Silicon quantum dots in a dielectric matrix for all-silicon tandem solar cells. *Advances in Opto Electronics*, 2007.

[42] I.H. Khudayer. Study of physical and optoelectronic properties of $CuInSe_2$/Si heterojunction solar cells. *Energy Procedia*, 119:507–517, 2017.

[43] J.A. Nelson. *The physics of solar cells*. World Scientific Publishing Company, 2003.

[44] J. Cubas, S. Pindado, and C. Manuel. Explicit expressions for solar panel equivalent circuit parameters based on analytical formulation and the Lambert W-function. *Energies*, 7(7):4098–4115, 2014.

[45] L.C. Hirst and N.J. Ekins-Daukes. Fundamental losses in solar cells. *Progress in Photovoltaics: Research and Applications*, 19(3):286–293, 2011.

[46] A. Wang and Y. Xuan. A detailed study on loss processes in solar cells. *Energy*, 144:490–500, 2018.

[47] M. Courel, J. Andrade-Arvizu, and O. Vigil-Galán. Loss mechanisms influence on Cu_2ZnSnS_4/CdS-based thin film solar cell performance. *Solid-State Electronics*, 111:243–250, 2015.

[48] S. Siebentritt. Why are kesterite solar cells not 20% efficient? *Thin Solid Films*, 535:1–4, 2013.

[49] T.J. Whittles. *Electronic Characterisation of Earth-Abundant Sulphides for Solar Photovoltaics*. Springer, 2018.

[50] L. Sravani. Loss mechanisms in CZTS and CZTSe Kesterite thin-film solar cells: Understanding the complexity of defect density. *Solar Energy*, 227: 56–66, 2021.

[51] M. Courel. Towards understanding poor performances in spray-deposited Cu_2ZnSnS_4 thin film solar cells. *Solar energy materials and solar cells*, 159: 151–158, 2017.

[52] M. Yamaguchi. Analysis for non-radiative recombination and resistance loss in chalcopyrite and kesterite solar cells. *Japanese Journal of Applied Physics*, 60(SB):05, 2021.

[53] C.S. Solanki. *Solar photovoltaics: fundamentals, technologies and applications*. Phi learning pvt. Ltd, 2015.

[54] M. Yamaguchi. Analysis of future generation solar cells and materials. *Japanese Journal of Applied Physics*, 57(4S):04 03, 2018.

[55] A.C. Badgujar, R.O. Dusane, S.R. Dhage, and Cu. Se2 thin film solar cells produced by atmospheric selenization of spray casted nanocrystalline layers. *Solar Energy*, 209:1–10, 2020.

[56] H. Zhou. CZTS nanocrystals: a promising approach for next generation thin film photovoltaics. *Energy & Environmental Science*, 6(10):2822–2838, 2013.

[57] D. Xia. Synthesis and characterization of Cu_2ZnSnS_4 nanocrystals by hot-injection method. *Journal of Materials Science: Materials in Electronics*, 26 (7):5426–5432, 2015.

[58] T. Zheng. An effective air heat-treatment strategy of precursor films in search of high open-circuit voltage for efficient CZTSSe cells. *Solar Energy Materials and Solar Cells*, 239:111662, 2022.

[59] T. Ratz. Physical routes for the synthesis of kesterite. *Journal of Physics: Energy*, 1(4):042003, 2019.

[60] X. Zhang. Fabrication of Cu_2ZnSnS_4 Thin Films from Ball-Milled Nanoparticle inks under Various Annealing Temperatures. *Nanomaterials*, 9(11): 1615, 2019.

[61] M.F. Islam, N.M. Yatim, and M.A. Hashim. A review of CZTS thin film solar cell technology. *Journal of Advanced Research in Fluid Mechanics and Thermal Sciences*, 81(1):73–87, 2021.

[62] J.M.R. Tan. Understanding the synthetic pathway of a single-phase quaternary semiconductor using surface-enhanced Raman scattering: a case of wurtzite Cu_2ZnSnS_4 nanoparticles. *Journal of the American Chemical Society*, 136(18):6684–6692, 2014.

[63] Best research-cell efficiency chart. *NREL Website*, 2023. URL `https://www.nrel.gov/pv/cell-efficiency.html`.

[64] J. Paier. Cu 2 ZnSnS 4 as a potential photovoltaic material: a hybrid Hartree-Fock density functional theory study. *Physical Review B*, 79(11):115126, 2009.

[65] A. Walsh. Crystal structure and defect reactions in the kesterite solar cell absorber Cu 2 ZnSnS 4 (CZTS): theoretical insights. In *AIP Conference Proceedings*. American Institute of Physics, 2011.

[66] S. Zhuk. Critical review on sputter-deposited Cu_2ZnSnS_4 (CZTS) based thin film photovoltaic technology focusing on device architecture and absorber quality on the solar cells performance. *Solar Energy Materials and Solar Cells*, 171:239–252, 2017.

[67] S. Engberg. Characterization of Cu_2ZnSnS_4 Particles Obtained by the Hot-Injection Method. *ACS omega*, 5(18):10501–10509, 2020.

[68] C. Malerba. CZTS stoichiometry effects on the band gap energy. *Journal of alloys and compounds*, 582:528–534, 2014.

[69] U. Ghorpade. Towards environmentally benign approaches for the synthesis of CZTSSe nanocrystals by a hot injection method: a status review. *Chemical communications*, 50(77):11258–11273, 2014.

[70] Kalyan B Chavan, Sachin V Desarada, and Nandu B Chaure. Structural and optical investigations on direct current (dc) magnetron sputtered czts thin film. *Materials Today: Proceedings*, 68:2687–2690, 2022.

[71] T.J. Huang. *CZTS-based materials and interfaces and their effects on the performance of thin film solar cells. physica status solidi*, volume 8. RRL)–Rapid Research Letters, 2014.

[72] K. Pal. Current challenges and future prospects for a highly efficient ($> 20\%$) kesterite CZTS solar cell: A review. *Solar Energy Materials and Solar Cells*, 196:138–156, 2019.

[73] J.J. Scragg. *Copper Zinc Tin Sulfide Thin Films for Photovoltaics: Synthesis and Characterisation by Electrochemical Methods*. Springer Science & Business Media, 2011.

[74] A. Tang. One-step electrodeposition for targeted off-stoichiometry Cu_2ZnSnS_4 thin films. *Applied Surface Science*, 383:253–260, 2016.

[75] S. Swati. *Experimental study of the optical properties of Cu_2ZnSnS_4 thin film absorber layer for solar cell application.* in Journal of Physics: Conference Series. IOP Publishing, 2018.

[76] R. Caballero. Non-stoichiometry effect and disorder in Cu_2ZnSnS_4 thin films obtained by flash evaporation: Raman scattering investigation. *Acta Materialia*, 65:412–417, 2014.

[77] S. Chamekh, N. Khemiri, and M. Kanzari. Effect of annealing under different atmospheres of CZTS thin films as absorber layer for solar cell application. *SN Applied Sciences*, 2(9):1–8, 2020.

[78] S. Vanalakar. Effect of post-annealing atmosphere on the grain-size and surface morphological properties of pulsed laser deposited CZTS thin films. *Ceramics International*, 40(9):15097–15103, 2014.

[79] N. Shaalan, A. Mahmoud, and D. Hamad. Synthesis of CZTS without sulfurization process and its performance evaluation on n-Si substrate as ITO-free photovoltaic cell. *Materials Science in Semiconductor Processing*, 120:105318, 2020.

[80] Z. Gong. A solvothermal route to synthesize kesterite Cu_2ZnSnS_4 nanocrystals for solution-processed solar cells. *Journal of Alloys and Compounds*, 663: 617–623, 2016.

[81] F.I. Lai. Weatherability of $Cu_2ZnSnSe_4$ thin film solar cells on diverse substrates. *Solar Energy*, 195:626–635, 2020.

[82] G. Gordillo, C. Calderón, and R. Moreno. Fabrication of solar cells based on Cu_2ZnSnS_4 films grown with optimized chemical composition homogeneity. *Revista de la Academia Colombiana de Ciencias Exactas, Físicas y Naturales*, 43(166):17–23, 2019.

[83] X. Jin. Pulsed laser deposition of Cu_2ZnSnS_4 thin films from single quaternary sulfide target prepared by combustion method. *Materials Letters*, 175: 180–183, 2016.

[84] M. Ravindiran and C. Praveenkumar. Status review and the future prospects of CZTS based solar cell–A novel approach on the device structure

and material modeling for CZTS based photovoltaic device. *Renewable and Sustainable Energy Reviews*, 94:317–329, 2018.

[85] B. Unveroglu and G. Zangari. Photovoltaic performance of Cu_2ZnSnS_4 thin film solar cells on flexible molybdenum foil formed by electrodeposition and sulfurization. *Journal of Materials Science: Materials in Electronics*, 33(6): 3101–3114, 2022.

[86] S. Shin. Cyclic voltammetry studies of copper, tin and zinc electrodeposition in a citrate complex system for CZTS solar cell application. *Current Applied Physics*, 16(2):207–210, 2016.

[87] C. Zhang, J. Tao, and J. Chu. An 8.7% efficiency co-electrodeposited Cu 2 ZnSnS 4 photovoltaic device fabricated via a pressurized post-sulfurization process. *Journal of Materials Chemistry C*, 6(48):13275–13282, 2018.

[88] M.P. Suryawanshi. Aqueous-Solution-Processed Cu2ZnSn (S, Se) 4 Thin-Film Solar Cells via an Improved Successive Ion-Layer-Adsorption–Reaction Sequence. *ACS omega*, 2(12):9211–9220, 2017.

[89] I. Repins. Co-evaporated $Cu_2ZnSnSe_4$ films and devices. *Solar Energy Materials and Solar Cells*, 101:154–159, 2012.

[90] Y.S. Lee. $Cu_2ZnSnSe_4$ thin-film solar cells by thermal co-evaporation with 11.6% efficiency and improved minority carrier diffusion length. *Advanced Energy Materials*, 5(7):1401372, 2015.

[91] W.S. Liu. Investigation of Zn/Sn ratio for improving the material quality of CZTS thin films with the reduction of $Cu_{2-x}S$ secondary phase. *Journal of Alloys and Compounds*, 853:157237, 2021.

[92] G. Agawane. Fabrication of 3.01% power conversion efficient high-quality CZTS thin film solar cells by a green and simple sol–gel technique. *Materials Letters*, 158:58–61, 2015.

[93] A. Krishnan. Towards phase pure CZTS thin films by SILAR method with augmented Zn adsorption for photovoltaic applications. *Materials for Renewable and Sustainable Energy*, 8(3):1–8, 2019.

[94] E. Mkawi. Fabricating chalcogenide Cu_2ZnSnS_4 (CZTS) nanoparticles via solvothermal synthesis: Effect of the sulfur source on the properties. *Ceramics International*, 46(16):24916–24922, 2020.

[95] Q. Guo. Fabrication of 7.2% efficient CZTSSe solar cells using CZTS nanocrystals. *Journal of the American Chemical Society*, 132(49):17384–17386, 2010.

[96] Y. Qu, G. Zoppi, and N.S. Beattie. The role of nanoparticle inks in determining the performance of solution processed Cu2ZnSn (S, Se) 4 thin film solar cells. *Progress in Photovoltaics: Research and Applications*, 24(6):836–845, 2016.

[97] G.M. Ford. Earth abundant element $Cu_2Zn(Sn_{1-x}Ge_x)S_4$ nanocrystals for tunable band gap solar cells: 6.8% efficient device fabrication. *Chemistry of Materials*, 23(10):2626–2629, 2011.

[98] A. Kowsar. Progress in major thin-film solar cells: Growth technologies, layer materials and efficiencies. *International Journal of Renewable Energy Research (IJRER*, 9(2):579–597, 2019.

[99] K. Orgassa, H.W. Schock, and J. Werner. Alternative back contact materials for thin film Cu(In,Ga)Se_2 solar cells. *Thin Solid Films*, 431:387–391, 2003.

[100] S. Azmi. Growth of Cu_2ZnSnS_4 thin film absorber layer on transparent conductive oxides and molybdenum substrates by electrodeposition for photovoltaic application. *Optik*, 250:168320, 2022.

[101] V.M. Fthenakis and H.C. Kim. CdTe photovoltaics: Life cycle environmental profile and comparisons. *Thin Solid Films*, 515(15):5961–5963, 2007.

[102] Y.Y. Prawira. All-Solution-Non-Vacuum Fabrication Process of CZTS Solar Cell using ZTO as Non-Toxic Buffer Layer. *International Journal of Nanoelectronics & Materials*, 13(2), 2020.

[103] K.K. Maurya and V.N. Singh. Comparison of Various Thin-Film-Based Absorber Materials: A Viable Approach for Next-Generation Solar Cells. *Coatings*, 12(3):405, 2022.

[104] J. Li. Interface recombination of Cu_2ZnSnS_4 solar cells leveraged by high carrier density and interface defects. *Solar RRL*, 5(10):2100418, 2021.

[105] K. Ernits. Improvement of VOC in Cu_2ZnSnS_4 monograin layer solar cells with tin oxide inter-layer. In *2015 IEEE 42nd Photovoltaic Specialist Conference (PVSC)*. IEEE, 2015.

[106] S. Ranjbar. P–N Junction Passivation in Kesterite Solar Cells by Use of Solution-Processed TiO_2 Layer. *IEEE Journal of Photovoltaics*, 7(4):1130–1135, 2017.

[107] K.S. Gour. An alternative buffer layer for chalcogenide and kesterite based thin films solar cells: A review. *Journal of Nanoscience and Nanotechnology*, 20(6):3622–3635, 2020.

[108] N.M. Martin. Atomic Layer Grown Zinc–Tin Oxide as an Alternative Buffer Layer for Cu_2ZnSnS_4-Based Thin Film Solar Cells: Influence of Absorber Surface Treatment on Buffer Layer Growth. *ACS Applied Energy Materials*, 2022.

[109] A. Bahfir, M. Boumaour, and M. Kechouane. Prospects of potential ZnMgO front layer in CZTS solar cells. *Optik*, 169:196–202, 2018.

[110] L.M. Peter. Towards sustainable photovoltaics: the search for new materials. *Philosophical Transactions of the Royal Society A: Mathematical, Physical and Engineering Sciences*, 369(1942):1840–1856, 2011.

[111] M. Suryawanshi. CZTS based thin film solar cells: a status review. *Materials Technology*, 28(1-2):98–109, 2013.

[112] M. Green. Solar cell efficiency tables (version 57. *Progress in photovoltaics: research and applications*, 29(1):3–15, 2021.

[113] F. Sava. Secondary crystalline phases influence on optical properties in off-stoichiometric Cu2S–ZnS–SnS2 thin films. *Materials*, 13(20):4624, 2020.

[114] C. Sripan. Influence of solvent on solution processed Cu_2ZnSnS_4 nanocrystals and annealing induced changes in the optical, structural properties of CZTS film. *Current Applied Physics*, 20(8):925–930, 2020.

[115] A.M. Elseman and M. Rashad. Influence of nitrogen atmosphere one-step heating assisted the solution processing of Kesterite Cu_2ZnSnS_4 as hole extraction on the efficacy of the inverted perovskite solar cells. *Optical Materials*, 124:111998, 2022.

[116] M. Olgar. Optimization of sulfurization time and temperature for fabrication of Cu_2ZnSnS_4 (CZTS) thin films. *Superlattices and Microstructures*, 126:32–41, 2019.

[117] X. Shi. Significantly improving the crystal growth of a $Cu_2ZnSn(S,Se)_4$ absorber layer by air-annealing a Cu_2ZnSnS_4 precursor thin film. *ACS Applied Materials & Interfaces*, 12(37):41590–41595, 2020.

[118] Boris D Chernomordik, Amélie E Béland, Donna D Deng, Lorraine F Francis, and Eray S Aydil. Microstructure evolution and crystal growth in cu2znsns4 thin films formed by annealing colloidal nanocrystal coatings. *Chemistry of Materials*, 26(10):3191–3201, 2014.

[119] O. Gunawan, T.K. Todorov, D.B. Mitzi, and S. Se. Loss mechanisms in hydrazine-processed Cu_2ZnSn . *Applied Physics Letters*, 97(23):233506, 2010.

[120] M. Kumar. Strategic review of secondary phases, defects and defect-complexes in kesterite CZTS–Se solar cells. *Energy & Environmental Science*, 8(11):3134–3159, 2015.

[121] A. Kanevce, I. Repins, and S.H. Wei. Impact of bulk properties and local secondary phases on the $Cu_2(Zn,Sn)Se_4$ solar cells open-circuit voltage. *Solar Energy Materials and Solar Cells*, 133:119–125, 2015.

[122] A. Nagoya. Defect formation and phase stability of Cu_2ZnSnS_4 photovoltaic material. *Physical Review B*, 81(11):113202, 2010.

[123] S. Chen. Classification of lattice defects in the kesterite Cu_2ZnSnS_4 and Cu2ZnSnSe4 earth-abundant solar cell absorbers. *Advanced materials*, 25 (11):1522–1539, 2013.

[124] Harbi Setyo Nugroho, Gema Refantero, Ni Luh Wulan Septiani, Muhammad Iqbal, Septhian Marno, Huda Abdullah, Eka Cahya Prima, Brian Yuliarto, et al. A progress review on the modification of czts (e)-based thin-film solar cells. *Journal of Industrial and Engineering Chemistry*, 105:83–110, 2022.

[125] G.Y. Kim. Effects of $Cu_{2-x}S$ phase removal on surface potential of Cu_2ZnSnS_4 thin-films grown by electroplating. *Current Applied Physics*, 14 (12):1665–1668, 2014.

[126] H. Katagiri. Enhanced conversion efficiencies of Cu_2ZnSnS_4-based thin film solar cells by using preferential etching technique. *Applied Physics Express*, 1(4):041201, 2008.

[127] J. Zeng. Na incorporation controlled single phase kesterite Cu_2ZnSnS_4 solar cell material. *Materials Letters*, 265:127355, 2020.

[128] A. Crovetto. Cu_2ZnSnS_4 solar cells: Physics and technology by alternative tracks, 2016.

[129] H. Ehira, K. Jimbo, and H. Katagiri. Impact of Na-addition effect into CZTS thin film solar cells. In *AIP Conference Proceedings.* AIP Publishing LLC, 2017.

[130] T. Prabhakar and N. Jampana. Effect of sodium diffusion on the structural and electrical properties of Cu_2ZnSnS_4 thin films. *Solar Energy Materials and Solar Cells*, 95(3):1001–1004, 2011.

[131] Jonathan JS Scragg, Jes K Larsen, Mukesh Kumar, Clas Persson, Jan Sendler, Susanne Siebentritt, and Charlotte Platzer Björkman. Cu–zn disorder and band gap fluctuations in cu2znsn (s, se) 4: Theoretical and experimental investigations. *physica status solidi (b)*, 253(2):247–254, 2016.

[132] Iulian Boerasu and Bogdan Stefan Vasile. Current status of the open-circuit voltage of kesterite czts absorber layers for photovoltaic applications—part i, a review. *Materials*, 15(23):8427, 2022.

[133] K. Pal, K.B. Thapa, and A. Bhaduri. *A review on the current and future possibilities of copper-zinc tin sulfur thin film solar cell to increase more than 20% efficiency*, volume 10. Advanced Science, Engineering and Medicine, 2018.

[134] H.S. Nugroho. A progress review on the modification of CZTS(e)-based thin-film solar cells. *Journal of Industrial and Engineering Chemistry*, 105:83–110, 2022.

[135] Jonathan J Scragg, Phillip J Dale, Diego Colombara, and Laurence M Peter. Thermodynamic aspects of the synthesis of thin-film materials for solar cells. *ChemPhysChem*, 13(12):3035–3046, 2012.

[136] C. Yan. Boost V_{oc} of pure sulfide kesterite solar cell via a double CZTS layer stacks. *Solar Energy Materials and Solar Cells*, 160:7–11, 2017.

[137] K. Wang. Thermally evaporated Cu_2ZnSnS_4 solar cells. *Applied Physics Letters*, 97(14):143508, 2010.

[138] Z. Tong. Modification of absorber quality and Mo-back contact by a thin Bi intermediate layer for kesterite Cu_2ZnSnS_4 solar cells. *Solar Energy Materials and Solar Cells*, 144:537–543, 2016.

[139] H. Guo. Dual function of ultrathin Ti intermediate layers in CZTS solar cells: Sulfur blocking and charge enhancement. *Solar Energy Materials and Solar Cells*, 175:20–28, 2018.

[140] H. Cui. Improving efficiency of evaporated Cu_2ZnSnS_4 thin film solar cells by a thin Ag intermediate layer between absorber and back contact. *International Journal of Photoenergy*, 2015.

[141] F. Liu. Beyond 8% ultrathin kesterite Cu_2ZnSnS_4 solar cells by interface reaction route controlling and self-organized nanopattern at the back contact. *NPG Asia Materials*, 9(7):401– 401, 2017.

[142] J. Park. The effect of thermal evaporated MoO_3 intermediate layer as primary back contact for kesterite Cu_2ZnSnS_4 solar cells. *Thin Solid Films*, 648:39–45, 2018.

[143] Samaneh Sharbati and James R Sites. Impact of the Band Offset for n-Zn(O,S)/p-Cu(In,Ga)Se_2 Solar Cells. *IEEE Journal of Photovoltaics*, 4(2): 697–702, 2014.

[144] Heng Sun, Kaiwen Sun, Jialiang Huang, Chang Yan, Fangyang Liu, Jongsung Park, Aobo Pu, John A. Stride, Martin A. Green, and Xiaojing Hao. Efficiency enhancement of kesterite cu2znsns4 solar cells via solution-processed ultrathin tin oxide intermediate layer at absorber/buffer interface. *ACS Applied Energy Materials*, 1(1):154–160, 2018.

[145] Chang Woo Hong, Seung Wook Shin, Mahesh P. Suryawanshi, Myeng Gil Gang, Jaeyeong Heo, and Jin Hyeok Kim. Chemically deposited cds buffer/kesterite cu2znsns4 solar cells: Relationship between cds thickness and

device performance. *ACS Applied Materials & Interfaces*, 9(42):36733–36744, 2017.

[146] S. Gao. Interfaces of high-efficiency kesterite $Cu_2ZnSnS(e)_4$ thin film solar cells. *Chinese Physics B*, 27(1):018803, 2018.

[147] D.C. Nguyen. Making nanoparticle ink for compound solar cells. *SPIE Newsroom*, 2013.

[148] Q. Guo, H.W. Hillhouse, and R. Agrawal. Synthesis of Cu_2ZnSnS_4 nanocrystal ink and its use for solar cells. *Journal of the American Chemical Society*, 131(33):11672–11673, 2009.

[149] E. Gu. Cu_2ZnSnS_4 thin film solar cells from coated nanocrystals ink. *Journal of Materials Science: Materials in Electronics*, 26(3):1932–1939, 2015.

[150] M. Paris. Solid-state NMR and Raman spectroscopy to address the local structure of defects and the tricky issue of the Cu/Zn disorder in Cu-poor, Zn-rich CZTS materials. *Inorganic chemistry*, 53(16):8646–8653, 2014.

[151] S. Chen. Defect physics of the kesterite thin-film solar cell absorber Cu_2ZnSnS_4 . *Applied Physics Letters*, 96(2):021902, 2010.

[152] D. Xia. Characterization of Cu_2ZnSnS_4 thin films prepared by solution-based deposition technique. *Physics Procedia*, 48:228–234, 2013.

[153] R. Ahmad. Facile synthesis and post-processing of eco-friendly, highly conductive copper zinc tin sulphide nanoparticles. *Journal of nanoparticle research*, 15(9):1–16, 2013.

[154] Y. Qu. Influence of reaction conditions on the properties of solution-processed Cu_2ZnSnS_4 nanocrystals. *Materials Research Express*, 1(4):045040, 2014.

[155] V.M.H. Cao. Fabrication of the Cu_2ZnSnS_4 Thin Film Solar Cell via a Photo-Sintering Technique. *Applied Sciences*, 12(1):38, 2021.

[156] Yongtao Qu. *Cu 2 ZnSn (S, Se) 4 Solar Cells Prepared from Cu 2 ZnSnS 4 Nanoparticle Inks*. University of Northumbria at Newcastle (United Kingdom), 2015.

[157] Kazuya Maeda, Kunihiko Tanaka, Yuki Fukui, and Hisao Uchiki. Influence of h2s concentration on the properties of cu2znsns4 thin films and solar cells prepared by sol–gel sulfurization. *Solar Energy Materials and Solar Cells*, 95 (10):2855–2860, 2011.

[158] Chinnaiyah Sripan, R Ganesan, EM Vinod, and Annamraju Kasi Viswanath. The effect of sulfur on the phase formation of cu2znsns4 solar cell material. *Materials Letters*, 180:295–297, 2016.

[159] W. Zhou and Z.L. Wang. *Scanning microscopy for nanotechnology: techniques and applications*. Springer science & business media, 2007.

[160] M. Sezen and M. Janecek. Focused Ion Beams (FIB)—Novel methodologies and recent applications for multidisciplinary sciences. *Modern Electron Microscopy in Physical and Life Sciences*, pages 121–140, 2016.

[161] S. Adachi. *Earth-abundant materials for solar cells: Cu2-II-IV-VI4 semiconductors*. John Wiley & Sons, 2015.

[162] Michaël Paris, Léo Choubrac, Alain Lafond, Catherine Guillot-Deudon, and Stéphane Jobic. Solid-state NMR and Raman spectroscopy to address the local structure of defects and the tricky issue of the Cu/Zn disorder in Cu-poor, Zn-rich CZTS materials. *Inorganic chemistry*, 53(16):8646–8653, 2014.

[163] Taoufik Slimani Tlemçani, Fouzia Cherkaoui El Moursli, Faiza Hajji, Zineb Edfouf, Mhamed Taibi, Hicham Labrim, Bouchra Belhorma, Safae Aazou, Guy Schmerber, Karima Bouras, et al. Deposition time effect on the physical properties of Cu_2ZnSnS_4 (CZTS) thin films obtained by electrodeposition route onto Mo-coated glass substrates. *Energy Procedia*, 84:127–133, 2015.

[164] A Méndez-López, A Morales-Acevedo, YJ Acosta-Silva, and M Ortega-López. Synthesis and characterization of colloidal CZTS nanocrystals by a hot-injection method. *Journal of Nanomaterials*, 2016, 2016.

[165] T Chtouki, L Soumahoro, B Kulyk, H Bougharraf, H Erguig, K Ammous, and B Sahraoui. Comparative study on the structural, morphological, linear and nonlinear optical properties of CZTS thin films prepared by spin-coating and spray pyrolysis. *Materials Today: Proceedings*, 4(4):5146–5153, 2017.

[166] EM Mkawi, K Ibrahim, MKM Ali, MA Farrukh, and AS Mohamed. Influence of triangle wave pulse on the properties of Cu_2ZnSnS_4 thin films prepared by single step electrodeposition. *Solar energy materials and solar cells*, 130: 91–98, 2014.

[167] Shefali Jain, Sanjay Kumar Swami, Viresh Dutta, and Shailesh Narain Sharma. Impact on structural, morphological, and compositional properties of CZTS thin films annealed in different environments. *Inorganic Chemistry Communications*, 133:108879, 2021.

[168] Nabeel A Bakr, Ziad T Khodair, and Hussein I Mahdi. Influence of thiourea concentration on some physical properties of chemically sprayed Cu_2ZnSnS_4 thin films. *International Journal of Materials Science and Applications*, 5(6): 261–270, 2016.

[169] H Ahmoum, P Chelvanathan, MS Su'ait, M Boughrara, G Li, Ali HA Al-Waeli, K Sopian, M Kerouad, and N Amin. Impact of preheating environment on microstructural and optoelectronic properties of Cu_2ZnSnS_4 (CZTS) thin films deposited by spin-coating. *Superlattices and Microstructures*, 140: 106452, 2020.

[170] Shiyou Chen, XG Gong, Aron Walsh, and Su-Huai Wei. Crystal and electronic band structure of Cu_2ZnSnX_4 (X=S and Se) photovoltaic absorbers: First-principles insights. *Applied Physics Letters*, 94(4):041903, 2009.

[171] YB Kishore Kumar, G Suresh Babu, P Uday Bhaskar, and V Sundara Raja. Preparation and characterization of spray-deposited Cu_2ZnSnS_4 thin films. *Solar Energy Materials and Solar Cells*, 93(8):1230–1237, 2009.

[172] P Prabeesh, I Packia Selvam, and SN Potty. CZTS films from three different routes: crystallite size-dependent properties. *Materials Research Express*, 6 (6):065509, 2019.

[173] Wei Li, Jian Chen, Chang Yan, and Xiaojing Hao. The effect of ZnS segregation on Zn-rich CZTS thin film solar cells. *Journal of Alloys and Compounds*, 632:178–184, 2015.

[174] J Henry, K Mohanraj, and G Sivakumar. Electrical and optical properties of CZTS thin films prepared by SILAR method. *Journal of Asian Ceramic Societies*, 4(1):81–84, 2016.

[175] AG Kannan, TE Manjulavalli, and J Chandrasekaran. Influence of solvent on the properties of CZTS nanoparticles. *Procedia Engineering*, 141:15–22, 2016.

[176] MA Olgar, A Altuntepe, S Erkan, and R Zan. Fabrication of Cu-rich CZTS thin films by two-stage process: Effect of gas flow-rate in sulfurization process. *Journal of Molecular Structure*, 1230:129922, 2021.

[177] Hassan Ahmoum, Puvaneswaran Chelvanathan, Mohd Sukor Su'ait, Mourad Boughrara, Guojian Li, Ralph Gebauer, Kamaruzzaman Sopian, Mohamed Kerouad, Nowshad Amin, and Qiang Wang. Sol-gel prepared Cu_2ZnSnS_4 (CZTS) semiconductor thin films: Role of solvent removal processing temperature. *Materials Science in Semiconductor Processing*, 132:105874, 2021.

[178] Sara Engberg, Joanna Symonowicz, Jørgen Schou, Stela Canulescu, and Kirsten M Ø Jensen. Characterization of Cu_2ZnSnS_4 Particles Obtained by the Hot-Injection Method. *ACS omega*, 5(18):10501–10509, 2020.

[179] C. J. Bosson, M. T. Birch, D. P. Halliday, K. S. Knight, A. S. Gibbs, and P. D. Hatton. Cation disorder and phase transitions in the structurally complex solar cell material Cu_2ZnSnS_4. *J. Mater. Chem. A*, 5:16672–16680, 2017.

[180] Leilei Chen, Hongmei Deng, Jiahua Tao, Huiyi Cao, Ling Huang, Lin Sun, Pingxiong Yang, and Junhao Chu. Synthesis and characterization of earth-abundant Cu_2MnSnS_4 thin films using a non-toxic solution-based technique. *RSC advances*, 5(102):84295–84302, 2015.

[181] Dongxu Zhang, Bin Yao, Yongfeng Li, Zhanhui Ding, Chunkai Wang, Jiayong Zhang, Ting Wang, Ding Ma, and Yue Liu. Insight into the role of air-annealing Cu_2ZnSnS_4 precursor films in improving efficiency of Cu2ZnSn(S,Se)4 solar cells. *Journal of Alloys and Compounds*, 929:167308, 2022.

[182] Ahmed Ziti, Bouchaib Hartiti, Hicham Labrim, Salah Fadili, Abderraouf Ridah, Bouchra Belhorma, Mounia Tahri, and Philippe Thevenin. Study of kesterite CZTS thin films deposited by spin coating technique for photovoltaic applications. *Superlattices and Microstructures*, 127:191–200, 2019.

[183] Srinivasan Thiruvenkadam, D. Jovina, and A. Leo Rajesh. The influence of deposition temperature in the photovoltaic properties of spray deposited CZTS thin films. *Solar Energy*, 106:166–170, 2014.

[184] Bo Long, Shuying Cheng, Dapeng Ye, Chuang Yue, and Jie Liao. Mechanistic aspects of preheating effects of precursors on characteristics of Cu_2ZnSnS_4 (CZTS) thin films and solar cells. *Materials Research Bulletin*, 115:182–190, 2019.

[185] Marit Kauk-Kuusik, Kristi Timmo, Katri Muska, Maris Pilvet, Jüri Krustok, Raavo Josepson, Guy Brammertz, Bart Vermang, Mati Danilson, and Maarja Grossberg. Detailed Insight into the CZTS/CdS Interface Modification by Air

Annealing in Monograin Layer Solar Cells. *ACS Applied Energy Materials*, 4 (11):12374–12382, 2021.

[186] M Kauk-Kuusik, K Timmo, K Muska, M Pilvet, J Krustok, M Danilson, V Mikli, R Josepson, and M Grossberg-Kuusk. Reduced recombination through CZTS/CdS interface engineering in monograin layer solar cells. *Journal of Physics: Energy*, 4(2):024007, 2022.

[187] Mitisha Baid, Ayesha Hashmi, Bhawana Jain, Ajaya Kumar Singh, Md Susan, Abu Bin Hasan, and Mariya Aleksandrova. A comprehensive review on Cu_2ZnSnS_4 (CZTS) thin film for solar cell: forecast issues and future anticipation. *Optical and Quantum Electronics*, 53(11):1–45, 2021.

[188] M.F. Sanchez, T.G. Sanchez, Maykel Courel, O. Reyes-Vallejo, Y. Sanchez, E. Saucedo, and P.J. Sebastian. Effect of post annealing thermal heating on Cu_2ZnSnS_4 solar cells processed by sputtering technique. *Solar Energy*, 237: 196–202, 2022.

[189] Om Pal Singh, Kuldeep Singh Gour, Rahul Parmar, and Vidya Nand Singh. Sodium induced grain growth, defect passivation and enhancement in the photovoltaic properties of Cu_2ZnSnS_4 thin film solar cell. *Materials Chemistry and Physics*, 177:293–298, 2016.

[190] Chan Kim and Sungwook Hong. Optical and electrical properties of Cu_2ZnSnS_4 thin films grown using spray pyrolysis technique and annealing in air. *Molecular Crystals and Liquid Crystals*, 645(1):217–224, 2017.

[191] Boris D. Chernomordik, Amélie E. Béland, Donna D. Deng, Lorraine F. Francis, and Eray S. Aydil. Microstructure Evolution and Crystal Growth in Cu_2ZnSnS_4 Thin Films Formed By Annealing Colloidal Nanocrystal Coatings. *Chemistry of Materials*, 26(10):3191–3201, 2014.

[192] Bryce A. Williams, Michelle A. Smeaton, Nancy D. Trejo, Lorraine F. Francis, and Eray S. Aydil. Effect of nanocrystal size and carbon on grain growth

during annealing of copper zinc tin sulfide nanocrystal coatings. *Chemistry of Materials*, 29(4):1676–1683, 2017.

[193] Jonathan J. Scragg, Tomas Kubart, J. Timo Wätjen, Tove Ericson, Margareta K. Linnarsson, and Charlotte Platzer-Björkman. Effects of Back Contact Instability on Cu_2ZnSnS_4 Devices and Processes. *Chemistry of Materials*, 25(15):3162–3171, 2013.

[194] Sharadrao Anandarao Vanalakar, Soo Jung Yeo, Pramod Shankarrao Patil, Jin Young Kim, and Jin Hyeok Kim. Structural, optical, surface morphological and electrical properties of Cu_2ZnSnS_4 thin film synthesized by drop casting technique. *Zeitschrift für Physikalische Chemie*, 228(9):917–926, 2014.

[195] Min Zhou, Yanmei Gong, Jian Xu, Gang Fang, Qingbo Xu, and Jianfeng Dong. Colloidal CZTS nanoparticles and films: preparation and characterization. *Journal of alloys and compounds*, 574:272–277, 2013.

[196] Jie Shen, Dingwen Zhang, Junjie Li, Xiaodong Li, Zhuo Sun, and Sumei Huang. Fabrication and evaluation of low-cost $Cu_2ZnSn(S, Se)_4$ counter electrodes for dye-sensitized solar cells. *Nano-Micro Letters*, 5(4):281–288, 2013.

[197] Giorgio Tseberlidis, Vanira Trifiletti, Alessia Le Donne, Luigi Frioni, Maurizio Acciarri, and Simona Binetti. Kesterite solar-cells by drop-casting of inorganic sol–gel inks. *Solar Energy*, 208:532–538, 2020.

[198] Sunil Kumar Samji and MS Ramachandra Rao. How different are CZTS grain boundaries? *Scripta Materialia*, 194:113605, 2021.

[199] Jagatpati Raiguru, Bidyadhar Subudhi, BVRS Subramanyam, and Pitamber Mahanandia. Intermittent sulfurization—a method promoting Macro-Porous Cu-Poor Zn-Rich—kesterite CZTS as HTM for inverted perovskite solar cell application. *Journal of Materials Science: Materials in Electronics*, 31(21): 18427–18444, 2020.

[200] Nagabhushan J Choudhari, Y Raviprakash, Brian Jeevan Fernandes, and NK Udayashankar. Role of soaking time on the phase evolution of Cu_2ZnSnS_4 polycrystals synthesized using melting route for photovoltaic applications. *Journal of Alloys and Compounds*, 799:314–324, 2019.

[201] Subhash Pandharkar, Ashvini Punde, Mamta Nasane, Vidya Doiphode, Pratibha Shinde, Priti Vairale, Yogesh Hase, Ajinkya Bhorde, Ashish Waghmare, Sachin Rondiya, et al. Soft annealing effect on the properties of sputter grown Cu_2ZnSnS_4 (CZTS) thin films for solar cell applications. *Materials Today: Proceedings*, 34:690–696, 2021.

[202] MA Olgar, MURAT Tomakin, T Kucukomeroglu, and E Bacaksız. Growth of Cu_2ZnSnS_4 (CZTS) thin films using short sulfurization periods. *Materials Research Express*, 6(5):056401, 2019.

[203] MA Olgar. Optimization of sulfurization time and temperature for fabrication of Cu_2ZnSnS_4 (CZTS) thin films. *Superlattices and Microstructures*, 126:32–41, 2019.

[204] Ali E Rakhshani and S Thomas. Cu_2ZnSnS_4 films with Cu-poor composition prepared by spin coating from a nontoxic methanol-based solution: the effect of annealing temperature. *Journal of Asian Ceramic Societies*, 8(3):827–834, 2020.

[205] Louise S Price, Ivan P Parkin, Amanda ME Hardy, Robin JH Clark, Thomas G Hibbert, and Kieran C Molloy. Atmospheric pressure chemical vapor deposition of tin sulfides (sns, sn2s3, and sns2) on glass. *Chemistry of materials*, 11(7):1792–1799, 1999.

[206] Begum Unveroglu and Giovanni Zangari. Effect of cell configuration on the compositional homogeneity of electrodeposited Cu-Zn-Sn alloys and phase purity of the resulting Cu_2ZnSnS_4 absorber layers. *Electrochimica Acta*, 255: 347–357, 2017.

[207] PA Fernandes, PMP Salomé, and AF Da Cunha. Growth and Raman scattering characterization of Cu_2ZnSnS_4 thin films. *Thin solid films*, 517(7): 2519–2523, 2009.

[208] Atul Kumar, Pranay Ranjan, and Ajay D Thakur. Secondary Phases in CZTS Thin Films Grown Using Direct Liquid Coating Approach. *Materials Today: Proceedings*, 5(1):99–103, 2018.

[209] Christopher Bosson. *Understanding Cu_2ZnSnS_4 as a Photovoltaic Absorber for the Future of Solar Electricity*. PhD thesis, Durham University, 2018.

Colophon